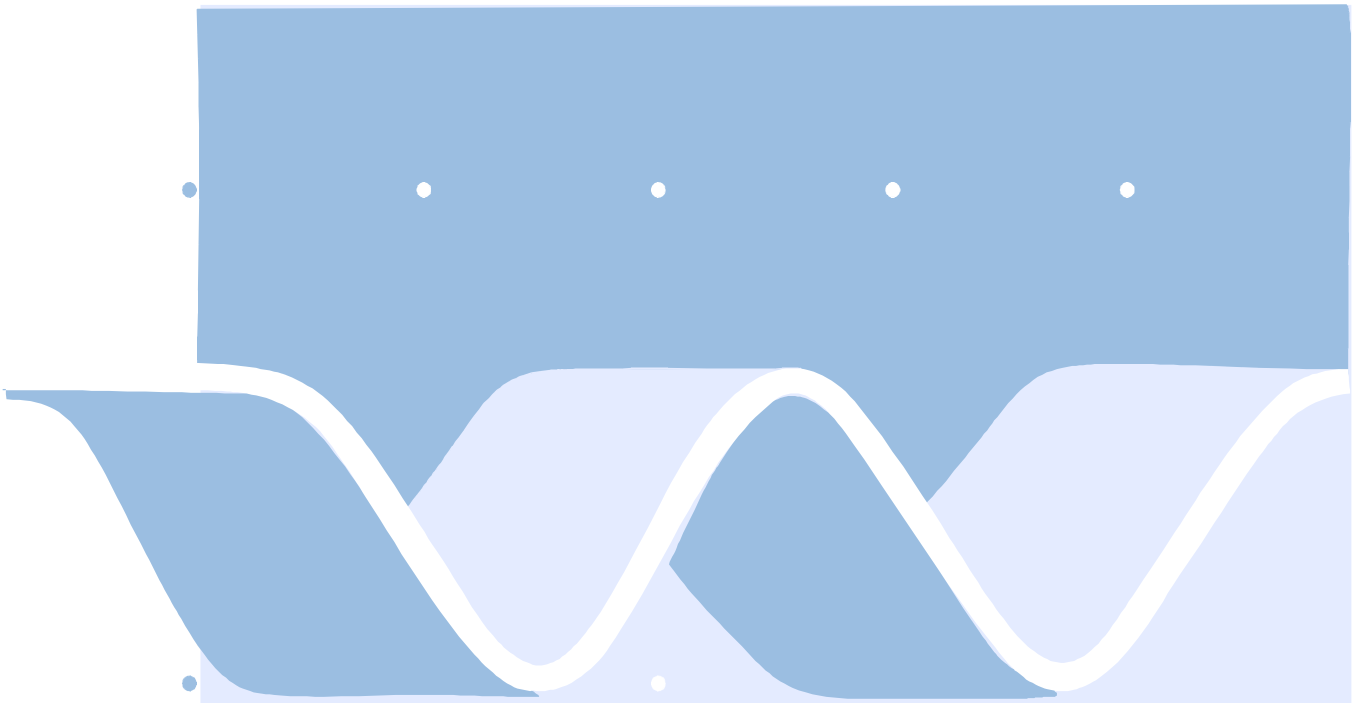

Prepared for:

RIKZ

Beach Wizard

A data model assimilation method for nearshore bathymetry and coastal state indicator estimation

Report

November, 2006

WL | delft hydraulics

Z4293

Prepared for:

RIKZ

Beach Wizard

A data model assimilation method for nearshore bathymetry and coastal state indicator estimation

Ap van Dongeren and Anna Cohen

Report

November, 2006

WL | delft hydraulics

CLIENT: Rijkswaterstaat, Rijksinstituut voor Kust en Zee

TITLE: Beach Wizard - A data model assimilation method for nearshore bathymetry and coastal state indicator estimation

ABSTRACT:

In this report an assimilation model is presented which is capable of estimating the sub- and intertidal bathymetry based on the difference between remotely sensed quantities such as the roller energy dissipation rate, wave celerities and intertidal bed elevation and the corresponding computed quantities for a large number of time instances.

The present method is an improvement over the previous method by Aarninkhof et al. (2005a,b) because of the use of a gradient method with fewer free parameters and the incorporation of other sources than roller energy dissipation. The rms error in Egmond from the previous method is 1.3-1.5 m. With the presented method the rms error in Egmond reduces to 0.6 m.

The model is validated for a synthetic case which shows that the assimilation scheme is capable of recovering a barred beach bathymetry starting from an initially plane beach and only "knowing" the dissipation rate and celerity fields.

The application to the Duck case shows that over a short time span (including one major storm) the model is capable of predicting the bathymetry rather accurately given a sequence of remotely observed inputs. The overall rms error in Duck is 0.4 m, with best results around the bars and worst results near the shoreline.

The model was then applied to the longer term case of Egmond. Here, the model is also capable of predicting the profile change with the same parameter settings as in the Duck case. The agreement is better for the winter months with stronger observed signals than in the summer months. The overall rms error in Egmond is 0.6 m, with best results around the bars and worst results near the shoreline and over the bars in the summer months.

Finally, the model output is used to estimate Coastal State Indicators. The intra-annual behavior shows a large variability which is on the order of the long-term (decadal) variation that is captured by the annual ground-truth surveys.

REFERENCES: RKZ-1788 SAP bestelnummer "4500057226"

VER	AUTHOR		DATE	REMARKS	REVIEW		APPROVED BY	
1.0	Van Dongeren and Cohen		7/11/2006		J.A. Roelvink		T. Schilperoort	
2.0	Van Dongeren and Cohen		27/11/2006		A. vd Weck		T. Schilperoort	

PROJECT NUMBER:	Z4293		
KEYWORDS:	Data-model integration, video, radar, ARGUS, Delft3D, sub tidal beach, bathymetry		
NUMBER OF PAGES:	88 pages		
CONFIDENTIAL:	☒ YES, until December 2006	☐ NO	
STATUS:	☐ PRELIMINARY	☐ DRAFT	☒ FINAL

Contents

List of Figures

List of Figures

1 Introduction

Information on the actual state of the nearshore zone – in terms of topographic variability, surface waves, and circulation patterns – is crucial in many civilian and naval applications, including shoreline management, protection of the hinterland against flooding, recreational safety, mine counter-measure strategies and covert military operations. Obtaining this information by in situ measurements is often not feasible, for instance because of costs, logistic limitations, hostility of the surf zone, or short notice on which data is needed.

As an alternative, sophisticated numerical models may be used to estimate the actual state. Numerical models that predict the hydrodynamics of these environments are reaching the level of complexity and numerical efficiency necessary for them to be used in an operational sense. Coupling the hydrodynamic models with sediment transport and topographic evolution are also nearing operational form. However, state-of-the-art surf zone models have shown insufficient forecasting capabilities so far at the spatial scales of interest. For typical nearshore processes (including circulation cells, sand bars, and submarine shelf topography) these span distances on the order of 100’s of meters to a few kilometres. One of the most severe limitations in the accurate prediction of waves and currents is the lack of information of one of the most important inputs: the underlying bathymetry.

Improvement of the models’ skill, and hence lengthening of the predictive horizon, may be expected from assimilating field measurements in near real-time. In that sense, of particular interest are remotely sensed data, which can be obtained without interference with the environment and, once the sensor and its platform are in place, with little logistic effort. For the surfzone environment, these measurement capabilities have been developed using primarily video (e.g. Aarninkhof and Holman, 1999; Alport et al., 2001; Aarninkhof et al., 2005a,b) and radar observations (e.g. Bell, 1997), and include surface current measurements (Chickadel et al., 2003), wave breaking distributions (Turner et al., 2004), shoreline position (e.g. Plant and Holman, 1997; Aarninkhof et al., 2003), sand bar position (Van Enckevort and Ruessink, 2003a,b), and wave phase speeds (Stockdon and Holman, 1998). Although these methods have largely been developed for shore-based applications, airborne platforms have also demonstrated similar measuring capability (Dugan, 2001). In any case, the assimilation of these types of data into currently available models will yield improved hindcasts, nowcasts, and forecasts of the nearshore environment.

Aarninkhof et al. (2005a) presented a technique to map 2D (cross-shore) bathymetry from time averaged video imagery using a simple linear relationship between erosion and accretion and the difference between modelled and measured roller energy dissipation. For this calculation the video-observed dissipation bands were quantified using pre-processing which will described briefly in this paper. Aarninkhof et al (2005a) demonstrated that such a model is capable of reproducing the dominant morphological changes during the first year after placing a shoreface nourishment at a multiple barred beach at Egmond. The rms error of the vertical deviations along the entire beach profile typically amounts to 40 cm for the two arrays considered. Deviations in the order of 10 to 20 cm were found at the seaward face of the bars, which increase up to 20 to 40 cm near the bar crest. Maximum deviations up to 80 cm were found in the trough regions, owing to lack of wave dissipation information.

Aarninkhof et al. (2005b) presented the extension of this method to 2DH and incorporation of the assimilation schemes in the Delft3D modelling system. The Delft3D model is capable of modelling 2DH and 3D hydrodynamics and morphodynamic changes over time-scales ranging from wave groups to several weeks, at spatial scales resolving rip-current cells and breaker bars (e.g. Reniers et al., 2004; Lesser et al, 2004). In particular, model application at Palm Beach, NSW (Australia) has contributed significantly to our understanding of nearshore morphodynamic processes (Reniers et al, 2001) showing the strong correlation between spatial distribution of computed wave energy dissipation and observed video intensity on a alongshore variable nearshore bathymetry. Aarninkhof et al. (2005b) compared to pilot cases at Monterey, USA and Egmond, the Netherlands. While proving the concept of a data-model assimilation method in 2D, their results still showed large deviations from ground truth in the troughs and near the shoreline.

2 Objectives of this report

The objective of this study is to derive a robust assimilation model with which accurate estimates of the seasonal variation are possible, apply this model to two field cases and calculate the coastal state indicators on an intra-annual time scale.

Specifically, the following objectives are defined (based on the RFP by Rijkswaterstaat):

- Continue to develop the model such that an analysis of the seasonal variability is possible, including improvement in the nearshore and trough areas.
- Define uncertainty estimates of the bathymetry.
- Validate with data from Egmond and Duck.
- Make predictions with a high resolution in time (on the order of 40 estimated per year) of the Momentary Coast Line, bar positions and bar elevations.
- Determine the seasonal variation of the MCL, including a comparison with MCL estimates from ground-truth JARKUS measurements.
- Discuss the added value of the Beach Wizard for Rijkswaterstaat purposes.

Concretely, we will present an improved 2DH method assimilation method based on the derivatives of the observed properties with respect to depth (a “gradient-descent” method). We will extend Aarninkhof’s method from one source to multiple (currently three) sources, while reducing the number of free parameters that need to be set from two per source to nil per source, and only one overall parameter. The sources that are added are video-observed intertidal bathymetry and radar-derived wave celerities. The uncertainties in the bathymetric estimates are quantified and presented with the bathymetric estimates.

Starting from an arbitrary, best guess initial bathymetry the model calculates a spatial distribution of roller energy dissipation and wave celerity across the bathymetry for the actual wave and tide conditions (water level, wave height, peak period and wave angle). The video time exposure image provides the observed spatial distribution of roller energy, while the processed information from the radar provides the observed wave celerities. The mismatch between observed and computed patterns is used to ‘nudge’ the model bathymetry towards one that better fits the observed dissipation pattern. This simulation is run for each available image so that different tidal and wave conditions can incrementally contribute to the bathymetric estimate.

The method is validated against a synthetic case and applied to two field sites at Duck, NC (USA) for a short-term (10 day) forecast and Egmond, The Netherlands for a long-term (18 month) hindcast. For the former field case we will incorporate video-measured intertidal bathymetry and radar-derived celerities. For the latter case we will use the measured intertidal bathymetry as a source and estimate coastal state parameters (with a frequency of about 40 estimates per year) such as the momentary coastal line (MCL), the bar positions and the bar height and compare these to annual ground-truth measurements. In this way the intra-annual variation and behavior of the coastal system at a higher resolution than the ground-truth measurements can be visualized.

We will conclude the report with a discussion on the applicability of the model for Rijkswaterstaat purposes, the present limitations of the model and possible future remedies.

3 Formulation and Implementation in D3D

The essence of the assimilation model is to iteratively solve (in time) for the local bed level so that the difference between an observed (measured) local quantity $f_m(x,y,t)$ and a computed quantity $f_o(x,y,t)$ become minimal. This process of adjustment can be written as a first order ordinary differential equation, or

$$\frac{df_m}{dt}+\frac{\alpha}{T_s}\left(f_m-f_o\right)=0 \tag{1}$$

where α is an adjustment rate, T_s is the length of a simulation run (and is on the order of 1 hour) and we have dropped the space and time-dependencies. Using the chain rule

$$\frac{df_m}{dt}=\frac{df_m}{dh_m}\frac{dh_m}{dt} \tag{2}$$

we can rewrite the decay function as

$$\frac{dh_m}{dt}+\frac{\alpha}{T_s}\left(\frac{df_m}{dh_m}\right)^{-1}\left(f_m-f_o\right)=0 \tag{3}$$

Given the difference between a modelled and observed property, all that is needed is the derivative $\frac{df_m}{dh_m}$. These derivatives are computed for the sources of wave dissipation, celerity and intertidal bathymetry in Appendix A.

This bed updating scheme involves only one (yet) free parameter α as opposed to the scheme proposed by Aarninkhof et al. (2005a,b) which involved two free parameters (w_A

and w_E for accretion and erosion) and which were treated physically differently. We have in the present implementation done away with the concept of a virtual buffer layer of suspended sediment proposed by Aarninkhof et al. (2005a). This choice implies that the present model does not conserve mass.

This assimilation model works well in a perfect world (see e.g. synthetic example in Cohen et al, 2006) in which there are no measurement errors and the derivatives are nonzero. However, in a real world application we need to account for measurement errors in f_o and the fact that the derivative should not go to zero. The zero derivative implies that the quantity is not dependent of depth, which is the case for e.g. dissipation for large water depths. If for some reason spurious dissipation were observed at these large depths – something that may occur using video data – the bottom update would become infinitely large.

To avoid these singularities the updating scheme is changed to

$$\frac{dh_m}{dt}+\frac{\alpha}{T_s}\frac{\dfrac{df_m}{dh_m}}{\left[\left(\dfrac{df_m}{dh_m}\right)^2+\beta\left(\dfrac{df_m}{dh_m}\right)^2_{\max}\right]}\frac{\left(f_m-f_o\right)^2}{\left(1+\dfrac{\sigma^2}{\left(f_m-f_o\right)^2}\right)}=0 \qquad (4)$$

where σ is the measurement error for a given source, $\left(\dfrac{df_m}{dh_m}\right)^2_{\max}$ is the maximum value of the squared derivative over the entire domain and β is a small value (on the order of 0.005 in our applications) to ensure that the second (maximum) term in the denominator only becomes dominant in the case where the local derivative is very small. The measurement error controls that the bathymetric response to small differences between a modelled and observed quantity is limited. The value of σ is a function of the measurement technique and not of the environmental conditions, i.e. it is not a freely tuneable parameter in the model runs.

This assimilation model is generalized for multiple sources as

$$\frac{d\,h_m}{dt}+\sum_{i=1}^{S}\left(\frac{\alpha_i}{T_s}\frac{\dfrac{\partial f_{i,m}}{\partial h_m}}{\left[\left(\dfrac{\partial f_{i,m}}{\partial h_m}\right)^2+\beta\left(\dfrac{df_{i,m}}{dh_m}\right)^2_{\max}\right]}\frac{\left(f_{i,m}-f_{i,o}\right)}{\left(1+\dfrac{\sigma_i^2}{\left(f_{i,m}-f_{i,o}\right)^2}\right)}\right)=0 \qquad (5)$$

where the index i indicates the source. For the present application we have limited the number of sources to three: wave roller energy dissipation, wave celerity and intertidal bathymetry. These sources may be extended with any measurable quantity that can be expressed as a differentiable function of depth, e.g. percentage of breaking, phase speed of the roller, wave height.

The uncertainty in a source for a given simulation run can be estimated as

$$\varepsilon_i = \sqrt{\frac{\left(f_{i,m} - f_{i,o}\right)_i^2 + \sigma_i^2}{\left(\frac{\partial f_i}{\partial h}\right)^2}} \tag{6}$$

which states that the uncertainty is large when the difference between the modelled and observed quantities are large (i.e., the modelled bed level must deviate considerably from ground truth), the measurement error is large (i.e., untrustworthy source) or the gradient is small (the quantity is locally not depth-dependent). Vice versa, the uncertainty is small when the differences are small, the measurement error is small and the gradient large. The uncertainty in the bed update after each simulation run is the ensemble of the uncertainties of the individual sources or

$$\varepsilon_{sum} = \sqrt{\frac{1}{\sum_i \left(\frac{1}{\varepsilon_i^2}\right)}} \tag{7}$$

where the double reciprocal is applied so that the source with the smallest uncertainty is locally dominant (cf. Kalman-filtering). Please note that we had dropped the space dependency in our notation and that the uncertainties are a function of space.

The updating still has one free tuneable parameter per source, the rate of update α_i, which value should vary between 0 (if locally the driving force is not to be trusted and no bottom update should take place) and 1 (where there is high confidence that the driving force is correct). This effectively links α_i to the uncertainty ε_i. In the model we have chosen to set

$$\alpha_i = e^{-\varepsilon_i} \tag{8}$$

which makes the parameter unity when the uncertainty is small and lets it go to zero when the uncertainty is large. In this way, the model has no free parameters anymore, apart from the simulation length T_s.

The assimilation scheme is applied to successive (in time) sources, e.g. a sequence of video images or radar images. Images from different sources can also be applied parallel in time, each time nudging the bathymetry in the right direction. The total integrated uncertainty over time is then a function of the uncertainty of the present run (image) and the total uncertainty at the time of the previous run (image) or

$$\varepsilon_{tot,j}^2 = \frac{\varepsilon_{sum,j}^2 \, \varepsilon_{tot,j-1}^2 e^{(t_j - t_{j-1})/T_r}}{\varepsilon_{sum,j}^2 + \varepsilon_{tot,j-1}^2 e^{(t_j - t_{j-1})/T_r}} \tag{9}$$

where j is the index of the run (image) and the exponential factor is introduced so that the uncertainty is increased if the time interval between successive runs is large. The time scale

T_r is set at 5 days and reflects a physical interpretation that a previously computed uncertainty is invalidated due to morphological changes over a period of days.

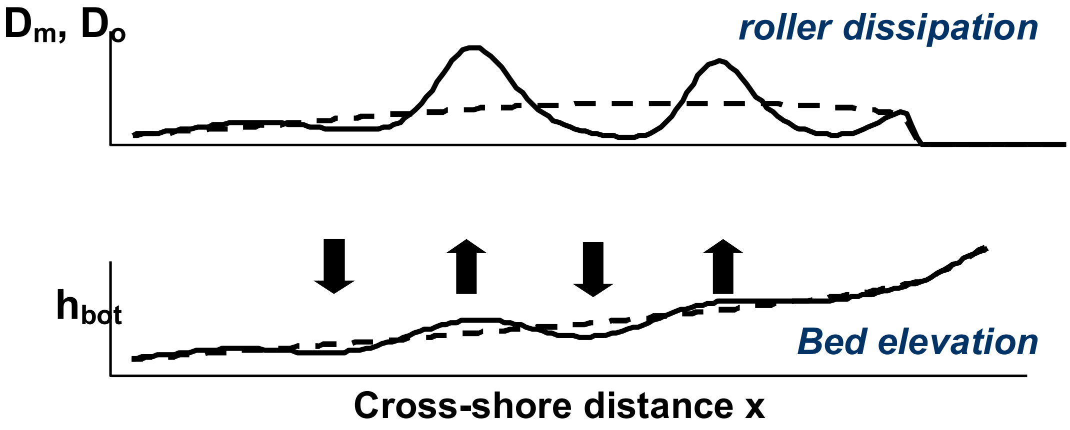

Figure 1: Top panel: modelled observation (solid line) and observed dissipation (dashed line) as function of cross-shore distance (shore to the right). Bottom panel: bathymetric response, initial bathymetry (dashed line) and adjusted bathymetry (solid line).

The essence of the assimilation model can be explained by considering only roller dissipation as a source (Figure 1). The top panel shows the observed dissipation (solid line) over a bar-trough bathymetry (solid line in bottom panel). The modelled dissipation (dashed line in top panel) is calculated over an initially monotonic slope (dashed line, bottom panel). If the observed dissipation is locally larger than the modelled dissipation, the driving force in 5 is negative and the depth will decrease, i.e. a bar will be formed under the area of locally large observed dissipation. Conversely, if the computed dissipation exceeds the measured dissipation, the depth is increased and a trough is formed. As we will show in the synthetic example, the computed dissipation will adjust to the changing computational bathymetry until it matches the observed dissipation and a converged bar-trough bathymetry is found.

The assimilation model is compactly implemented in the Delft3D model in the module “Assim” (Figure 2) and can be run alone or parallel with other modelled processes in the software, most notably physics-based sediment transports. For the present purpose, physics-based sediment transports are turned off to focus on the assimilation routines.

Figure 2 shows that – given an initial bathymetry – both Delft3D-WAVE and Delft3D-FLOW are executed in the “Waves-on-line” mode. The Wave module which is essentially the “SWAN” program (Booij et al., 1999) computes the wave directions which are read in by Delft3D-FLOW. The wave driver used in FLOW is the so-called roller model (Roelvink, 1993; Reniers et al., 2004) which concurrently solves the energy equations of the organized wave motion and the roller motion using expressions for the wave and roller energy dissipation by Baldock et al. (1999) and Reniers et al. (2004), respectively. We refer to Reniers et al. (2004) for details on the modelled equations. From these energy equations and linear theory we can derive the computed sources, such as the roller energy dissipation and the (shoreward projection of the) wave celerity. These computed quantities are compared to the corresponding observed quantities, in our case from video and radar.

In the assimilation routine Eq. 5 is solved given the (interpolated) input fields, parameters and computed derivatives (Appendix A). The bed update is done in the same routine as the physics-based morphological updates and the option of computing physics-based sediment transport in conjunction with the assimilation model is not excluded. The updated bathymetry is fed back into the wave model at set intervals, so that a new set of wave directions can be computed on the updated bathymetry. At the end of a simulation run (for a given time-instance where there is a source available) the bed is written to file and is used as the initial bathymetry in the next simulation run.

Each of the simulation runs is in stationary mode, which means that the water level and offshore wave conditions are assumed constant for the duration of the simulation (about 2 hours maximum). The boundary conditions therefore consist of tidal elevation, offshore H_{rms} wave height, peak period and mean direction. In hindcast mode these quantities can be derived from nearby gauges and buoys. A simulation run is performed at all the time instants where there is remotely-sensed data available. For some simulation runs data from one source and for some runs concurrent data from multiple sources is used. In order to properly compute the bed evolution it is necessary to perform a large number of sequential simulation runs (on the order of 50 to 100 in our applications) for a diverse set of combinations of wave conditions and water levels so that the driving force for the bed update can be applied all along the sub- and intertidal bathymetry.

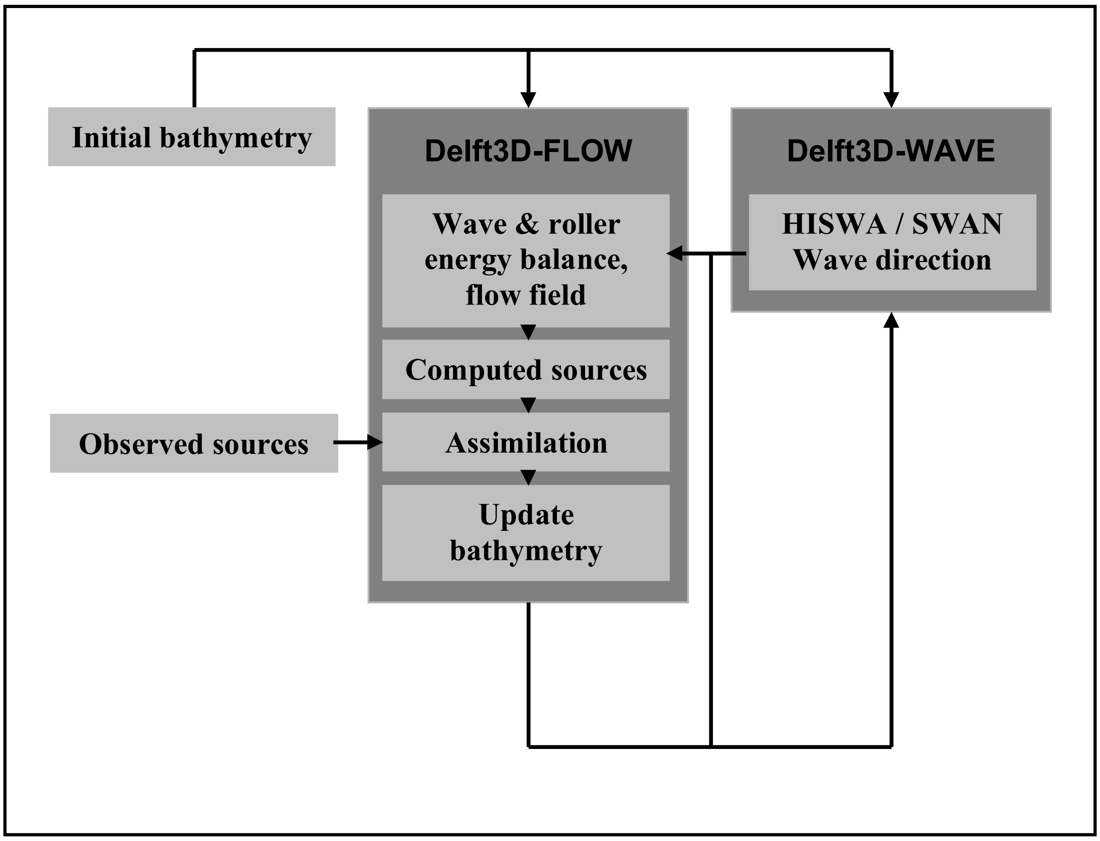

Figure 2: Schematic of the incorporation of the Assimilation routine in the Delft3D software package.

4 Verification with synthetic case

The assimilation model is validated against a synthetic case of the modelled wave energy evolution over a barred 1D bathymetry taken from the Boers (1996) flume experiments, which were a fixed bathymetry scale model experiments of the large-scale LIP experiments (Arcilla et al., 1994). From the set of wave conditions we have selected case 1C (scaled parameters H_{rms}=0.073 m, T_{m01}=2.25 s), with a high wave steepness and wave breaking over the bar and near the shoreline.

The assimilation model has been implemented into a 1D (Matlab) version of the roller model. First a target run is performed on the actual Boers bathymetry to determine the celerity and roller energy dissipation profile over this bathymetry. The steady state result is taken as the "measurements" D_o and c_o, all other information (most notably the bathymetry) is discarded. The aim is to use the assimilation model starting from an initially plane slope and given the known wave boundary conditions and determine whether the actual barred bathymetry can be recovered.

Even though the "measured" data is perfect the model is run with measurement errors σ_D=0.2 (W/m^2) and σ_c=0.25 (m/s), which is about 10% of the maximum value of D_o and the mean value of c_x, respectively. This will restrain the bathymetric change in areas where the difference between the modelled and observed quantities is small.

The model is run until steady state is reached, after which the bottom update routine is invoked at t/T = 0, where T is the duration of the morphological update. Figure 3 shows the evolution of the computed bed level (top row, solid lines) towards the target (dashed lines) for four time instances. The update is driven by the difference between the computed (solid lines) and "measured" (dashed lines) roller energy dissipation (third row) and celerity (bottom row). These differences are seen to decrease over time, which means that the driving force reduces and the solution converges. This is confirmed by the evolution of the differences in the computed bed level and the target bed level in the second row, which decrease over the duration of the simulation with a factor 10. The differences do not go to zero due to the inclusion of the measurement errors and the finite length of the simulation but would if these constraints were removed.

This verification shows that the assimilation model is stable and converges to the correct solution.

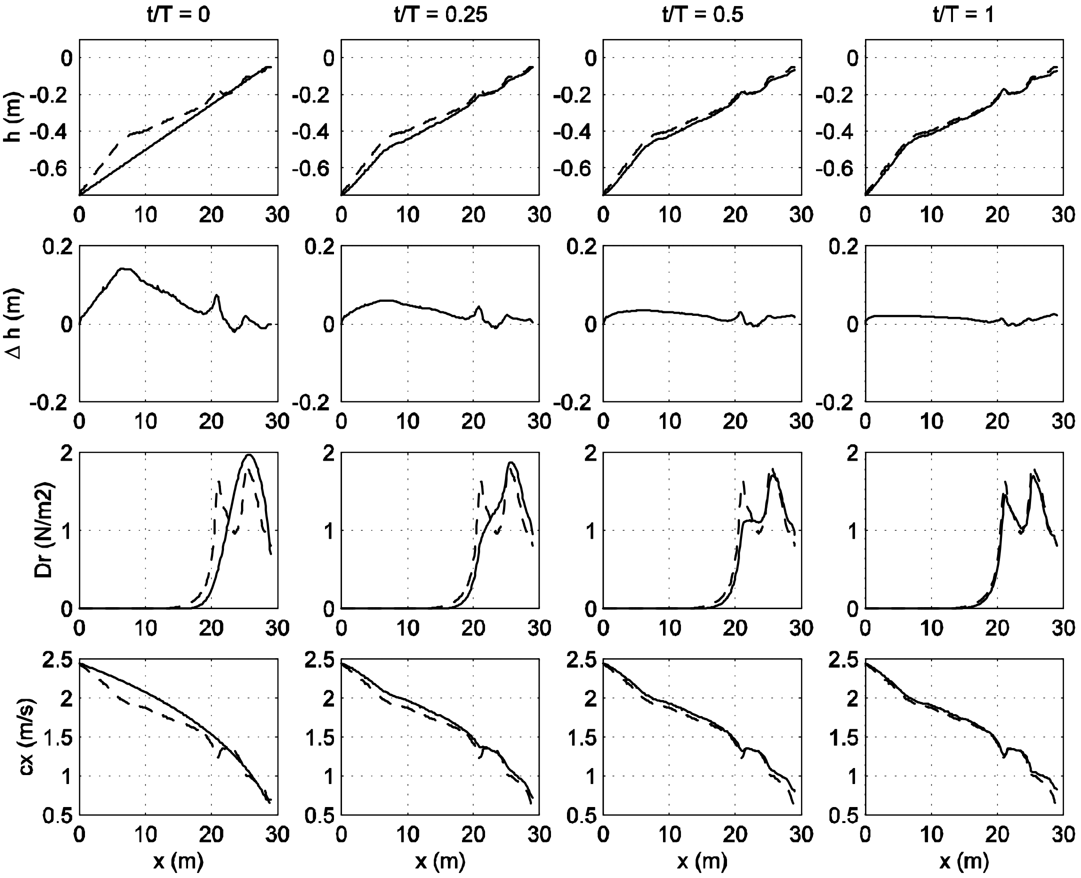

Figure 3: Top row: evolution of the computed bed level (solid line) and target bathymetry (dashed line); second row: difference between computed bed level and target; third row: computed (solid line) and "measured" (dashed line) roller dissipation; bottom row: computed (solid line) and "measured" (dashed line) celerity. The columns indicate four time instances (t/T = 0, 0.25, 0.5 and 1).

5 Data sources

The assimilation model is driven by the difference between computed and observed sources. In the applications which are shown below three sources are implemented: roller energy dissipation, intertidal bathymetry and wave celerity. The data collection and processing of these data is discussed in this section.

5.1 Roller energy dissipation

The primary source used in the assimilation model is the difference between observed and computed roller energy dissipation. The observed roller energy dissipation is derived from plan view Argus video images, obtained from merging and rectifying oblique time exposure sampled from one or more video cameras that cover the area of interest (e.g. Figure 4). The procedure largely follows Aarninkhof et al. (2005b) and is repeated here in brief.

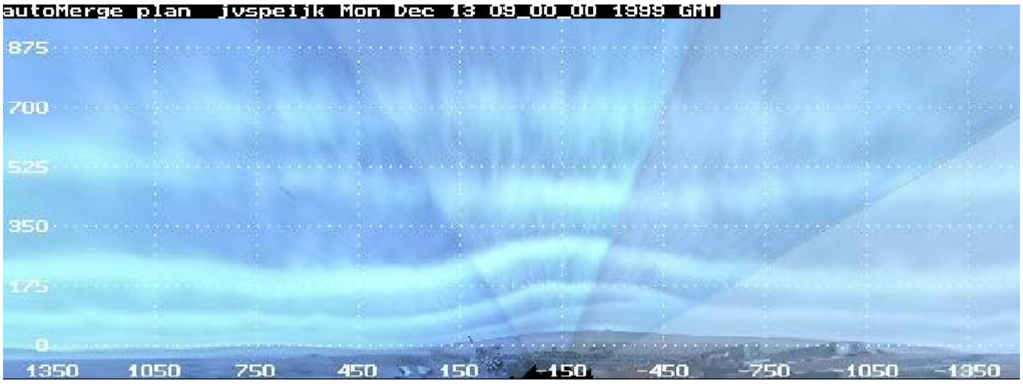

Figure 4: Merged plan view image of Egmond station Jan van Speijk of 13/12/1999 at 10:00 GMT.

To obtain a roller dissipation map from an image, a three-step approach is followed. First a background intensity level is removed, because an area with no wave breaking should map to no wave dissipation, hence the video intensity should be set to zero there. This is achieved by determining the average image intensity in the region well outside the surf zone (from 800 m to 1800 m offshore for the Egmond case), for each vertical image line in the oblique image. Before transforming the oblique image to a plan view image this value is subtracted from each vertical image line. In addition, this approach was found to correct for cross-image variations of optical intensity characteristics and sharp transitions between camera views, caused by different camera orientations with respect to the position of the sun and the non-simultaneous collection of video data.

To obtain smooth wave dissipation maps covering multiple cameras, we further take into account differences in image contrast levels between cameras, because an area represented by a low contrast image will result in unrealistically low wave dissipation levels in that area. This is achieved by adopting the standard deviation σ_{sz} of surf zone pixel intensities as an indicator for image contrast. An image-specific σ_{sz} is determined from pixel intensities sampled from a nearshore region enclosed by shore-parallel lines (at 100 m and 1000 m offshore). Breaking-induced image intensities collected from different cameras are corrected by the ratio between the minimum σ_{sz} of all cameras involved and the standard deviation $\sigma_{sz,i}$ of surf zone pixel intensities of camera i or

$$I_{c,i} = \left(\frac{\sigma_{sz,\min}}{\sigma_{sz,i}} \right) I_i \tag{10}$$

where $\sigma_{sz,i}$ is the standard deviation of surf zone pixel intensities of camera i, $\sigma_{sz,min}$ is the minimum σ_{sz} of all cameras involved and I_i is the breaking-induced image intensity map of camera i (after correction for background illuminations) and $I_{c,i}$ is the breaking-induced image intensity map after correction for variable image contrast. This ratio $\sigma_{sz,min}/\sigma_{sz,i}$ typically varies between 0.5 and 1. Merging the individual camera views after correction for background illuminations and variable image contrast yields a plan-view, wave dissipation map I_v, which typically covers a coastal stretch up to a few kilometres alongshore.

Finally, the corrected image intensities are scaled such that they are a quantitatively correct measure of roller dissipation. To that end, we normalize I_v so that the total normalized intensity in the model domain is equal to unity, and scale the normalized intensity map with the incoming wave energy flux to obtain a video-derived measure of wave dissipation D_o that quantitatively matches the model-computed roller dissipation or

$$D_o(x,y) = \left(\frac{I_v(x,y)}{\int\limits_x \int\limits_y I_v dxdy} \right) \int\limits_y Ec_g \cos\theta dy \tag{11}$$

where the wave energy at the offshore boundary of the model $E = 1/8 \rho g H_{rms}^2$ and c_g is the wave group velocity and θ is the wave angle of incidence with respect to shore normal. The resulting maps of D_o are stored for each processed (composite) image and to be used in the assimilation model.

5.2 Intertidal bathymetry

Intertidal beach bathymetries are generated with the Intertidal Beach Mapper (IBM, Aarninkhof et al, 2003). The model determines the three-dimensional beach surface between the low-tide and high-tide shoreline contours by mapping a series of beach contours, sampled throughout a tidal cycle. IBM delineates a shoreline feature from time-averaged video imagery on the basis of the visual contrast between the sub-aerial and sub-aqueous parts of the beach. The corresponding shoreline elevation is estimated from the tide and wave conditions at the time of image collection. Validation of IBM against a dataset of GPS-surveyed shorelines has shown that mean vertical model deviations increase with increasing distance from the video station and are less than 15 cm along the Egmond area (Aarninkhof et al., 2003).

Application of IBM over a single tidal cycle yields a dataset of shoreline sample points with variable sample spacing. The alongshore sample distance ranges from 1 to 15 m, depending on the pixel resolution which improves with decreasing distance to the video station. The cross-shore sample distance varies between 1 and 20 m and is governed by the local beach slope, the water level change between successive video images and the possible occurrence of emerging intertidal bars. Shoreline sample points are interpolated to a grid with a cross-shore spacing of 2 m and an alongshore spacing of 20 m.

5.3 Radar celerities

Marine radar image sequences were collected from a shore-based station at Duck, NC (USA) in September 2005. The station consists of a 25 kw SiTex marine radar with a 2.7 m scanning array antenna and is mated with a custom data acquisition system developed by Imaging Science Research (USA), see Figure 5. Collected data consists of a large number of approx. 15 minute image sequences. The footprint of each image is a semicircle of 1200m radius centered on the FRF pier. Individual images are collected at a rate of 44 images per minute (0.73 Hz) and a given sequence consists of 640 images. These approx. 15 minute image sequences were collected once per hour over a period of 5 days. The scanning marine radar antenna and an example image are shown in the Figure below. Further details of the radar system and data collection can be found in Lentine (2006).

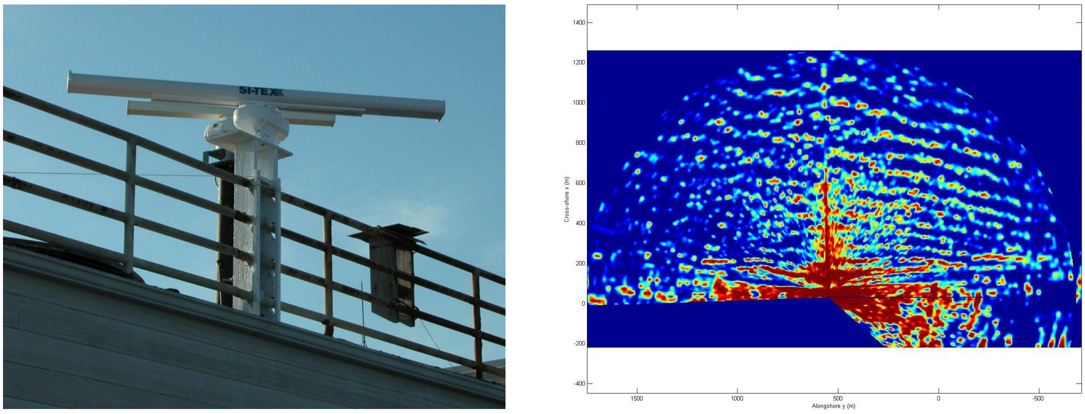

Figure 5: (a): SiTex radar antenna (white antenna, center of image) mounted above the FRF main building, (b): single radar image (Sept. 28, 2005), radar located at center of semi-circle. Bright linear (red and yellow) features represent wave crests. Shoreline is also visible as bright linear feature at cross-shore distances near 200 m.

In order to estimate wave celerities from these radar observations, the raw data is first converted from the range and azimuth coordinates in which it was collected to the Cartesian grid corresponding to the model domain. Hence, the raw radar data is geo-located and interpolated to a Cartesian grid. This processing is similar to that applied to Argus data. From these 0.73 Hz image sequences, the cross-shore component of the phase velocity is obtained from using a Complex Empirical Orthogonal Function analysis (Wallace and Dickinson, 1972), from which spatial maps of the wave celerity are obtained. These maps are then filtered by removing outlier celerity values that exceed a threshold value defined as the sum of the alongshore mean celerity and one alongshore standard deviation. These outliers were simply marked as NaNs (not-a-number).

5.3.1 Results

The resulting phase maps were further pre-selected based on two criteria: the first one is that the percentage NaNs (Not-a-Number) in the data should not exceed 30% otherwise the image is discarded. An additional criterion imposed was that only celerity maps demonstrating quasi-alongshore uniformity were considered. This was done by calculating the cross-shore average of the ratio of the alongshore standard deviation to the alongshore mean value of the observed celerities. The value of this quantity should not exceed 30%. . The celerity maps which pass both criteria have the remaining NaNs removed by interpolation. An example of measured and interpolated celerity maps is given in Figure 6.

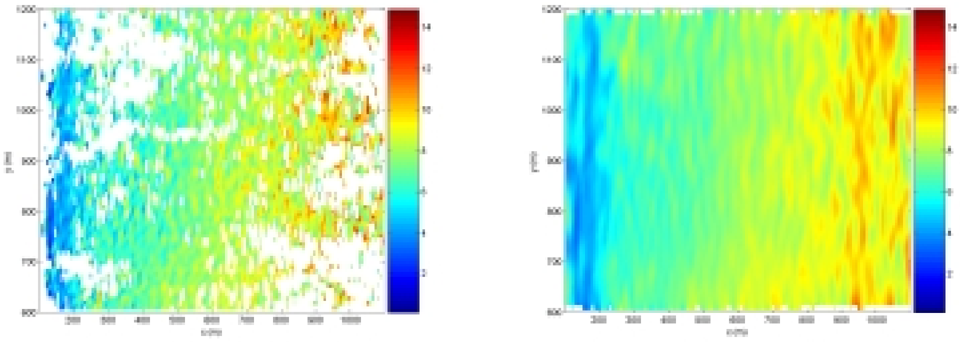

Figure 6: Left: Measured celerity map and right: celerity map after interpolation. Values of the celerities are in m/s.

6 Application to field cases

6.1 Duck

6.1.1 Situation

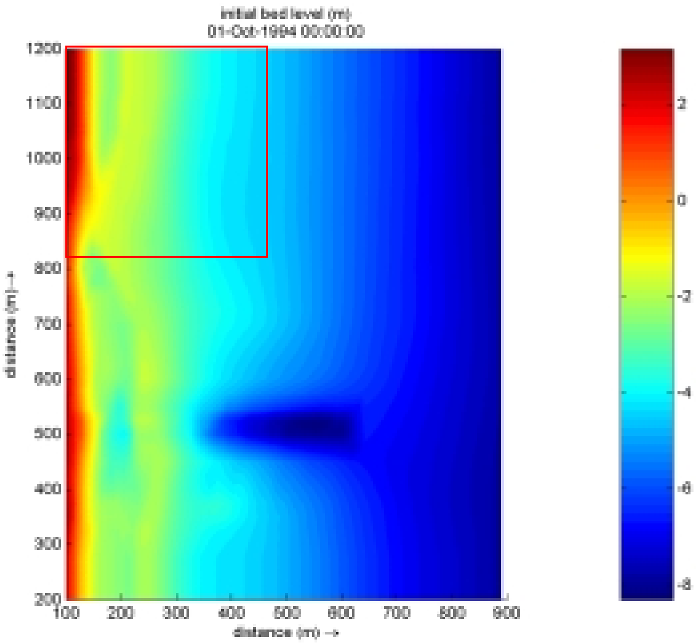

Figure 7: Initial (1994) bed level used in the model computation. The minigrid area is marked by the box.

The assimilation model was applied to the mini-grid area (see Figure 7) of the U.S. Corps of Engineers Field Research Facility (FRF) at Duck, NC (USA) for the period of 21-29 September 2005. Duck is located on the Mid-Atlantic coast of the USA. The micro-tidal beach (tide range of less than 1 meter) is exposed to swell from hurricanes to the South (which occasionally make landfall near Duck) and North-east storms and is characterized by a single bar. The site is selected because of the availability of an Argus station which provides time exposure images from which roller energy dissipation maps can be processed. In addition, wave celerity maps covering both sides of the FRF pier are available from marine radar data during the period of interest. The offshore boundary conditions in the model are provided by the measurement array of pressure sensors at 8 meters of water depth.

6.1.2 Model set-up

The Delft3D model spans from 200 to 1200 meters in y-direction (alongshore) and from 100 to 900 meters in x-direction (cross-shore), see Figure 7. However, the results and statistics will focus on the minigrid area (indicated by the box). The location of the FRF pier can clearly be seen as the scour hole in the bathymetry.

The assimilation starts with an arbitrarily chosen bathymetry from October 1994. For each instance that assimilation data are present, the model is run in stationary roller mode for a duration of 2 hours. At the offshore boundary, short wave energy and peak period (group speed) are imposed, the lateral boundaries are prescribed by the Neumann boundary condition. The tide level is assumed constant over each simulation run and is provided by the tide gauge mounted on the pier.

The flow and wave model were calibrated on Duck 1994 data. From this calibration, a breaking parameter γ=0.65 is derived. The measurement errors are scaled up from the synthetic case with approximate Froude scale 15, so that σ_D=10 W/m^2 and σ_c=1 m/s for the dissipation and the celerity respectively. We choose σ_S=0.5 m for the error in the intertidal bathymetry. These measurement errors will restrain the bathymetric change in areas where the difference between the modelled and observed quantities is small.

6.1.3 Data set

Three different data sources are available for this pilot application, e.g. wave dissipation, intertidal bathymetry and wave celerity. For about 50 time-exposure images, dissipation maps are constructed following the procedure described above.

A set of 4 intertidal bathymetries was generated based on time exposure images over the period 26/09/2005 until 29/09/2005 using the advanced Loess interpolator mentioned in section 5.2.

Radar image data were collected at the Duck site in September 2005 by the Oregon State University group (Haller and Catalan). These image sequences were used to generate wave celerity maps over the mini grid shown in Figure 7. Celerity maps were quality controlled based on the procedure described in Section 5.3. The present computations utilized a total of 6 maps at the end of the simulation period.

The results are shown in Figure 8 and Figure 9. The time history of the H_{m0} wave heights (Figure 9, top panel) shows that the period included one major and one minor storm. The assimilation is performed using 50 stationary runs divided over the interval of which seven are indicated by the red and blue dots in the figure. Red dots are runs with wave dissipation images, blue dots are runs with both wave dissipation and celerity images. These seven instances correspond to the seven rows of panels in Figure 8. There the bathymetric evolution is shown for two cross-sections (at y=800 and y=1100 m in the local FRF coordinate system). The computed bathymetry (solid red line) is shown to slowly evolve from the initial computational bathymetry (dashed red line), which was taken from the 1994 survey to the measured bathymetry (solid line). The integrated error (Eq. 9) is indicated by the error bars. Due to many successive images the error bar decreases. This is especially apparent offshore after the assimilation with the celerity data (bottom three rows). While at the cross-section at y=1100 m the modelled and measured bathymetry agree very well, this is not the case for y=800 m. There, the measured bar between x=100 and 200 m is not predicted. The issue of the formation of the beach terrace is addressed in the Discussion.

The bottom panel of Figure 9 shows the rms errors in the entire domain and in sub domains of the inner and outer surfzone and the shoaling zone. The overall error (black line) and the error in the outer surfzone (red line) are decreasing quite steadily over the simulation period. The error in the inner surfzone is constant and increases temporarily after the storm. The cause of this will be addressed in the Discussions section. The error in the shoaling zone decreases only slightly. Overall the total error is reduced by a factor two from 0.8 to 0.4 meters. The error in the subdivisions is either constant at around 0.4 m or decreases to that level, except for the error in the inner surfzone, which increase due to the building of the terrace (see Discussion).

The blue line in Figure 8 shows the measured bathymetry of 21 September 2005, thus at the start of the simulation. The measured bathymetry in y=800 m lies outside the error bands during the second half of the simulation. This is because the true bathymetry, especially in the area around y=800 m, has changed radically due to storm influences. The next available bathymetry is measured at 19 October 2005. This is outside the modelperiod and more time away from the end of the simulation (30 September) than the measurement at the start of the simulation. The 19 October bathymetry shows some sedimentation near the shoreline at y=800 m, which agrees with the model results shown in Figure 8.

The conclusion of this hindcast is that the modelled bathymetry rapidly approaches the measured bathymetry on the basis of a sequence of remotely-observed images.

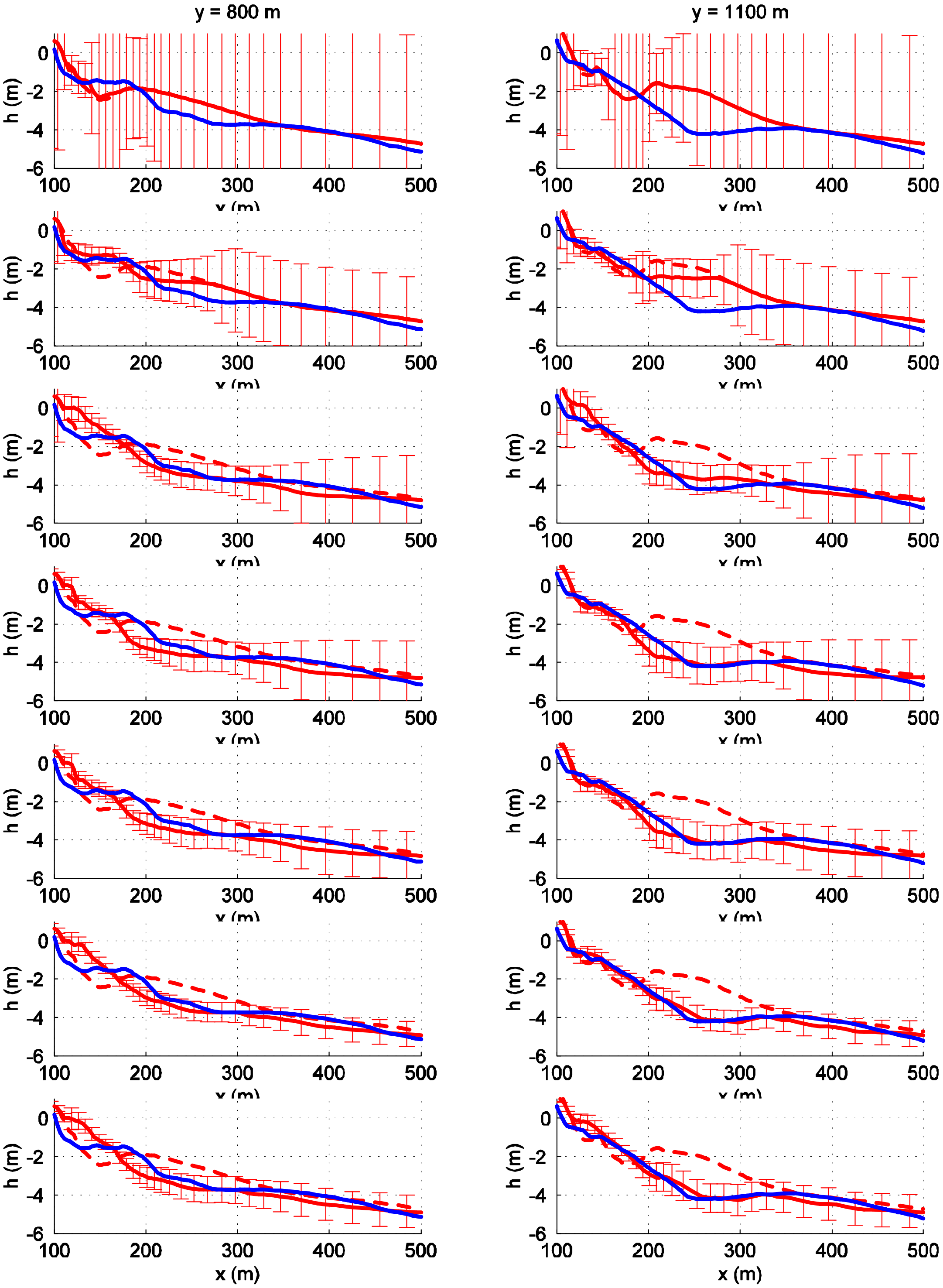

Figure 8: Computed (solid red line), measured (solid blue line) and initial (dashed red line) bathymetries for two transects at y=800 and y=1100 m for seven time instances given in Figure 9.

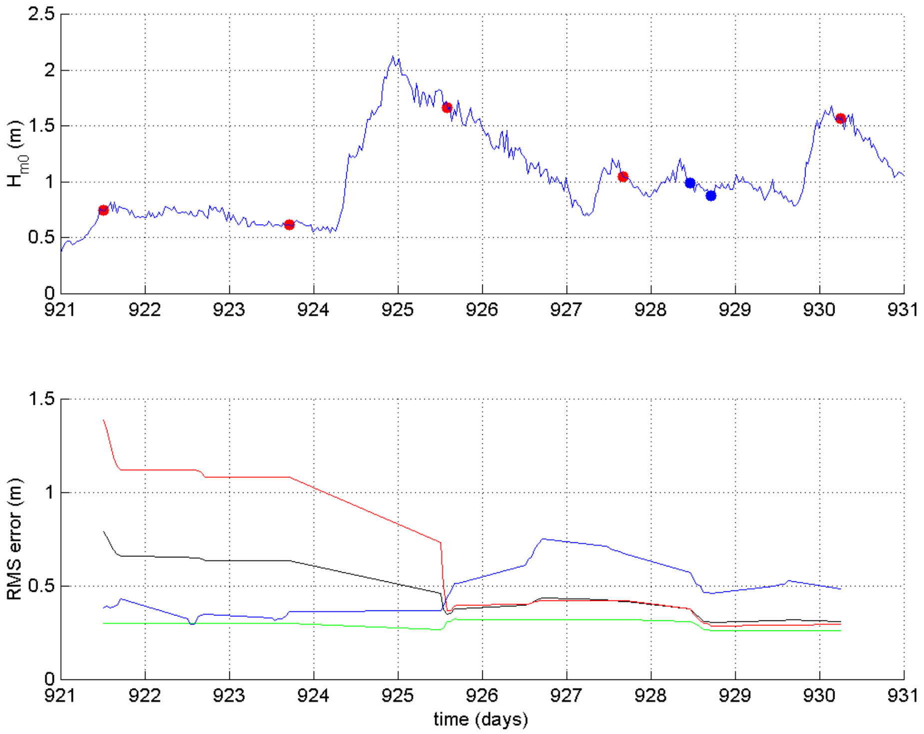

Figure 9: Top panel: Time history of the offshore Hm0 wave height. The red dots indicate the pictured time instances with only wave dissipation images. The blue dots have both wave dissipation and celerity field images. Bottom panel: the rms error between computed and measured bathymetries. The black line is the error in the entire domain between x=150 and x=500 and y=800 and y=1200 m. The blue line is the error in the inner surf zone (150<x<200 m), the red line is the error in the outer surfzone (200<x<300) and the green line is the error in the shoaling zone (300<x<500 m)

6.2 Egmond

6.2.1 Situation

The second pilot application involves the assessment of the evolution of subtidal bathymetry along a 2 km coastal stretch at Egmond (The Netherlands), over an 18 month period starting December 1999 (Aarninkhof et al., 2005b).

Egmond is situated along the central part of the Dutch coast also known as the Holland coast. This coastal stretch has a length of about 120 km and mainly consists of dune areas, sandy beaches and multiple-barred nearshore zones. Egmond is located in the northern part of the central Dutch coast (Figure 10).

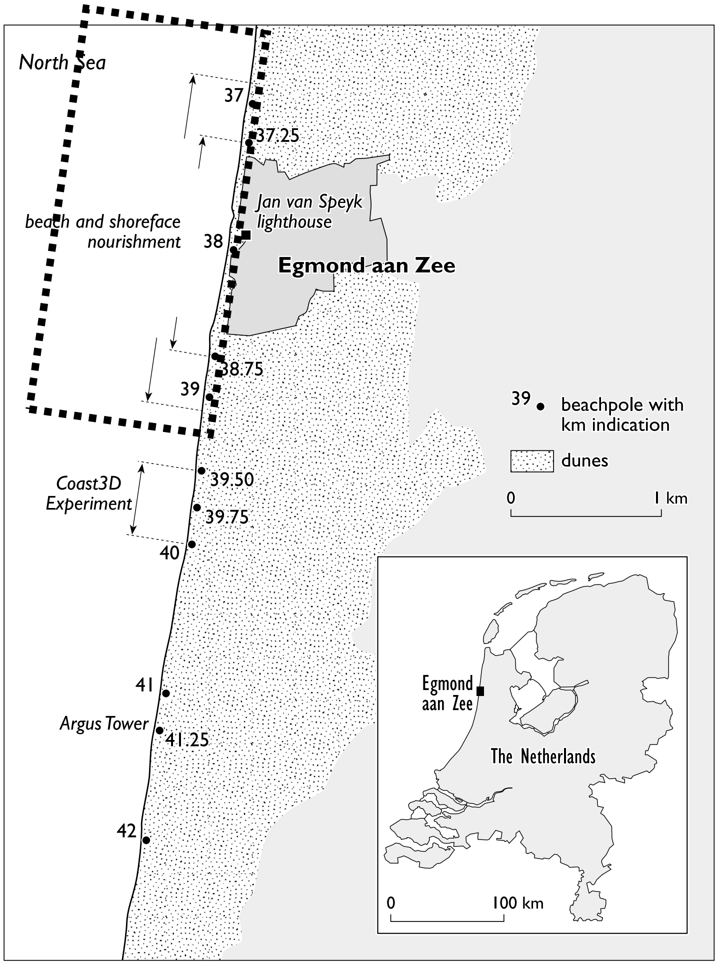

Figure 10: Location of Egmond along the Holland coast. The location of the model domain is indicated with the dashed black line.

The surf zone at Egmond is characterized by two shore-parallel subtidal nearshore sandbars. The crest of the outer bar is located at -3.5 to -4.0 m NAP (Dutch Ordnance Datum, approximately Mean Sea Level) and is fairly straight at times, but it often shows irregularities and some rhythmicities with typical length scales of several kilometres. The crest of the inner bar has an irregular alongshore planview with most of the time a crescentic appearance, and located at -1.5 to -2.5 m NAP (Van Rijn et al, 2002). The bars have a multi-annual lifetime during which they evolve in a periodic manner where the period is about 15 years (Ruessink et al., 2003).

Morphological changes along the storm-dominated Egmond coast are driven by a wave climate with a yearly mean wave height H_{mo} of 1.2 m and a mean period T_m of about 5 s, showing considerable seasonal fluctuations. Waves predominantly approach the shore from south-westerly and north-north-westerly directions (Wijnberg, 2002). The asymmetrical, semi-diurnal tidal curve induces northward directed currents during the four-hour flood period and southward directed currents during the 8 hour ebb period. The mean tidal range at Egmond is 1.68 m, with mean low tide at NAP -0.78 m and mean high tide at NAP +0.9 m. The tidal range is 2.0 m at spring tide, reducing to 1.4 m at neap tide.

During the 18 month assessment period, the WESP (Waves and Surface Profiler) was used to survey nearshore bathymetry twice per year, typically along 50 cross-shore profiles with 100 m spacing alongshore. The measured depth is estimated to have an error of less than 15 cm. Offshore wave conditions were measured with a directional wave buoy at IJmuiden, located approximately 15 km to the south of the nourished site. Approximately 50% of the missing data, which occurred during 15% of time, could be replaced by values from an identical buoy approximately 75 km to the north. Offshore tidal levels are found from interpolation in water level data collected at tidal stations located 15 km north and south of Egmond.

6.2.2 Model set-up

A model was set up along the lines of the model described in Wijnberg et al. (2004). The Flow model grid spans from -1400 to 1400 meters in y-direction (alongshore) and from -100 to 1200 meters in x-direction (cross-shore) in the local Argus coordinate system. The grid sizes Δx and Δy are 5 and 20 m respectively.

For each instance that assimilation data are present, the model is run in stationary roller mode for a duration of 2 hours. The simulation starts with a bathymetry measured on 14 and 15 September 1999. This measurement was not part of the annual JARKUS measurement campaign but was done for the sake of a local beach nourishment. At the offshore boundary, short wave energy and peak period (group speed) are imposed, the lateral boundaries are prescribed by the Neumann boundary condition. For the boundary conditions, tide level, wave height, period and direction are read from the Argus database and transformed to the depth at the model boundary. Wave directions are calculated by a Swan model, which is laterally extended with respect to the flow grid, to avoid discontinuities in the velocities. The model and instrument error settings were the same as in the Duck hindcast.

6.2.3 Data set

In this case, two assimilation sources are available for the modelled period, i.e. wave dissipation and intertidal bathymetry from video. We use the 100 wave dissipation maps as generated and used in Wijnberg et al. (2004), collected from 13/12/1999 until 20/07/2001.

Intertidal bathymetry files are constructed from the intertidal bathymetries derived from video. The Egmond application involves a compilation of two existing bathymetrical datasets of Egmond data generated by Caljouw (2000) and Nipius (2002) for the periods June 1999 – June 2000 and July 2000 – September 2001 respectively. Caljouw (2000) used a linear interpolator to map the shoreline sample points on the data grid, whereas all bathymetries after June 2000 were generated with the help of an advanced Loess interpolator (Plant et al., 2002). Due to variations in the spatial extent of the two datasets, only the overlapping region could be taken into account. This limitation reduced the intertidal study area to a 1360 m coastal strip centered around the Egmond light house and enclosed by the elevation contours at 0 m NAP and +0.9 m NAP. The overall Egmond dataset obtained consists of 27 intertidal beach bathymetries over the period 15/06/1999 until 22/09/2001.

6.2.4 Results

Figure 11 shows the results of the Egmond application for one cross-shore array (at y = 10 m in the local Argus coordinate system and corresponding to JARKUS array 03800, see Figure 17). The actual bathymetry was measured only five times during the model period. The measured bathymetry is indicated in blue (solid line) and the computed bathymetry in red (solid line). Initial values of both are shown with dashed lines. The computed uncertainty estimates are shown as cyan error bars.

The model predicts the overall bar-trough dynamics reasonably well (Figure 11). In the deeper regions (seaward of x = 700 m) the bathymetry is less dynamic. No assimilation data in this region is available, so the model does not update the bathymetry, unless wave conditions are very strong. The lack of local signals from the data also makes the uncertainty bands large, not necessarily because the computed bathymetry is far off the true bathymetry but simply because there is no way of knowing from the remote-sensed observations.

The model predicted errors (Figure 11) is very dependent on the moment in time we consider, but the error is smallest around the bar tops. Errors in the deeper regions remain large, because of the lack of data in these areas. In order to decrease these errors, inclusion of a third data source (for instance wave celerity) would be needed to increase model (data) uncertainty. For the model period, unfortunately no such data are available.

The 2-D results (Figure 12 and Figure 13) show that the rms error over the entire model domain generally lies between 0.5 and 0.6 m. The former approach (Aarninkhof et al., 2005b) resulted in an rms error of 1.2 to 1.5 m in the same model domain. Especially at the end of the computation and in the deeper regions, the present model approach shows a much smoother and more stable estimate of the bathymetry, which is in line with reality.

In Figure 14, the results are shown along the same two arrays as before, but now for the previous approaches (Aarninkhof et al., 2005b and Cohen et al., 2006), together with the present approach and the measurement. Large improvements have been made near the shoreline, the troughs and the outer bar compared with the Aarninkhof et al. (2005b) results. Bar heights are moderately better predicted with the present approach compared with the Cohen et al. (2006) results. However, this simulation was run without any site-specific tuning which means that the results are more robust than either of the previous ones.

Aarninkhof et al. (2005a) already showed that the model skill in predicting the bathymetry near the shoreline is small. The current assimilation method has improved the performance near the shoreline by including intertidal bathymetry as an assimilation source in the model. Also, the performance near the shoreline is improved because the overall performance in the bar-trough region is improved and the accumulation of errors towards the beach has decreased. Still, the model skill is lowest in these shallow areas.

During the summer months, the profile somewhat flattens and gets de-activated. The signal of the observed dissipation sources is weaker during summer months than in winter. This may cause the flattening of the profile. The profile becomes more dynamic during winter and this is very well predicted by the model.

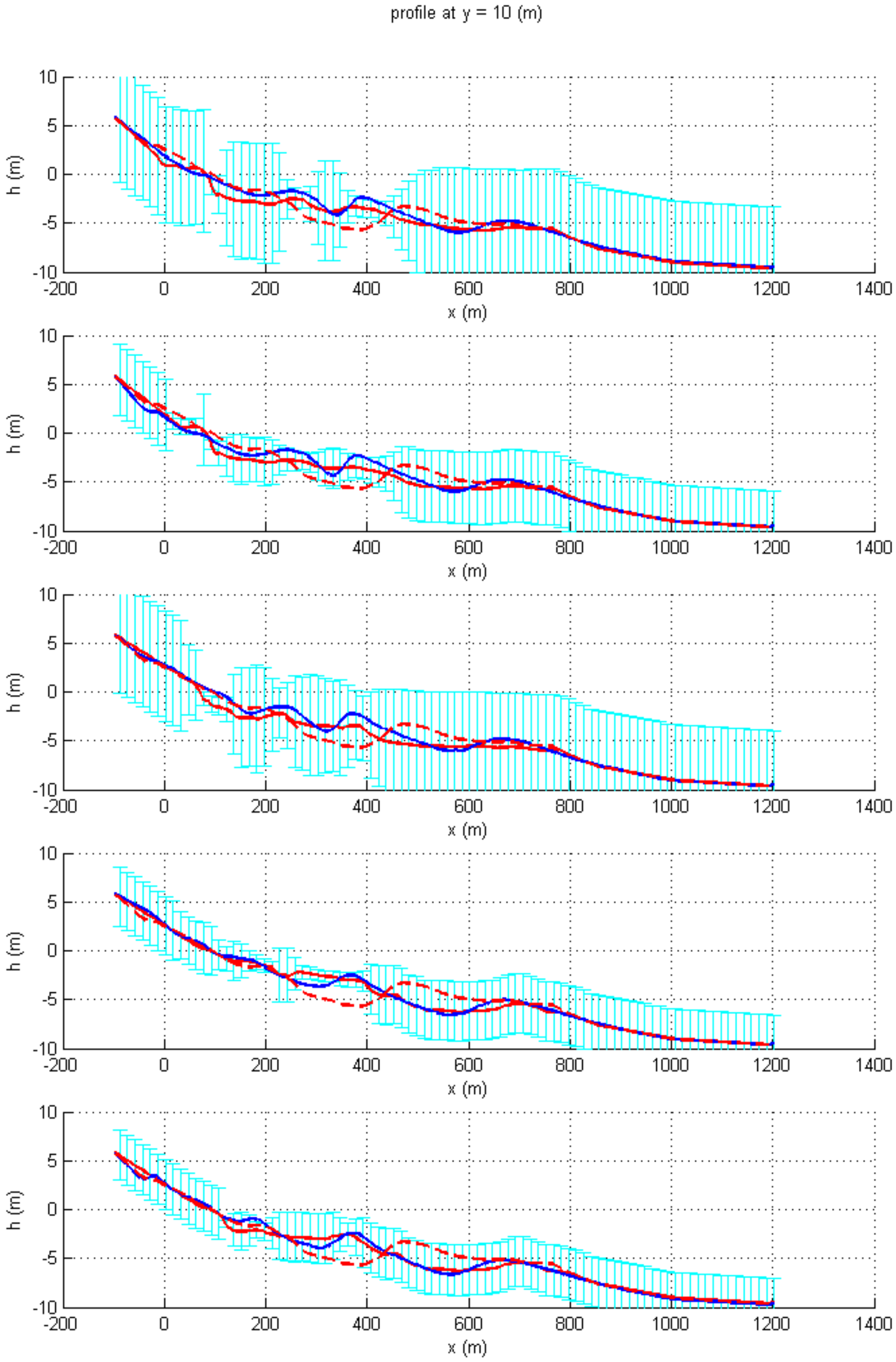

Figure 11: Results of the Egmond application at a cross-shore array (y = 10 m) at the five points in time during the model period when the bathymetry was measured (from top to bottom: 05/04/2000, 17/05/2000, 17/09/2000, 18/04/2001 and 18/06/2001). The blue line indicates the measured bathymetry, the red line indicates the computed bathymetry. Dashed lines indicate the initial situation of both. The model predicted errors are shown in cyan.

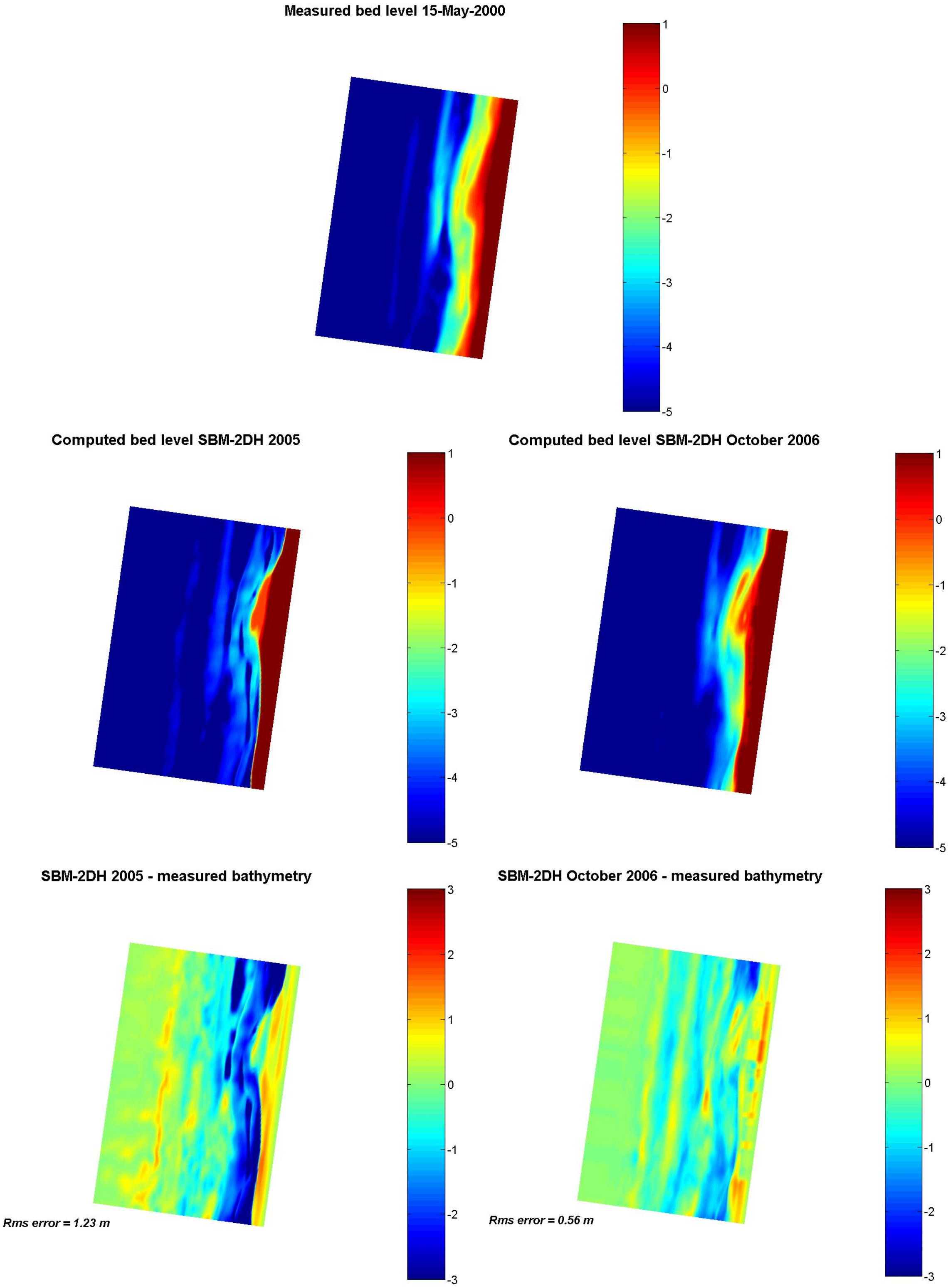

Figure 12: Results of the Egmond application in the model domain on 15 May 2000. The top panel shows the measured bathymetry. In the center panels show the computed bathymetries with the Aarninkhof et al., 2005 model (left) and the present model (right). The difference between the measured and computed bathymetries are shown in lower panels, together with the computed rms-error over the model domain for both models.

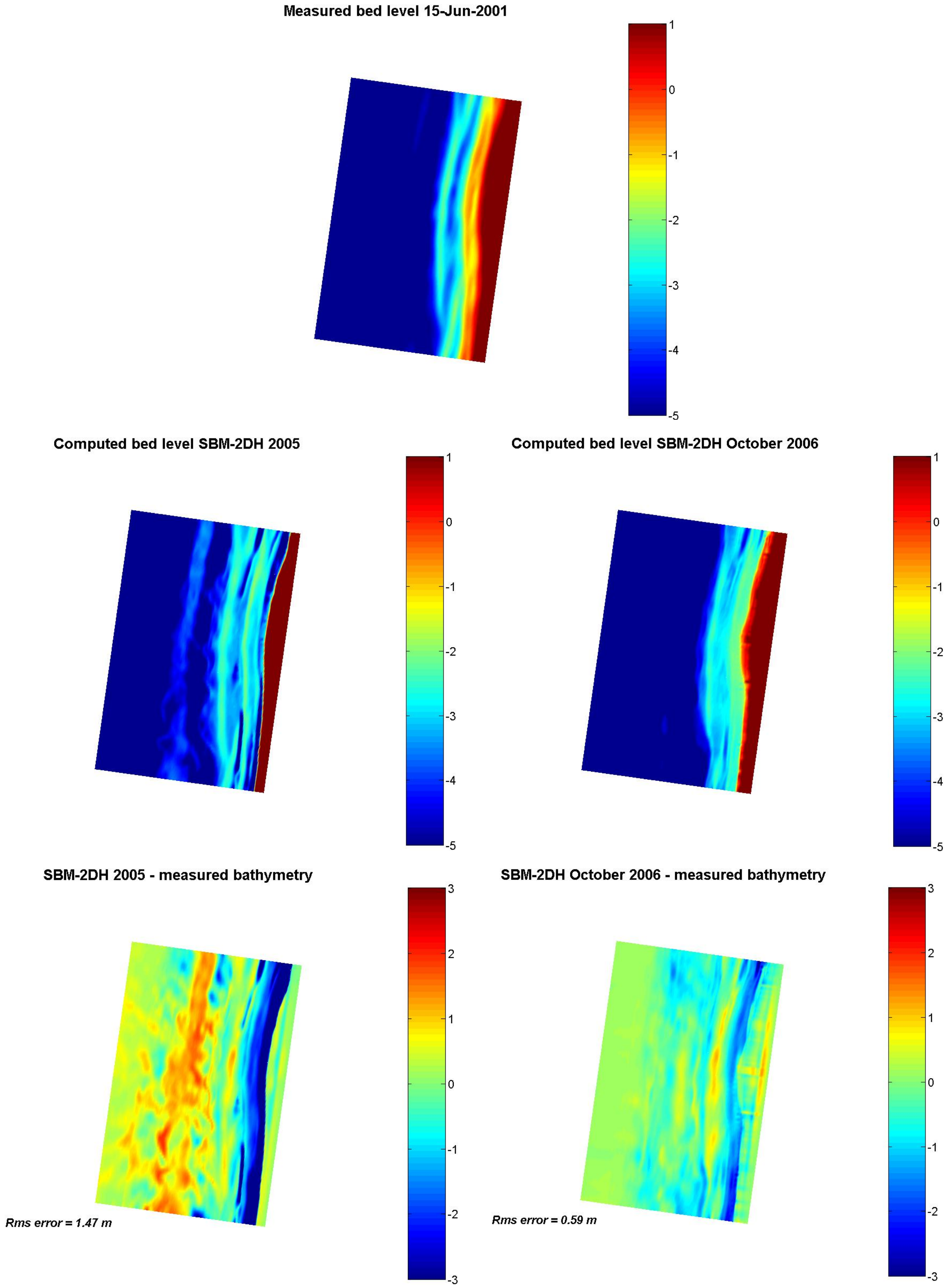

Figure 13: Results of the Egmond application in the model domain on 15 June 2001. The top panel shows the measured bathymetry. In the center panels show the computed bathymetries with the Aarninkhof et al., 2005 model (left) and the present model (right). The difference between the measured and computed bathymetries are shown in lower panels, together with the computed rms-error over the model domain for both models.

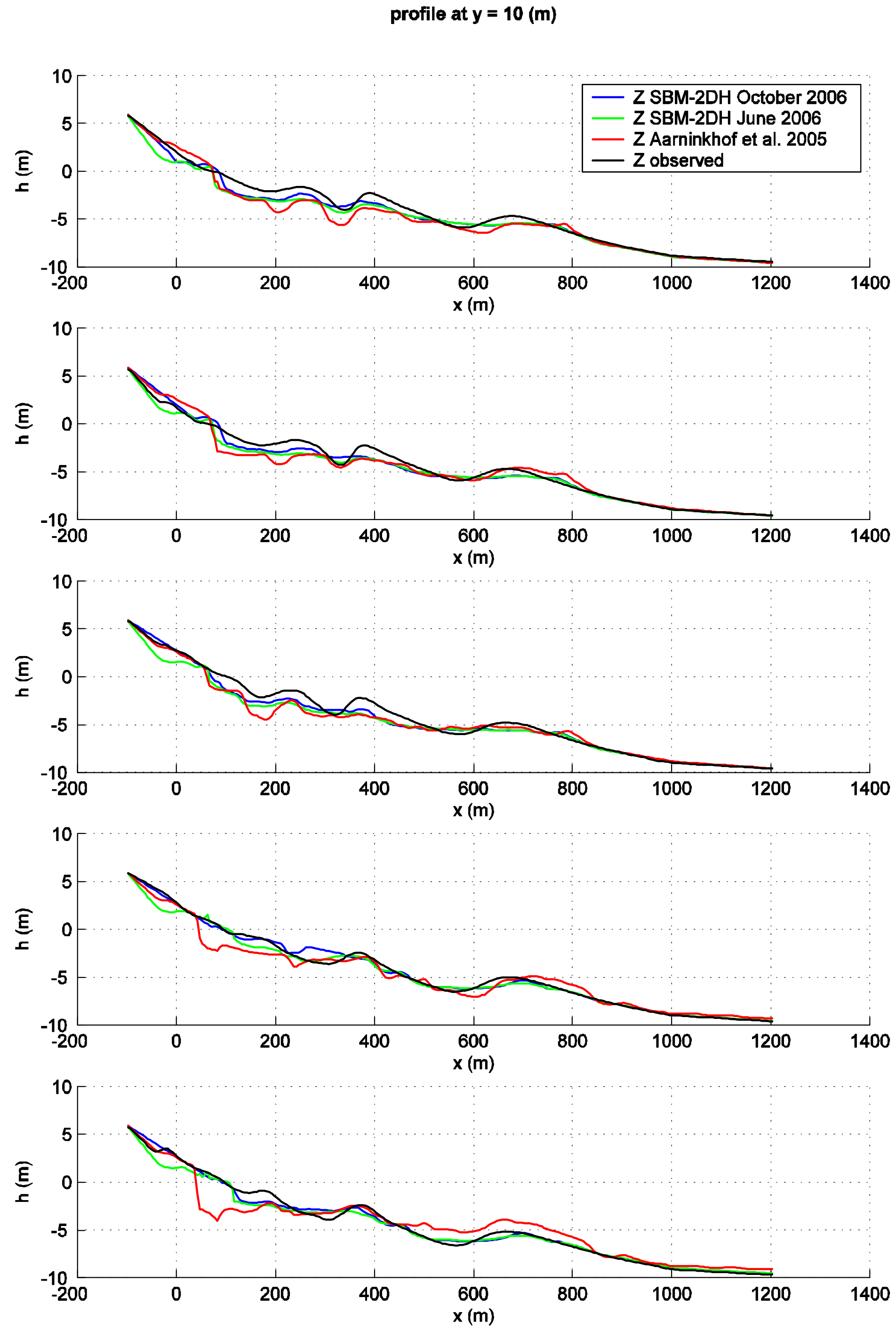

Figure 14: Results of the Egmond application at a cross-shore array (y = 10 m) at the five points in time during the model period when the bathymetry was measured (from top to bottom: 05/04/2000, 17/05/2000, 17/09/2000, 18/04/2001 and 18/06/2001). The black lines indicate the measured bathymetries, the red lines indicate the computed bathymetries from Aarninkhof et al. (2005). The green and blue lines indicate the computed bathymetries from the SBM-2DH June model and the present model respectively.

7 Estimation of coastal state parameters

7.1 Momentary Coastline

Coastal policy in the Netherlands has primarily been aimed at the protection against flooding of the lowland areas situated landward of the coastline. Since 1990 it has been official policy to stop any further coastal retreat by maintaining the coastline at the position of that date, adopting a new policy called ‘Dynamic Preservation’. The objective of this policy is to provide safety against flooding in combination with sustainable preservation of the functions and values of dunes and beaches. As it aims to take advantage of natural dynamic processes, the principal intervention measure is sand nourishment. Implementation of the Dynamic Preservation policy demands an objective assessment of the state of the coastal system. For this purpose, the concept of the Momentary Coastline (MCL) has been developed (e.g., Hamm et al., 2002).

The MCL (see Figure 15) represents the momentary horizontal position of the coastline, determined from the sand volume in a cross-shore profile between the dune foot at an elevation *H* above mean low water (mlw) and the depth contour at an equal depth *H* below mlw. The MCL is computed every year on the basis of annual surveys of bathymetry (named JARKUS for “JAaRlijkse KUStmetingen” or “Annual Coastal Surveys”) along cross-shore profiles with 250 m alongshore spacing. The anticipated position of the MCL for the next year is predicted from the ten-year trend in the evolution of the MCL and compared to the location of the so-called Base Coastline (BCL), which reflects the 1990 coastline and acts as the reference state. If the anticipated MCL is located shoreward of the BCL, an intervention by means of sand nourishment is necessary at that location. The MCL and BCL parameters are calculated using the UCIT Toolkit (Van Koningsveld et al., 2004).

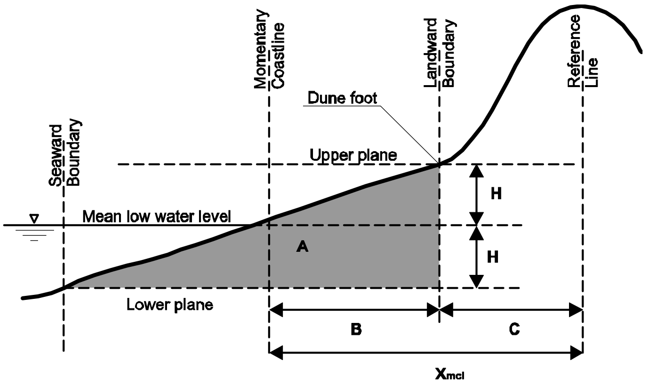

H = Height between dune foot and mean low water [m]
A = Momentary Coastline Zone [m^2]
B = A / 2H = Momentary Coastline position [m]
C = Distance dune foot to reference [m]
X_{mcl} = B + C = Momentary Coastline position + Distance dune foot to reference [m]

Figure 15: Definition sketch of the Momentary Coastline, MCL (Van Koningsveld and Mulder, 2004).

The Universal Coastal Intelligence Toolkit (UCIT), is an instrument that facilitates communication between decision makers and experts in coastal zone management problems. It does so by integrating various types of measurement data, morphological models and coastal state indicators (i.e. specific parameters on which decisions are based). A primary benefit of this approach is an increased efficiency in dealing with the 'traditional' coastal problems for which long standing approaches are used. A secondary but by no means lesser benefit is the creation of an environment where innovative technologies can be employed to supplement the traditionally derived information or even to generate new, previously unavailable, information in support of coastal management. Within the framework of the Beach Wizard project, the model results of the Egmond application are implemented in the UCIT environment, to facilitate simple comparison between model results and measured bathymetries, through derivation of several coastal state indicators from these bathymetries.

The JARKUS surveys are conducted in mild conditions during the spring or summer and do not resolve the intra-annual variability. The Beach Wizard assimilation model has in the above been shown to be capable to recover the bar-trough dynamics over an annual cycle is therefore applied to provide an estimate of this variability over the season in addition to the JARKUS measurements.

7.2 Bar position and height

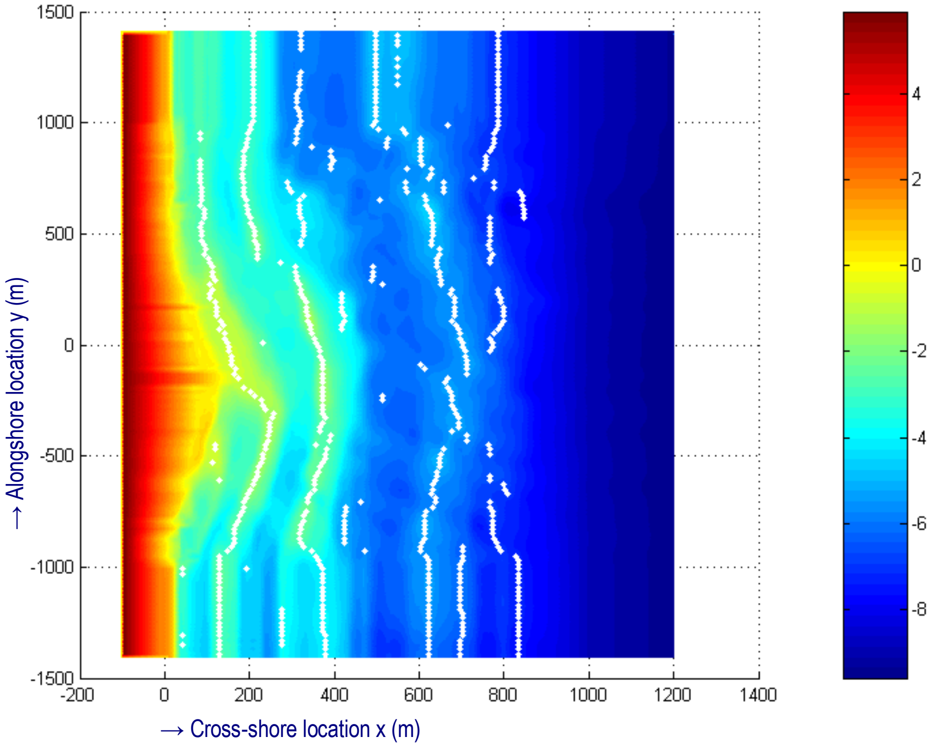

Figure 16: Bathymetry at Egmond with the bar locations given as white dots.

Besides the MCL, two more parameters are identified and calculated. The position of the bars is determined by finding the location of the local maxima in a cross-shore profile. The local maximum in each cross-shore area of 100 m is defined as a bar crest. The height of these crests can be easily found by taking the depth belonging to the location found. An example of the bar position calculated with this method is shown in Figure 16. The bar position and height are not yet used in Dutch coastal policy, but will show the behavior of the bars, as opposed to the MCL position. Understanding the behavior of nearshore bars is important for the understanding of the behavior of shoreface nourishments and the effects on the natural bar system. This understanding is needed for a founded design of these shoreface nourishments.

7.3 Comparison with JARKUS data

The MCL position and volume are determined with the method explained in section 7.1 at all the JARKUS transects that are located inside the Egmond model domain (transects 03675 – 03925, 11 in total). This is done for all the years that JARKUS data is present (each year, from 1965 – present) and for all the computation moments in the model period (120 in total, from December 1999 – July 2001). The results are shown in Figure 18a and b and in Appendix D. The transects shown in Figure 18a and b are located right in front of the Argus cameras (see Figure 17). In Appendix D, the computed and measured MCL positions in the remaining transects are shown.

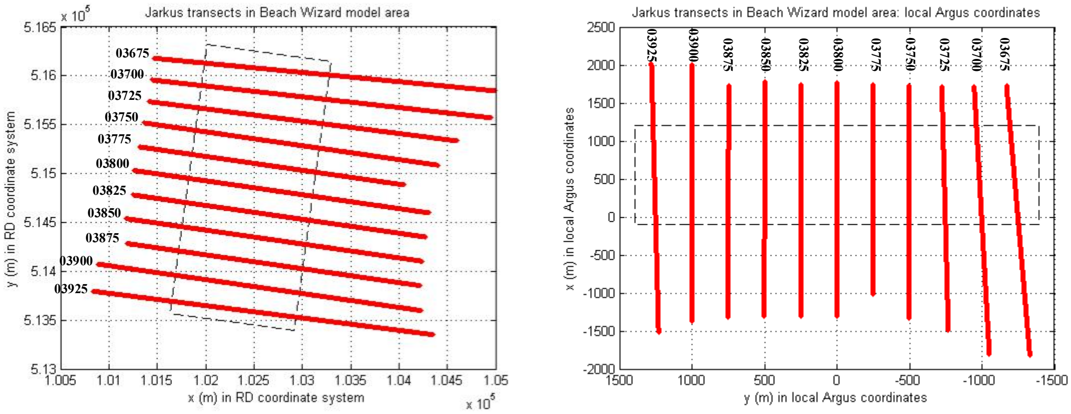

Figure 17: JARKUS transects (03675 – 03925) inside the Egmond model area in RD coordinates (left figure) and local Argus coordinates (right figure). In the Argus coordinate system, the orientation of the x-axis is shore normal, with the positive x-axis pointing in seaward direction. The y-axis is directed perpendicular to the x-axis, such that the co-ordinate system thus obtained is positive in mathematical sense. The latter means that the rotation from the x-axis towards the y-axis indicates the counter-clockwise (or 'positive') turning direction

The model computed MCL in Figure 18a and b shows the variability of this CSI through a year, while the JARKUS computed MCL only is determined once a year, mostly when conditions are moderate enough to measure the bathymetry (spring/summer). At the times that the JARKUS measurement and the model computations are simultaneous, the model computed MCL agrees quiet well with the measured MCL. An off-set can be seen in some transects, this is caused by the fact that the dry beach is not well represented in the modelled bathymetry, while it is more accurately measured in the JARKUS profiles. Because the dry beach is not the most dynamic part of the profile, this does not influence the MCL trend very much, but a small off-set may be caused by this. The measured profiles shown in Figure 20 are not regular JARKUS measurements, but additional WESP surveys conducted to monitor the behavior of the shoreface nourishment. In this study, the WESP measurements are extrapolated from the waterline to a set dune foot position in the same way as the model results. This is why the measured profiles do not show a beach behavior different from the behavior of the modelled beach.

More variability in MCL position and volume occurs in the model results through a year than the JARKUS measurements can capture. This implies that the JARKUS measurements do not represent the mean MCL location over a year. The MCL variability in a year is still in the range of the variability of the MCL over many years.

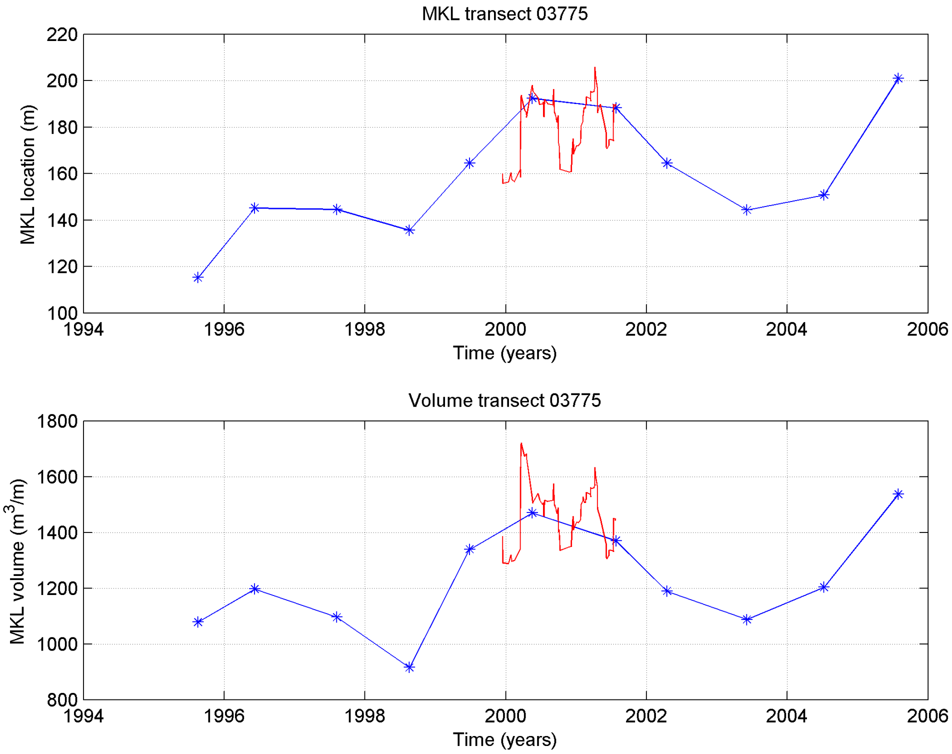

Figure 18a: MCL position and volume at JARKUS transect 3775 from JARKUS data (blue) and model (red). This corresponds to y=-250 m in the ARGUS coordinates.

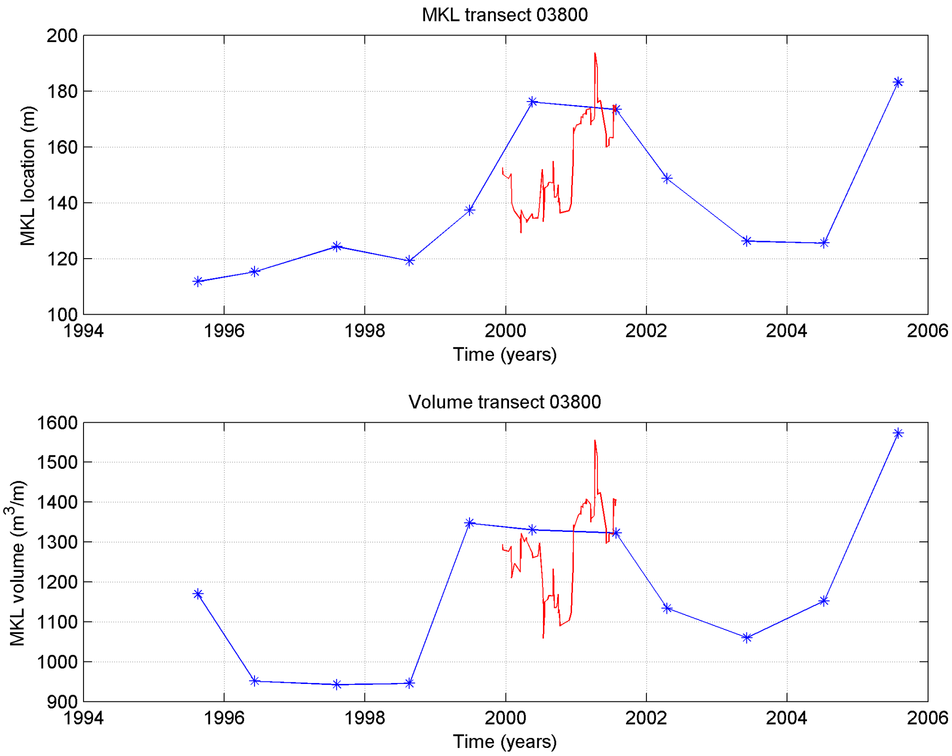

Figure 18b: MCL position and volume at JARKUS transect 3800 from JARKUS data (blue) and model (red). This corresponds to y=10 m in the ARGUS coordinates.

When we zoom in on the simulation period (Figure 19), we see that in the transition from strong to moderate wave conditions (start period 1, summer 2000), the MCL position remains stable or increases. During the summer of 2000 (period 1), the MCL position remains stable. Moving into a period of stronger wave conditions (period 2) at the end of 2000, the MCL position decreases. The final period indicates weaker wave conditions again, at the beginning of 2001 (period 3), where the MCL position increases in both cases. From this example array, it can be concluded that the MCL position varies due to the forcing of different (periods of) wave conditions.

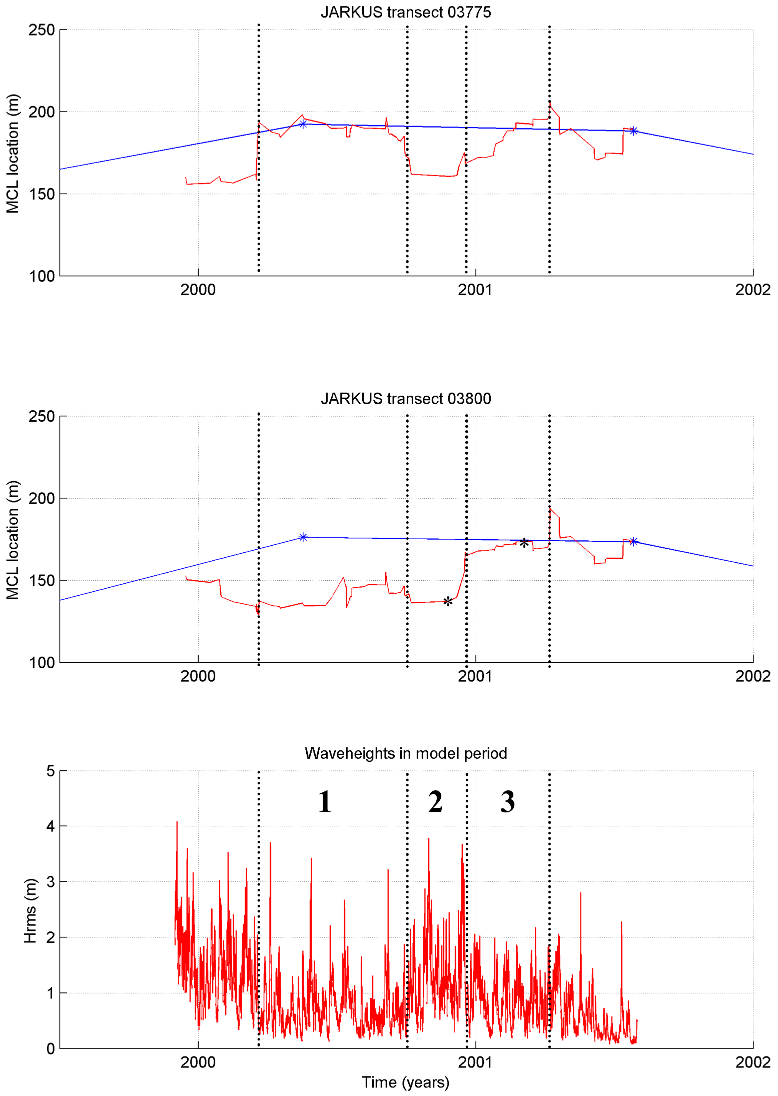

Figure 19: Wave height Hrms during the simulation period (bottom panel) together with the computed and measured MCL positions in JARKUS transect 03775 (upper panel) and 03800 (middle panel). Three different periods are indicated with number 1, 2 and 3 to analyse the results under different wave conditions. The two black stars in the middle panel indicate the times of a local minimum and maximum of the MCL volume/location (25 November 2000 and 22 February 2001 respectively) at which the cross-shore profiles of transect 03800 are shown in Figure 20.

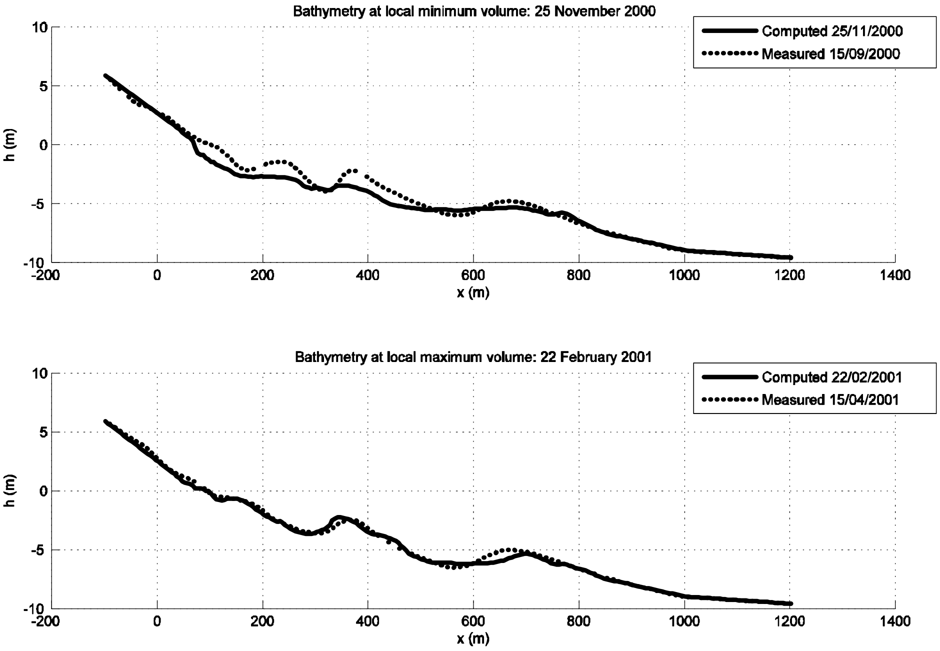

Figure 20: Cross-shore profiles at transect 03800 for two instants: top panel: local minimum of MCL volume on 25/11/2000 and bottom panel: local maximum of MCL volume on 22/02/2001. The nearest in time measurements (WESP surveys, not JARKUS) are also plotted.

From the figures in Appendix D it can be seen that for transects located further from the cameras, the model computed MCL shows a large dip at that moment that cannot be found in the MCL from JARKUS. In Appendix B, we see that the model starts deepening near the shoreline at the beginning of 2001. The dip in the MCL position is most likely caused by the erroneous deepening near the shoreline in the model away from the center of the domain and has no physical meaning. In this area, the quality of the assimilation data (video dissipation maps) needs to be improved to improve model performance.

Figure 20 shows the cross-shore profiles at transect 03800 at the times of a local minimum and maximum of the MCL volume (25 November 2000 and 22 February 2001 respectively, indicated with black stars in Figure 19). The figure shows that at the time of a local minimum the profile is flattened with some deepening near the shoreline with respect to the measurement nearest in time (WESP survey). The nearest measurement is before the storm season started, however, so it can not be said that the modelled bathymetry should exactly match the measurement. The mismatch though, may also be caused by the fact that this minimum is seen at the end of summer, after a period with weak signals in the video data, where we know that model skill is lowest. The cross-shore profile at the time of a local maximum MCL volume is at the end of the storm season and in good agreement with the measurement nearest in time (WESP survey). This is after a period with strong video signal and we see that the model skill is higher in this case.

Figure 18a and b, Figure 19 and Figure 20 give the impression that large volumes of sand (on the order of 300 m^3/m are lost or gained in the transects in rather small time spans. The question then arises where this sand goes. Figure 21 shows the MCL volume variation over the model period for five transects in the central part of the model domain. The transects show a simultaneous response to storms but often in the opposite direction, i.e. integrated over the whole domain less sand is gained or lost than the individual cross-sections would lead to believe. In fact, the sum net loss or gain of volume from 1/1/2000 to 1/1/2001 over the five transects is about zero. Sand is therefore not lost in the active zone of the beach profile but redistributed alongshore over a relatively short length of about 1000 meters in total. Still this variability may have important consequences for the management of the coastline since on short time and space scales the beach and shoreface are much more active than the JARKUS derived MCL locations can capture.

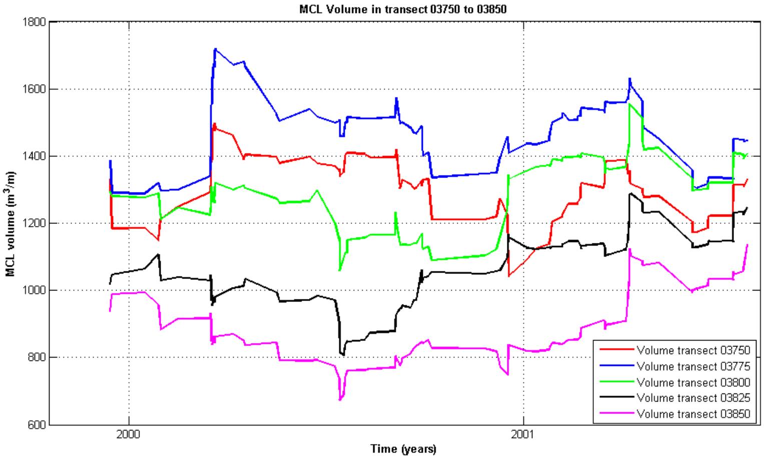

Figure 21: MCL volume variation over the model period for five transects in the central part of the model domain. Line colors are identified in the legend.

The bar locations and heights are computed at all the times that a bathymetry is computed with the model in the model period. These are plot against time at all the JARKUS transects in the model domain. Results are shown in Figure 22a and b and in Appendix E. The transects shown in Figure 22a and b are located right in front of the Argus cameras. In Appendix E, the computed and measured MCL positions in the remaining transects are shown.

We see that the position of the bars is very well predicted with the model. Positions remain fairly stable through the model period, but the heights of the shallower bars are dynamic. This can be seen from the model results, where we see that the model shows a increase of bar heights in the shallow parts, which is confirmed by the JARKUS measurement in 2001. In contrast to the MCL position, the skill of the model with respect to bar location and height does not decrease with distance from the Argus cameras. This supports the conclusion that the mismatch in MCL position at the beginning of 2001 is mostly caused by the erroneous deepening near the shoreline at transect further from the cameras. This deepening has no effect on the bar location and height.

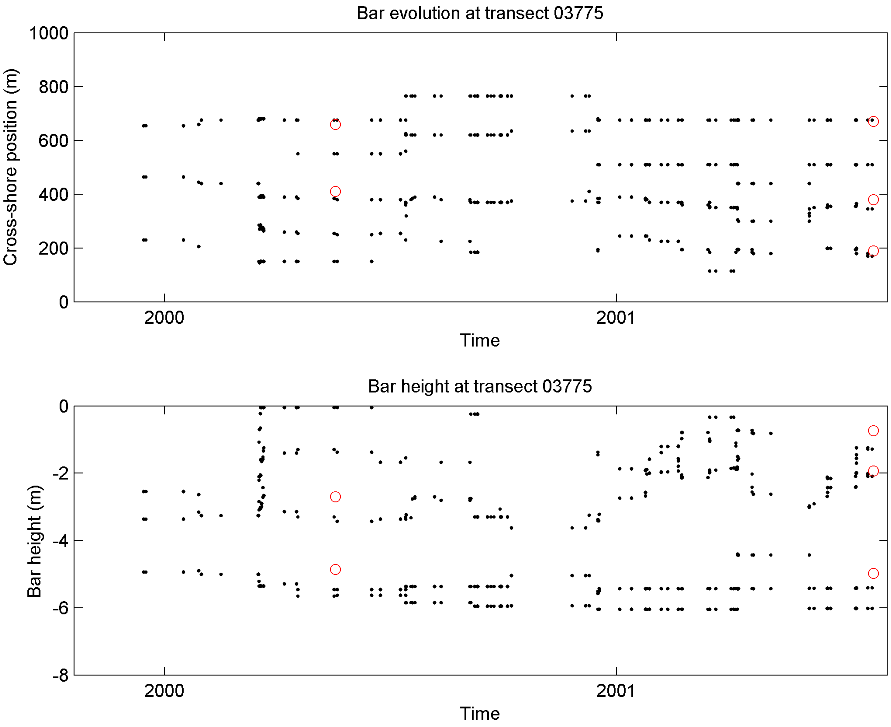

Figure 22a: Bar position and height at JARKUS transect 3800 from JARKUS data (red circles) and model (black dots).

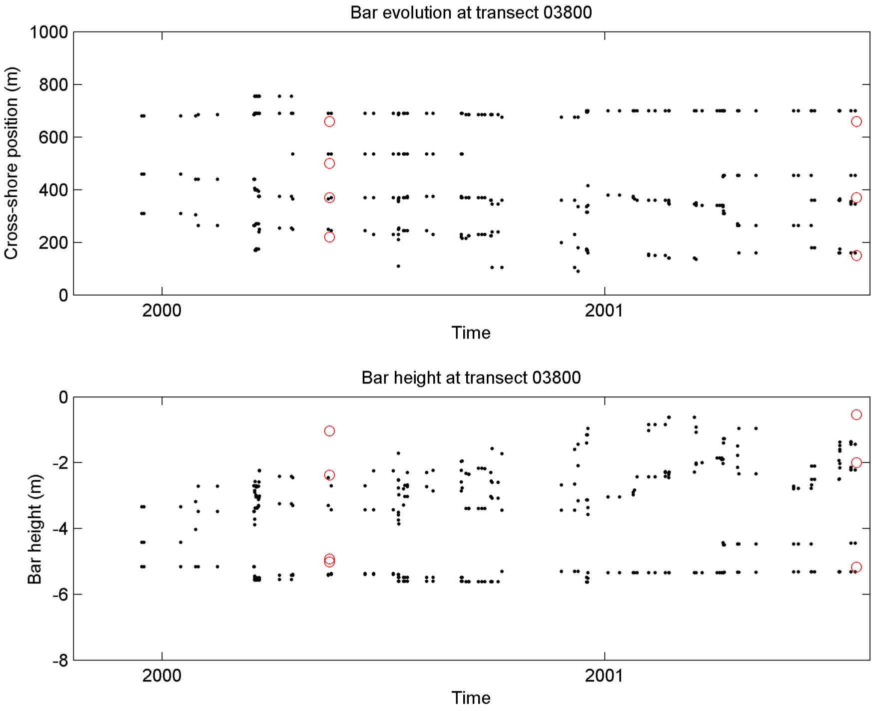

Figure 22b: Bar position and height at JARKUS transect 3775 from JARKUS data (red circles) and model (black dots).

8 Discussion

8.1 Applicability of Beach Wizard for Rijkswaterstaat purposes

This study has shown that the Beach Wizard can estimate the subtidal and intertidal bathymetry in the nearshore based on remote-sensed observations (presently from video and radar) with a rather low overall error, but some significant local deviations. The overall rms errors in Duck and Egmond are 0.4 m and 0.6 m respectively, with best results around the bars and worst results near the shoreline and over the bar(s) in the summer months. In those regions the error can be in the order of one meter. The study has indicated some issues yet to be resolved to remedy these problems (see below) but on the whole it has been proven to be a powerful and potentially cheap tool. The Beach Wizard can be of great use for Rijkswaterstaat for the following purposes:

- Estimation of the intra-annual variability of the coastal state indicators.

As been shown in the above, the intra-annual variability is rather large and on the scale of the long-term (several year) variability. This variability may have consequences for the decision to place a nourishment on a beach. This decision has hitherto been made based on the JARKUS data which appear to give a too optimistic local value of the MCL.

- Estimation of winter bathymetry for safety issues.

One aspect Rijkswaterstaat is responsible for is the calculation of the Hydraulic Boundary Conditions on the Dutch sea defenses, including the Holland Coast. These calculations are now performed on bathymetries which are based (among other sources) on the JARKUS data. As this data is not necessarily representative for a winter profile, the Beach Wizard estimates could provide additional information to provide alternative bathymetries.

- Monitoring of beach nourishments

The monitoring of the development of the coastal profile after a beach nourishment is of great interest to Rijkswaterstaat since this monitoring information can provide valuable data with which future nourishments can be placed more optimally. The Beach Wizard can provide a good alternative to extensive and expensive ground truth measurements which are now necessary to track the changes in the bathymetry.

- Forecasting of coastal recreational safety and use

The Beach Wizard can provide up to date estimates of the local bathymetry based on the latest video images. These images can be used to predict into the near future (order days or weeks) the (statistical likelihood of) the presence of breakers and rip currents. Smit et al. (2006) have shown promising results for the case of Palm Beach, Australia for this case. Rip currents are a major threat for swimmers, while the accurate prediction of breakers may be of benefit of surfers. This tool would require the operationalization of the Beach Wizard which has until now not been done.

The outstanding issues with respect to the Beach Wizard are outlined below.

8.2 Nearshore model behavior: terraces and digging

The Duck case has shown that at the shoreline a “terrace” builds up, while in the Egmond case the very nearshore area becomes deeper (“digging”). This effect is due to the same issue, namely that the bathymetric adjustment in the subtidal area is governed by the wave dissipation. Over a ray from offshore to onshore the wave dissipation has a history, which is not accounted for by adjusting the bathymetry due to local differences. For example, if in the true bathymetry a large bar exists, which is not present (yet) in the computational bathymetry, the model will correctly react by raising the bar in that area. However, due to the dissipation over the bar in reality, there will be less dissipation left in the nearshore area. There the model will react by deepening the bottom, which is possibly incorrect. This effect is illustrated in the following schematic. In the offshore area, over the true bar, the modelled depth will decrease correctly, but in the nearshore area the depth will become larger, incorrectly.

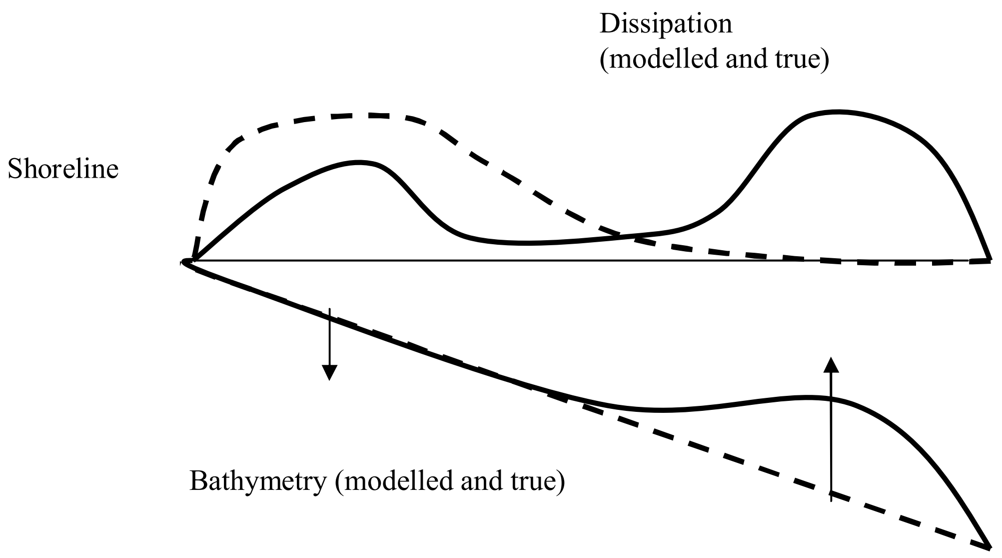

Figure 23: Schematic of a barred bathymetry (bottom solid line) and associated dissipation (top solid line), and the modelled bathymetry (bottom dashed line) and the modelled dissipation (top dashed line). The arrows indicate the direction of the adjustment of the modelled bathymetry.

The solution to this problem is to not use dissipation in the extreme shallow depth where is this the largest problem but to use another source, most notably observed phase speeds (bore speeds) of the broken waves. This can be done by incorporating information from video time stacks. The technique has been conceptually developed by Bos (2006) and the data is presently being collected already at Egmond.

This method of estimating the celerity can also be applied to the offshore area where there is no wave dissipation information (in the way we have applied radar data in this report). We strongly recommend implementing the video-derived celerities as obtained from the Egmond cameras in the Beach Wizard.

8.3 Trough behavior: persistent foam

At the end of the Egmond application, the model starts to fill in the trough at x=300 m. The cause for this may be found when taking a closer look at the data on which the model is assimilated. If we look at the driving force during the infilling of the trough (see Figure 24), we notice that the dissipation from video over the bar, seaward of the 'problem trough', shows a tail landward of the bar, when the computed dissipation does not. This difference generates an upward driving force landward of the bar, thus in the trough where we see the infilling.

The above mentioned dissipation tail may indicate the presence of persistent foam on the sea surface, which can be seen as an area of high intensity on a time exposure image. This, erroneously, gives the impression of wave dissipation, while it is just foam that was originally generated by wave breaking, but that remains at the surface for a while after the waves have dissipated. No relation between this whiteness in the time exposure images and the actual wave dissipation exists.

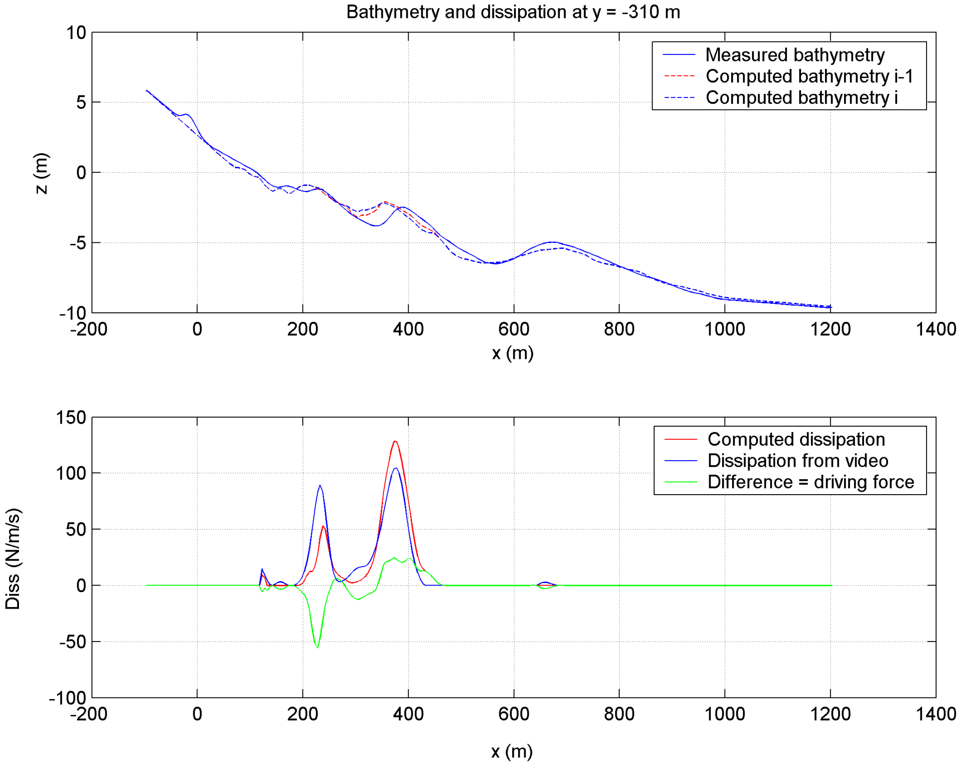

Figure 24: Computed bathymetry at y = -310 m on 06/04/2001 GMT 8.10 (i) and GMT 7.10 (i-1) with the dissipation signal at time i.

Aarninkhof (2003) has already seen this problem occurring in the 1-D version of the Beach Wizard model and has proposed a spatially varying reduction factor $f_{red}(x)$ which yields the cross-shore distribution of roller related image intensities I_{rol}.

$$f_{red}\left(x\right)=\frac{A_{rol}}{A_{br}\left(x\right)} \qquad (12)$$

The reduction factor is determined from the ratio between the roller related contribution A_{rol} to the increase of intensity I(x) and the integrated combined contribution A_{br} of both the roller and the persistent foam to the increase of I(x). Implementation of this formulation in the 2-DH model, presented in this study, may reduce the infilling effect in the troughs.

8.4 Farfield behavior: camera resolution

The results show that the data-model agreement deviates with increasing distance from the camera. This means that for a further extent of the model domain either more cameras have to be placed (at different towers) or other methods have to be applied such as radar (which also has a distance dependency of the illumination).

8.5 Operational and automated model

The input from the observed sources (dissipation maps, phase speed maps and intertidal bathymetry) are presently manually picked and processed. This labor adds to the cost of the model set up and delays the prediction time. In the future, an automated process should be defined for the Dutch situation based on the experiences from Dr. Todd Holland of NRL, USA. This, together with the incorporation of online wave and tide boundary conditions, can lead to an automated and operational model for a near-future (order days) forecast for the coastal bathymetry and the nearshore currents and waves. This is of benefit for coastal managers and for recreational purposes.

8.6 Error statistics

The error statistics defined in this study are a first attempt of defining the uncertainty. These statistics can be refined by incorporating a priori knowledge of the response of various sections of the bathymetry to waves and currents. This in effect leads to the replacement of the crude T_r parameter in Eq. (9) by a space-dependent parameter which depends on wave height and period.

9 Conclusions

In this report an assimilation model is presented which is capable of estimating the sub- and intertidal bathymetry based on the difference between remotely sensed quantities such as the roller energy dissipation rate, wave celerities and intertidal bed elevation and the corresponding computed quantities for a large number of time instances.

The present method is an improvement over the previous method by Aarninkhof et al. (2005a,b) because of the use of a gradient method with fewer free parameters and the incorporation of other sources than roller energy dissipation.

The model is validated for a synthetic case which shows that the assimilation scheme is capable of recovering a barred beach bathymetry starting from an initially plane beach and only “knowing” the dissipation rate and celerity fields.

The application to the Duck case shows that over a short time span (including one major storm) the model is capable of predicting the bathymetry rather accurately given a sequence of remotely observed inputs.

The model was then applied to the longer term case of Egmond. Here, the model is also capable of predicting the profile change with the same parameter settings as in the Duck case. The agreement is better for the winter months with stronger observed signals than in the summer months.

Finally, the model output is used to estimate Coastal State Indicators. The intra-annual behavior shows a large variability which is on the order of the long-term (decadal) variation that is captured by the annual ground-truth surveys. While the net sum gain or loss over an alongshore area is smaller than the variation over an individual cross-section, the fact that beaches are very active over short time scales may have consequences for coastal management.

The most important issues still to be tackled regarding the Beach Wizard model include weak nearshore and trough behavior of the model, improvement of error statistics and the practical use of the model (see Discussion). Solutions for better model behaviour nearshore and in the troughs can be found in the inclusion of breaking wave phase speeds nearshore and the implementation of a persistent foam formulation (Aarninkhof, 2003), respectively. The error statistics will be improved by incorporating a priori knowledge of the space-varying response of the bathymetry to waves and currents. The practical use of the model will be improved by operationalisation of the model through automatisation of the data selection and incorporation of online wave and tide boundary conditions.

10 Acknowledgments

Ap van Dongeren, Anna Cohen and Dano Roelvink were funded by Rijkswaterstaat under contract contract RKZ-1788 (number 450007226), building on concurrent funding by the Office of Naval Research under contract N000140510226 and the Dutch Ministry of Public Works Rijkswaterstaat, in the framework of the ‘Voortschrijdend Onderzoeks Programma VOP’ (Ongoing Research Program).

The Argus video technique has been developed with funds generated by the Coastal Imaging Lab, Oregon State University. The authors wish to acknowledge Prof. Rob Holman, OSU, for actively and generously stimulating the collaboration within the worldwide Argus research group.

A Derivation of derivatives per source

The bed update routine (Eq. 5) requires the computation of the gradients $\frac{df_{i,m}}{dh_m}$ for every source. For the three sources considered in this paper the evaluation is as follows

A.1 Celerity

If we choose the celerity as the quantity *f*=*c* and we need to calculate

$$\frac{dc}{dh}=\frac{d}{dh}\left(\sqrt{\frac{g}{k}\tanh(kh)}\right) \tag{A1}$$

using the linear dispersion relation in which *k* is the wave number at the peak frequency. Taking the derivatives with respect to h, and after some manipulation we find

$$\frac{dc}{dh}=\frac{2\pi f_p}{\cosh kh \sinh kh+kh} \tag{A2}$$

where f_p is the peak frequency

A.2 Roller dissipation

If we choose the roller dissipation as the quantity $f=D_r$. Because we cannot calculate $\frac{dD_r}{dh}$ straightforwardly we will calculate the derivative of the organized wave dissipation with respect to *h*, so $\frac{dD_w}{dh}$ as a proxy and we will use the dissipation formula of Baldock et al. (1998) because it is very accurate and straightforwardly differentiable with respect to *h.*

We will calculate this derivative in three stages by chain rule

$$\frac{dD_w}{dh}=\frac{dD_w}{d\Gamma}\frac{d\Gamma}{dH_b}\frac{dH_b}{dh} \tag{A3}$$

where

$$\begin{aligned}
D_w &= 0.25\rho g f_p H_{rms}^2 e^{-\Gamma}\left(1+\Gamma\right)\\
\Gamma &= \left(\frac{H_b}{H_{rms}}\right)^2\\
H_b &= \frac{0.88}{k}\tanh\left(\frac{\gamma kh}{0.88}\right)\\
\gamma &= 0.29+0.76kh
\end{aligned} \tag{A4}$$

Then

$$\begin{aligned}&\frac{\partial D_w}{\partial \Gamma} = -0.25\rho g f_p H_{rms}^2 \Gamma e^{-\Gamma}\\&\frac{\partial \Gamma}{\partial H_b} = 2\frac{H_b}{H_{rms}^2}\end{aligned} \tag{A5}$$

After some manipulation we find

$$\begin{aligned}\frac{\partial H_b}{\partial h} = &\frac{1}{\cosh^2\left(\dfrac{0.29kh+0.76(kh)^2}{0.88}\right)}\left[\left(0.29+2*0.76kh\right)\left(\frac{-kh}{\sinh kh\cosh kh+kh}+1\right)\right]\\&+\frac{0.88\tanh\left(\dfrac{0.29kh+0.76(kh)^2}{0.88}\right)}{\sinh kh\cosh kh+kh}\end{aligned} \tag{A6}$$

Eqs. (A5) and (A6) are collected and inserted into (A3).

A.3 Intertidal bathymetry

The modelled quantity is the intertidal height h_s. The gradient with respect to depth is simply unity.

B Results Beach Wizard Egmond at all JARKUS transects in model domain

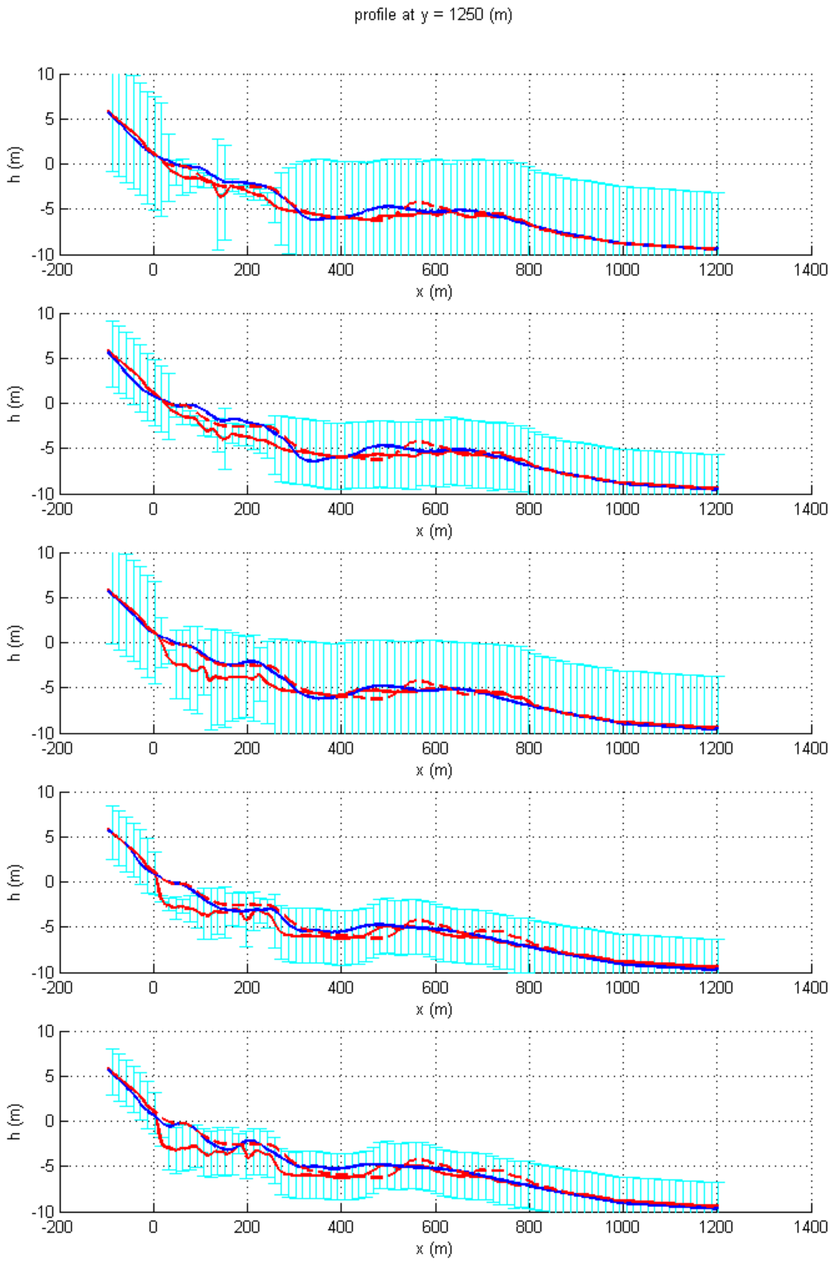

Figure 25: Results of the Egmond application at a cross-shore array (y = 1250 m) at the five points in time during the model period when the bathymetry was measured (from top to bottom: 05/04/2000, 17/05/2000, 17/09/2000, 18/04/2001 and 18/06/2001). The blue line indicates the measured bathymetry, the red line indicates the computed bathymetry. Dashed lines indicate the initial situation of both. The model predicted errors are shown in cyan.

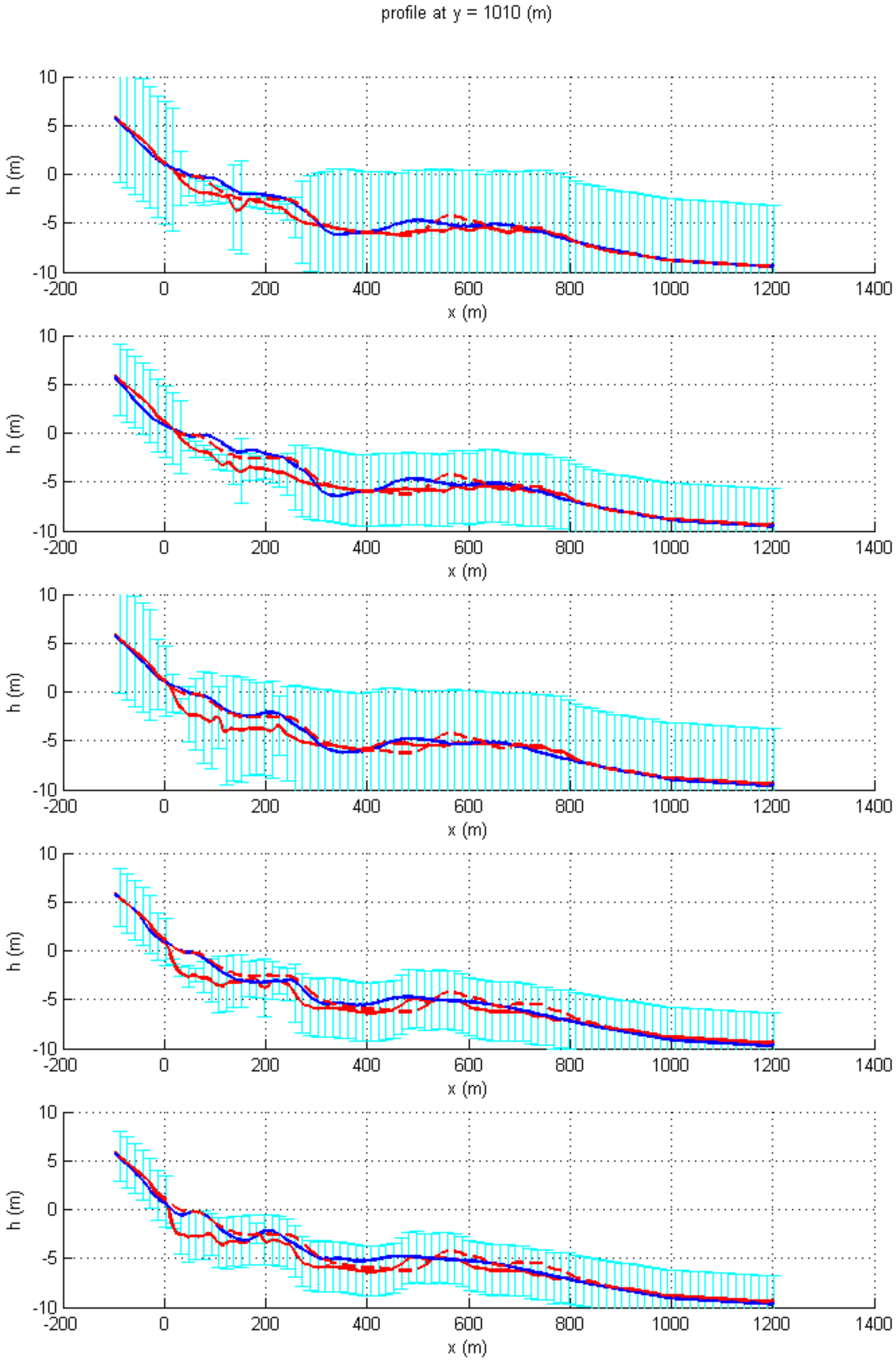

Figure 26: Results of the Egmond application at a cross-shore array (y = 1010 m) at the five points in time during the model period when the bathymetry was measured (from top to bottom: 05/04/2000, 17/05/2000, 17/09/2000, 18/04/2001 and 18/06/2001). The blue line indicates the measured bathymetry, the red line indicates the computed bathymetry. Dashed lines indicate the initial situation of both. The model predicted errors are shown in cyan.

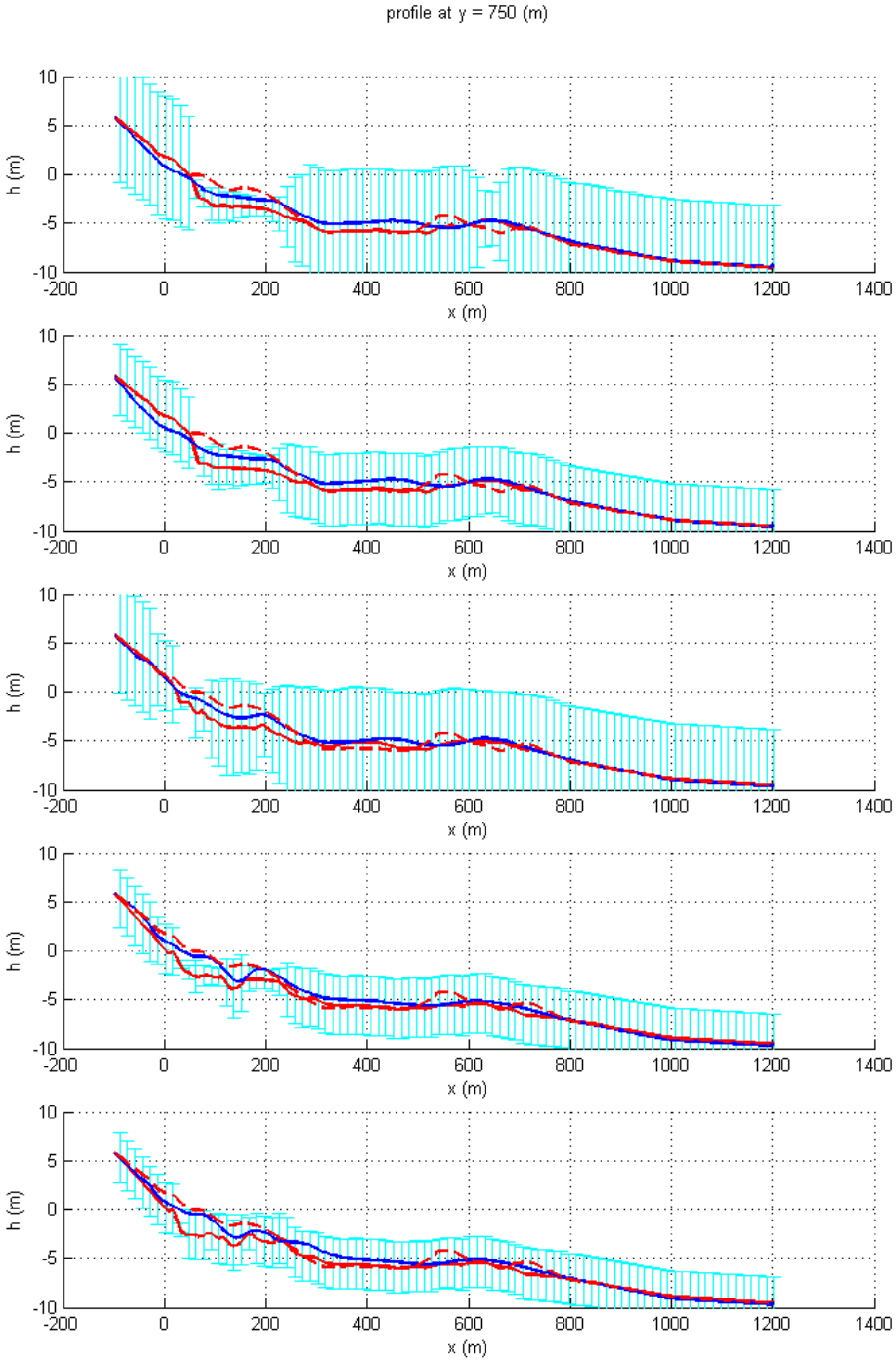

Figure 27: Results of the Egmond application at a cross-shore array (y = 750 m) at the five points in time during the model period when the bathymetry was measured (from top to bottom: 05/04/2000, 17/05/2000, 17/09/2000, 18/04/2001 and 18/06/2001). The blue line indicates the measured bathymetry, the red line indicates the computed bathymetry. Dashed lines indicate the initial situation of both. The model predicted errors are shown in cyan.

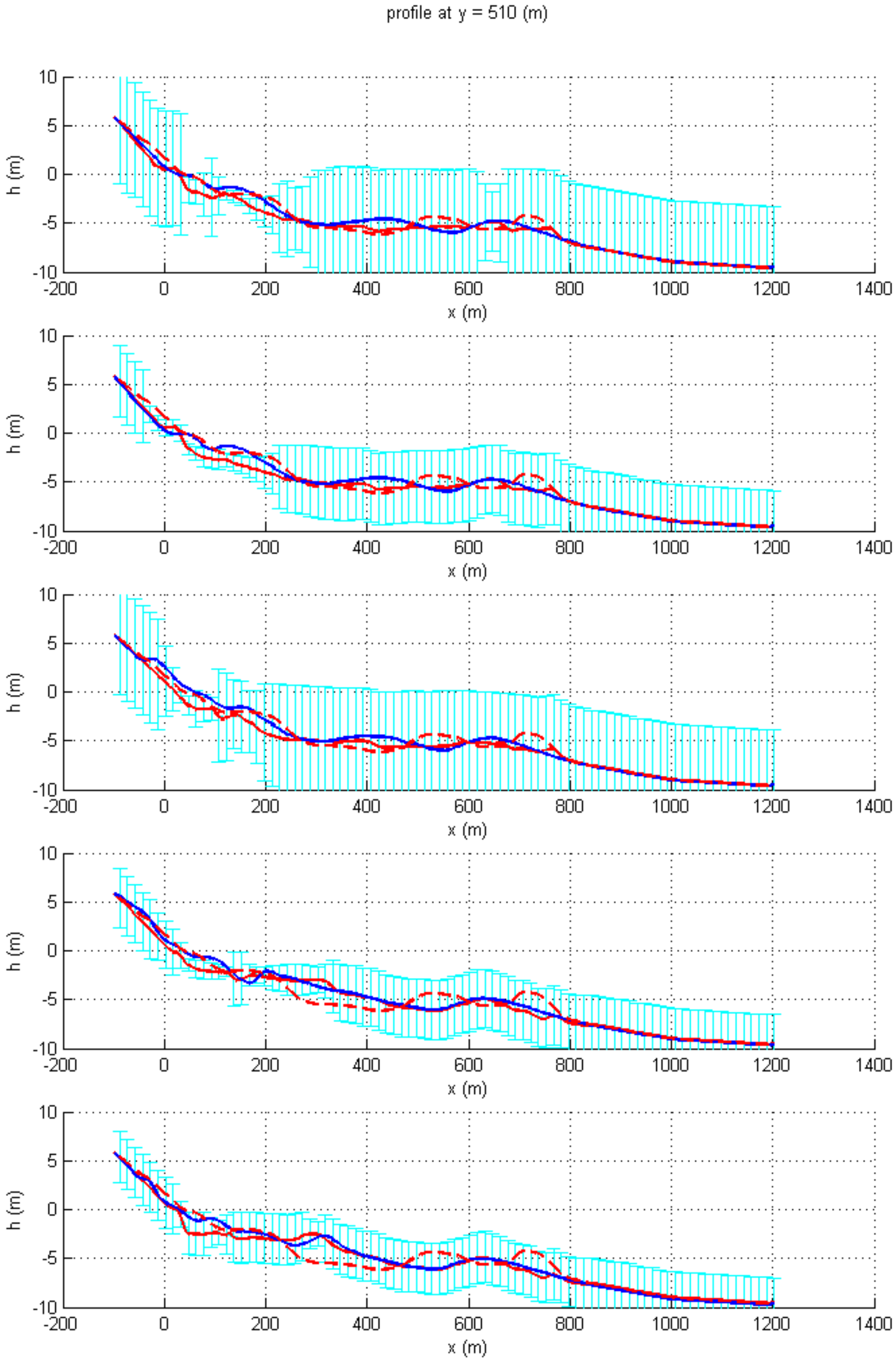

Figure 28: Results of the Egmond application at a cross-shore array (y = 510 m) at the five points in time during the model period when the bathymetry was measured (from top to bottom: 05/04/2000, 17/05/2000, 17/09/2000, 18/04/2001 and 18/06/2001). The blue line indicates the measured bathymetry, the red line indicates the computed bathymetry. Dashed lines indicate the initial situation of both. The model predicted errors are shown in cyan.

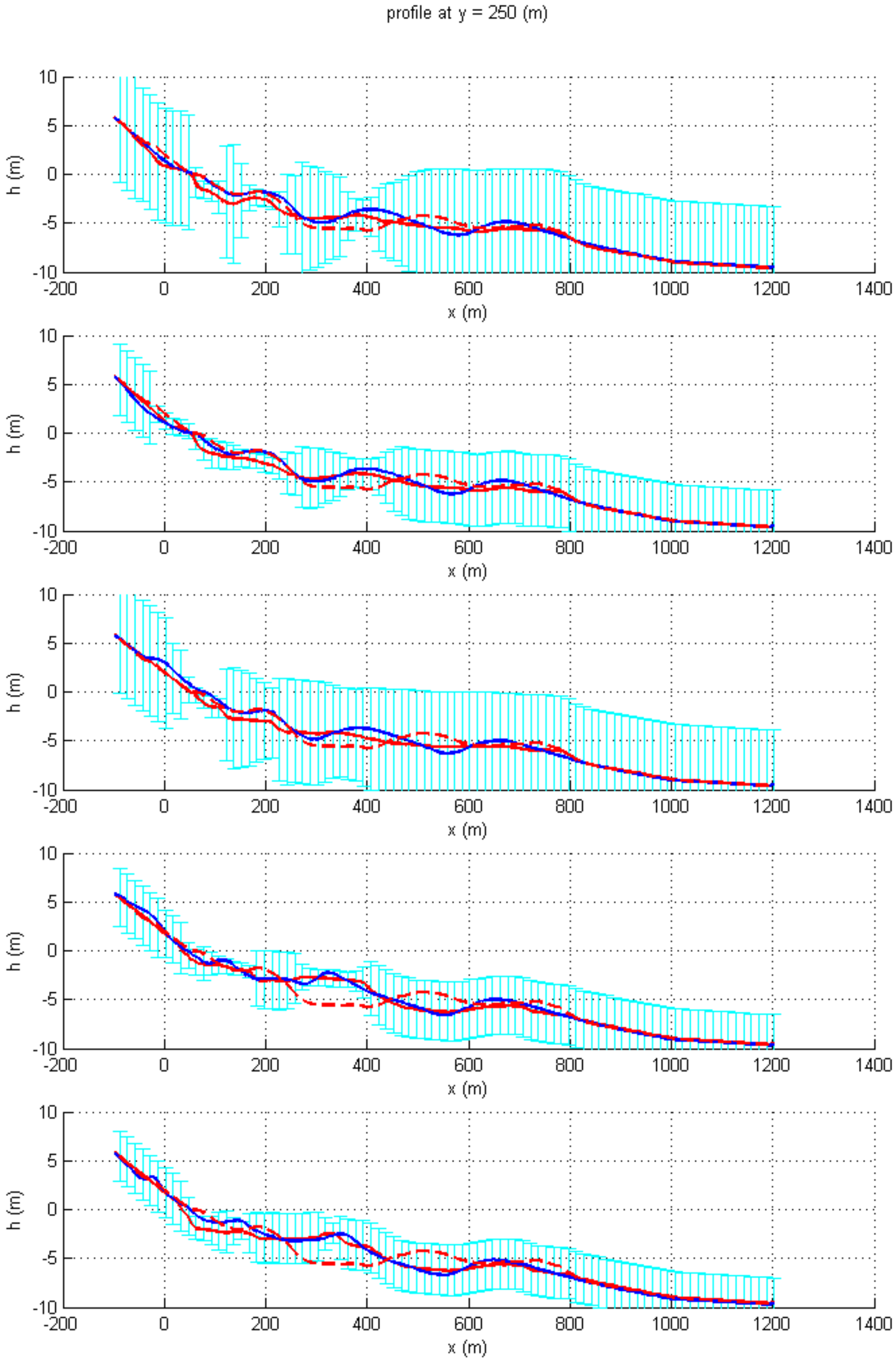

Figure 29: Results of the Egmond application at a cross-shore array (y = 250 m) at the five points in time during the model period when the bathymetry was measured (from top to bottom: 05/04/2000, 17/05/2000, 17/09/2000, 18/04/2001 and 18/06/2001). The blue line indicates the measured bathymetry, the red line indicates the computed bathymetry. Dashed lines indicate the initial situation of both. The model predicted errors are shown in cyan.

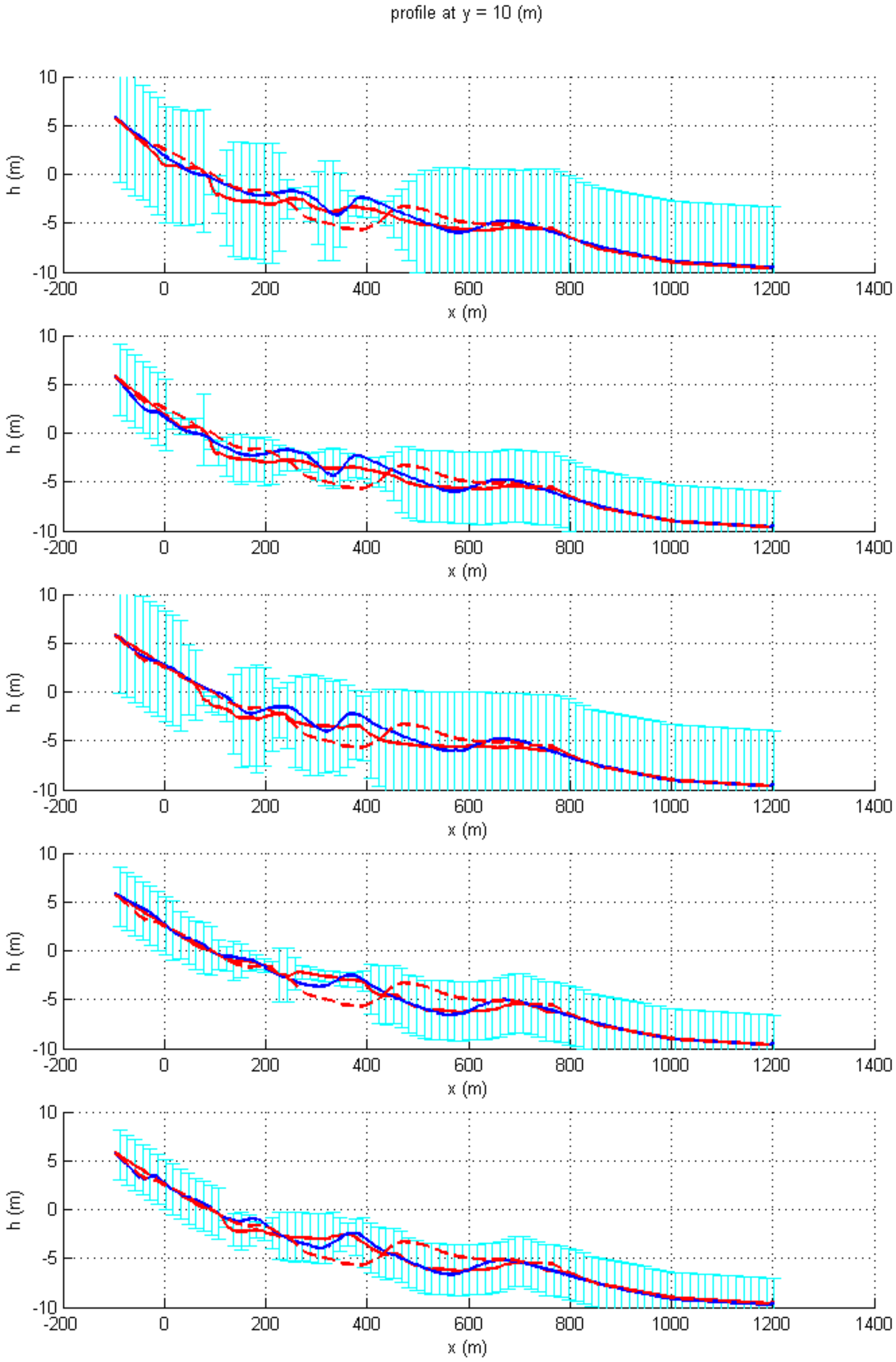

Figure 30: Results of the Egmond application at a cross-shore array (y = 10 m) at the five points in time during the model period when the bathymetry was measured (from top to bottom: 05/04/2000, 17/05/2000, 17/09/2000, 18/04/2001 and 18/06/2001). The blue line indicates the measured bathymetry, the red line indicates the computed bathymetry. Dashed lines indicate the initial situation of both. The model predicted errors are shown in cyan.

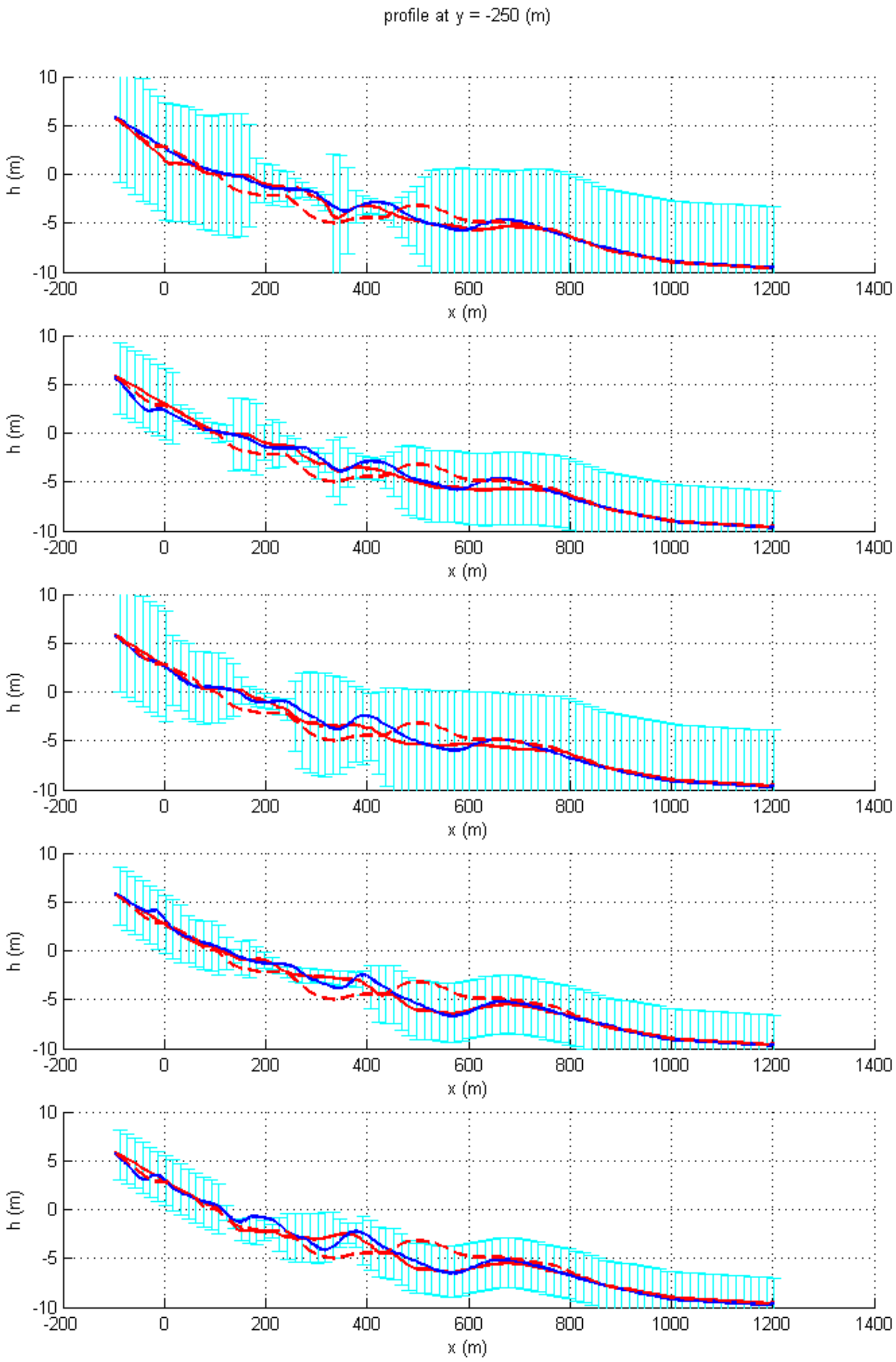

Figure 31: Results of the Egmond application at a cross-shore array (y = -250 m) at the five points in time during the model period when the bathymetry was measured (from top to bottom: 05/04/2000, 17/05/2000, 17/09/2000, 18/04/2001 and 18/06/2001). The blue line indicates the measured bathymetry, the red line indicates the computed bathymetry. Dashed lines indicate the initial situation of both. The model predicted errors are shown in cyan.

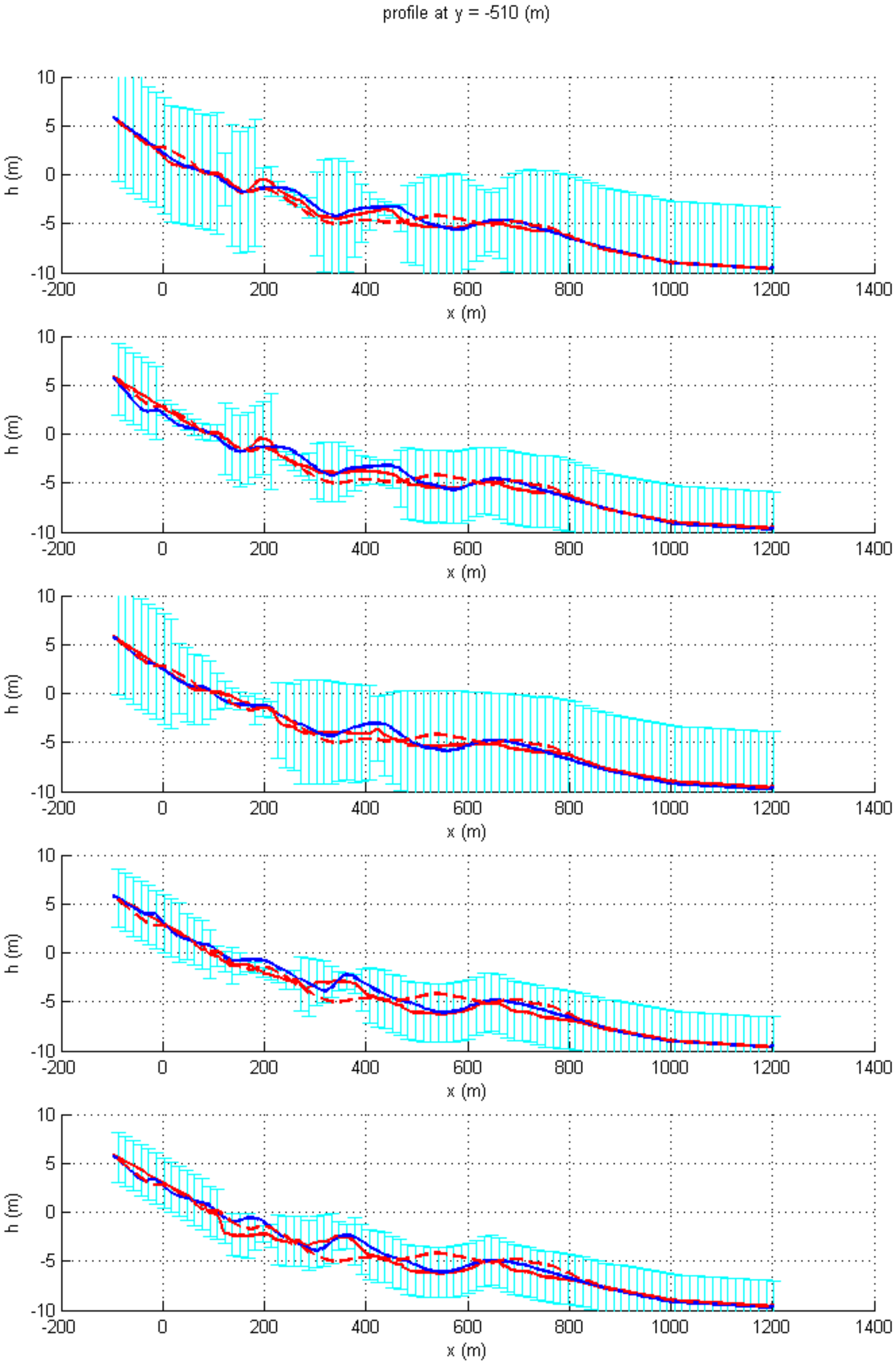

Figure 32: Results of the Egmond application at a cross-shore array (y = -510 m) at the five points in time during the model period when the bathymetry was measured (from top to bottom: 05/04/2000, 17/05/2000, 17/09/2000, 18/04/2001 and 18/06/2001). The blue line indicates the measured bathymetry, the red line indicates the computed bathymetry. Dashed lines indicate the initial situation of both. The model predicted errors are shown in cyan.

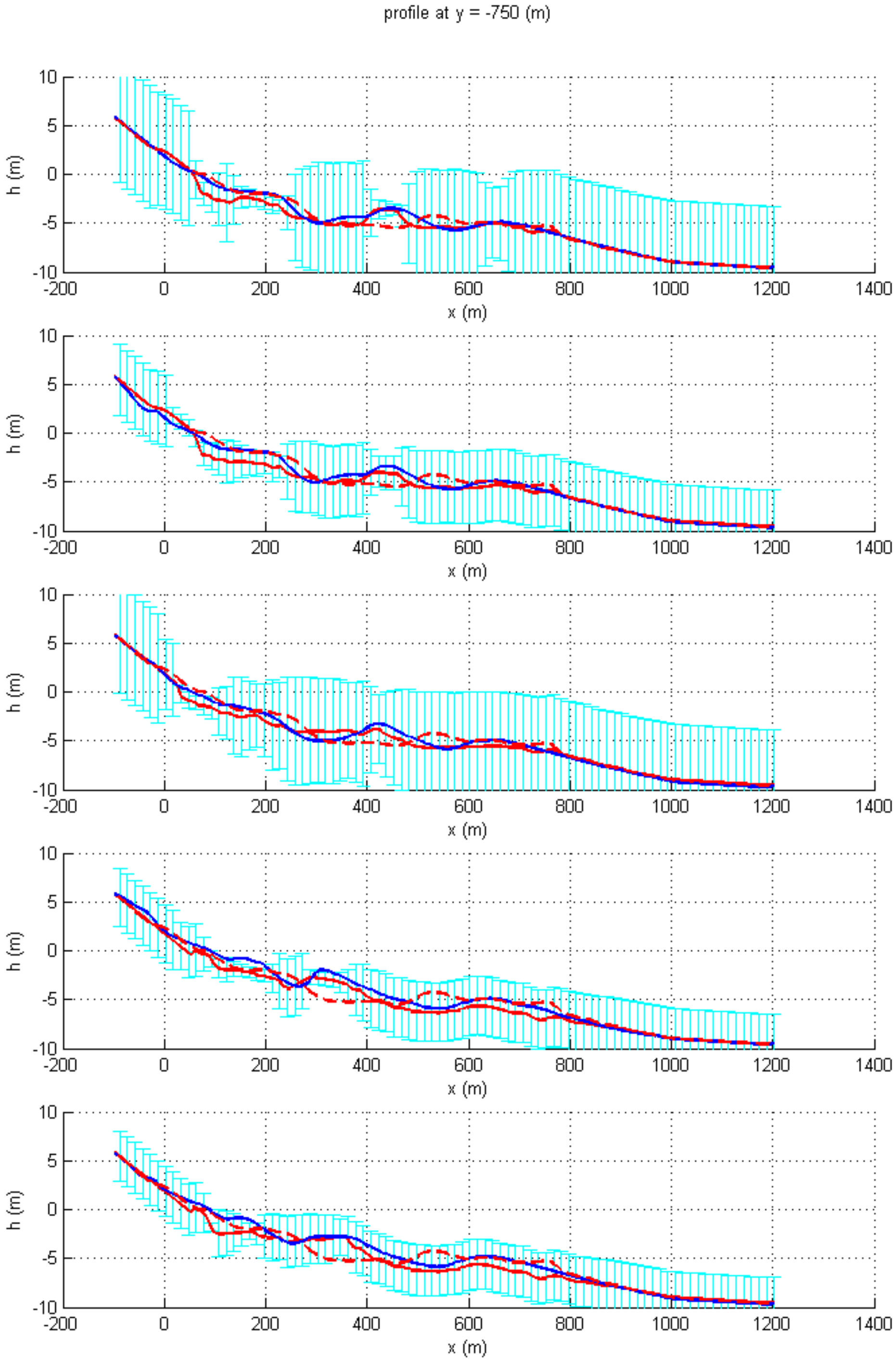

Figure 33: Results of the Egmond application at a cross-shore array (y = -750 m) at the five points in time during the model period when the bathymetry was measured (from top to bottom: 05/04/2000, 17/05/2000, 17/09/2000, 18/04/2001 and 18/06/2001). The blue line indicates the measured bathymetry, the red line indicates the computed bathymetry. Dashed lines indicate the initial situation of both. The model predicted errors are shown in cyan.

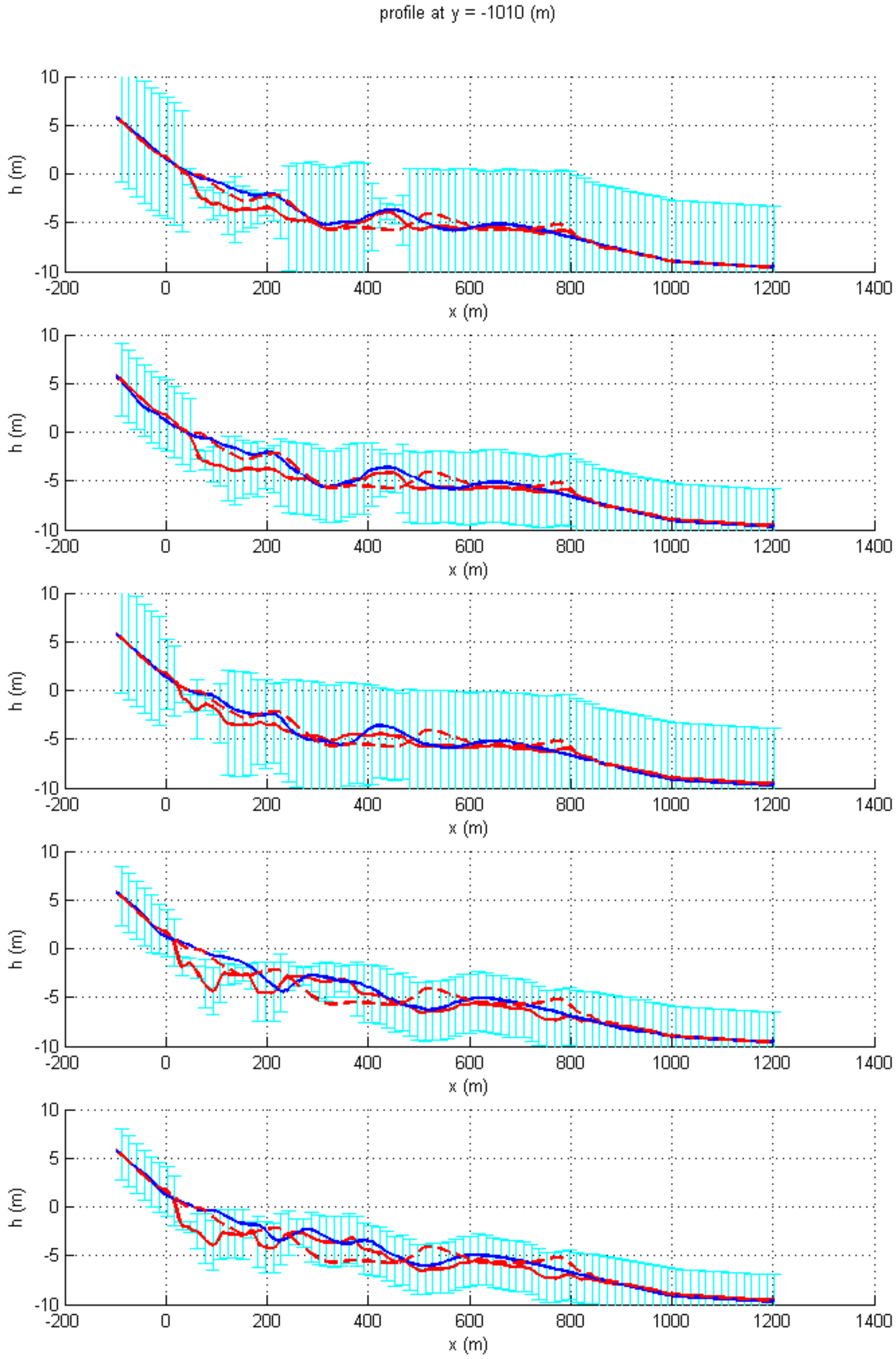

Figure 34: Results of the Egmond application at a cross-shore array (y = -1010 m) at the five points in time during the model period when the bathymetry was measured (from top to bottom: 05/04/2000, 17/05/2000, 17/09/2000, 18/04/2001 and 18/06/2001). The blue line indicates the measured bathymetry, the red line indicates the computed bathymetry. Dashed lines indicate the initial situation of both. The model predicted errors are shown in cyan.

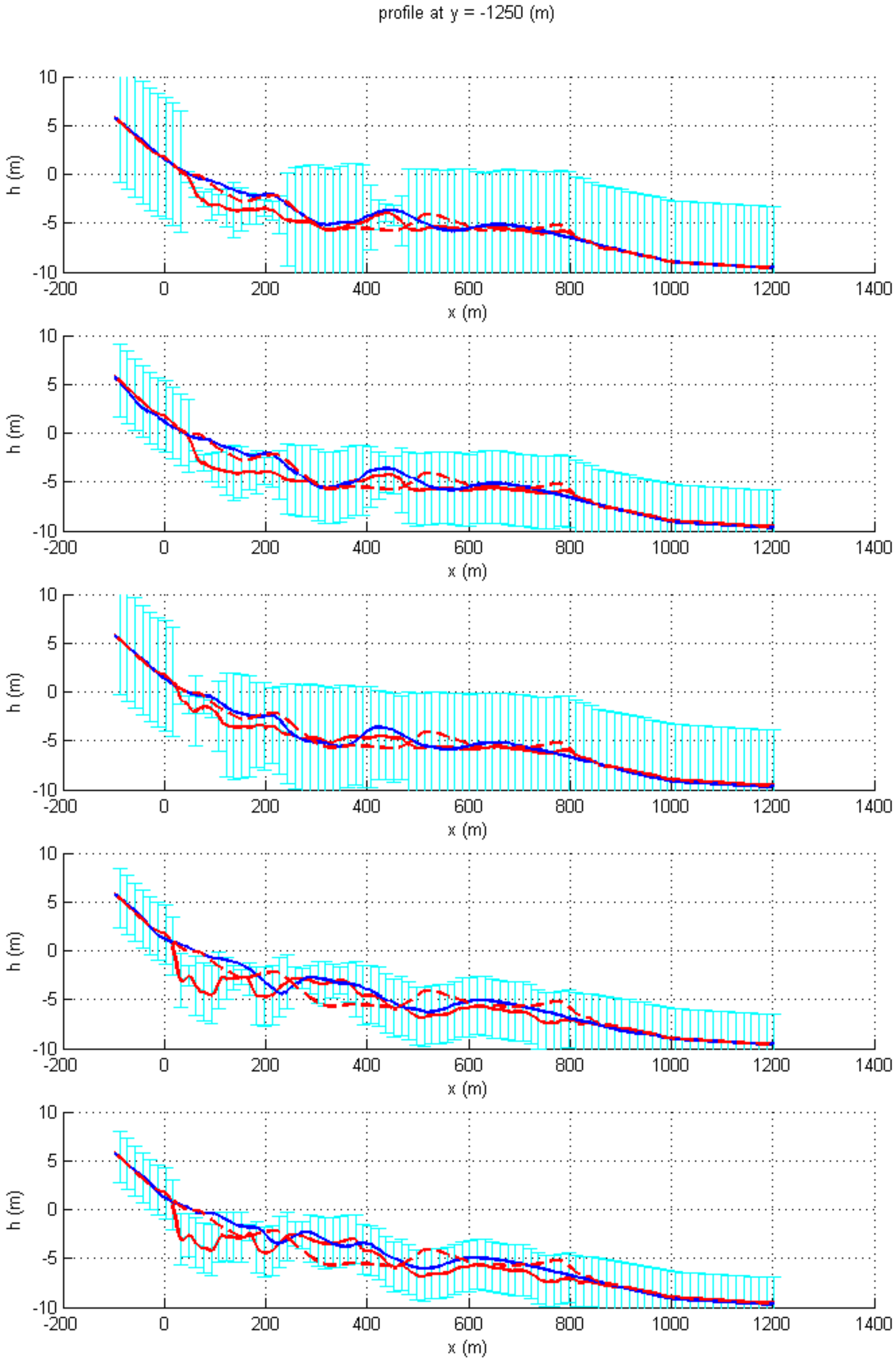

Figure 35: Results of the Egmond application at a cross-shore array (y = -1250 m) at the five points in time during the model period when the bathymetry was measured (from top to bottom: 05/04/2000, 17/05/2000, 17/09/2000, 18/04/2001 and 18/06/2001). The blue line indicates the measured bathymetry, the red line indicates the computed bathymetry. Dashed lines indicate the initial situation of both. The model predicted errors are shown in cyan.

C Comparison different Beach Wizard versions at all JARKUS transects in model domain

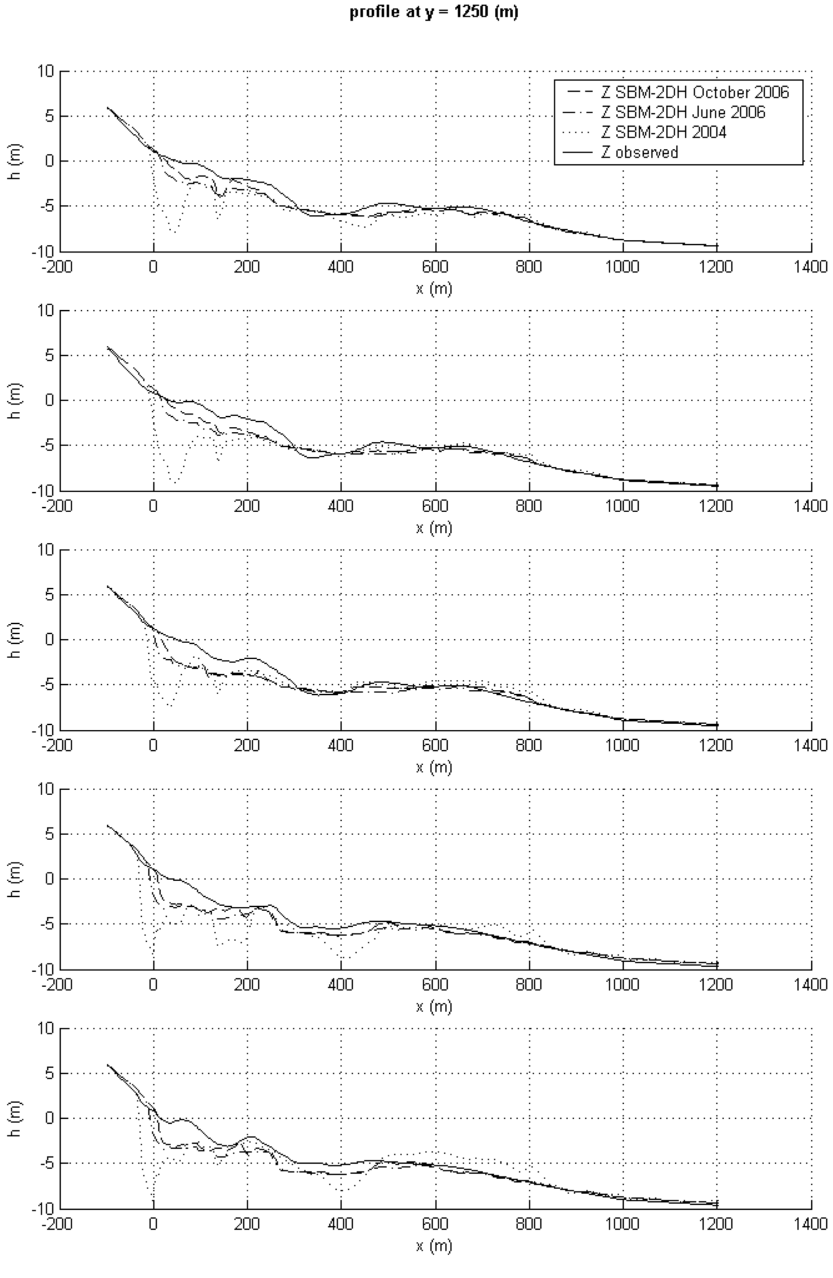

Figure 36: Results of the Egmond application at a cross-shore array (y = 1250 m) at the five points in time during the model period when the bathymetry was measured (from top to bottom: 05/04/2000, 17/05/2000, 17/09/2000, 18/04/2001 and 18/06/2001). The thick black line indicates the measured bathymetry, the thin black line indicates the computed bathymetry. The dash-dotted lines indicate the initial situation of both.

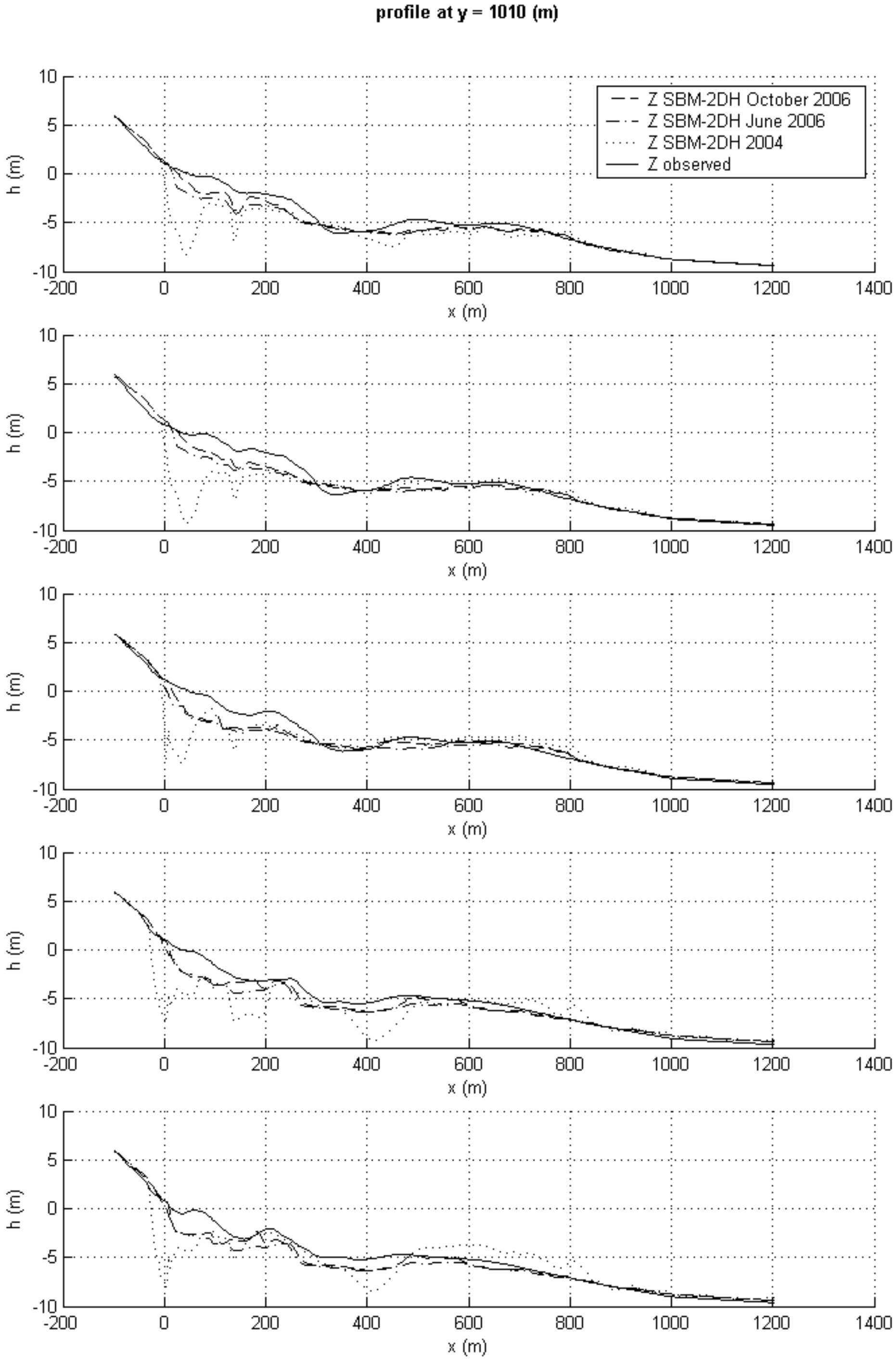

Figure 37: Results of the Egmond application at a cross-shore array (y = 1010 m) at the five points in time during the model period when the bathymetry was measured (from top to bottom: 05/04/2000, 17/05/2000, 17/09/2000, 18/04/2001 and 18/06/2001). The thick black line indicates the measured bathymetry, the thin black line indicates the computed bathymetry. The dash-dotted lines indicate the initial situation of both.

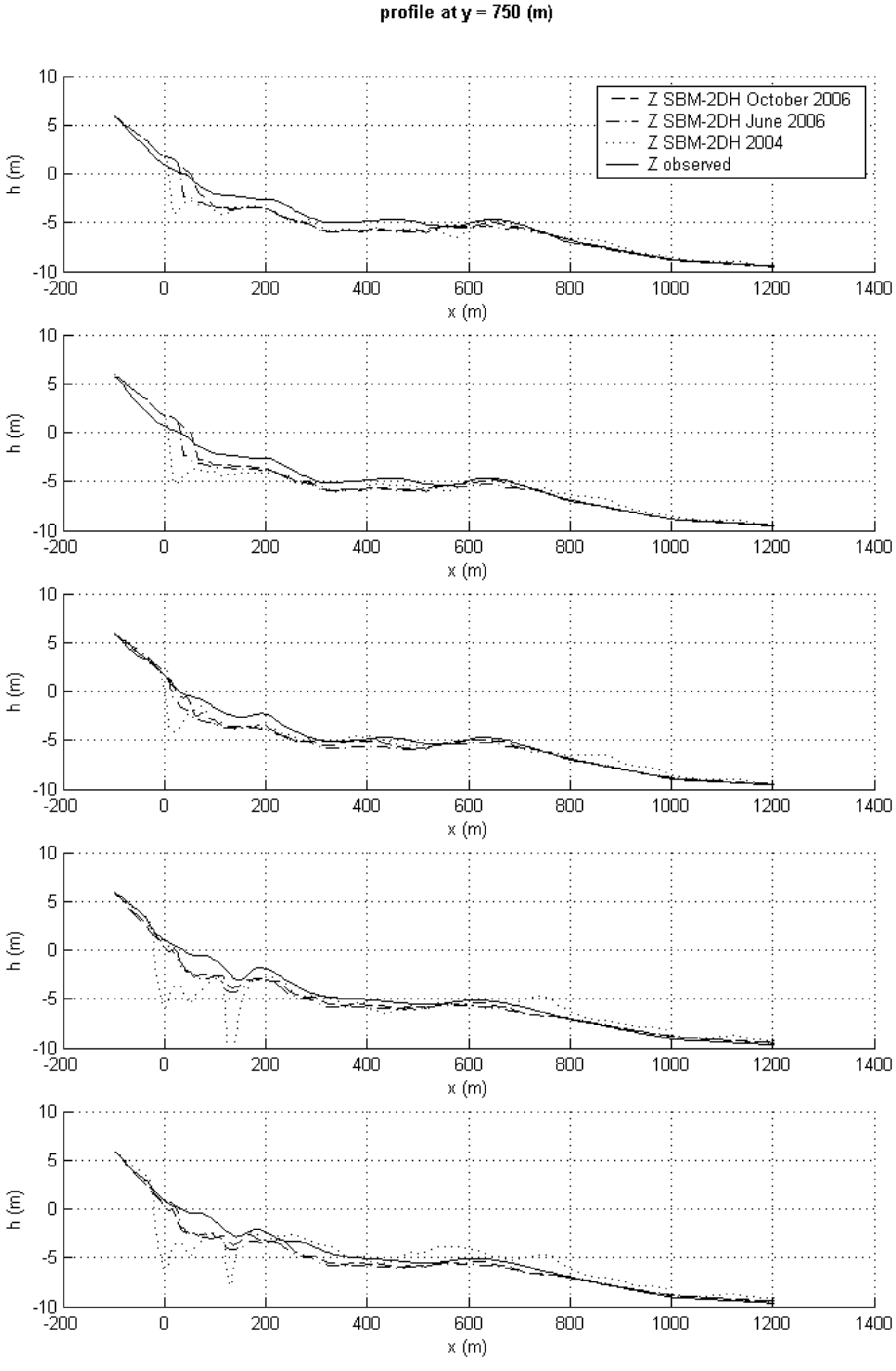

Figure 38: Results of the Egmond application at a cross-shore array (y = 750 m) at the five points in time during the model period when the bathymetry was measured (from top to bottom: 05/04/2000, 17/05/2000, 17/09/2000, 18/04/2001 and 18/06/2001). The thick black line indicates the measured bathymetry, the thin black line indicates the computed bathymetry. The dash-dotted lines indicate the initial situation of both.

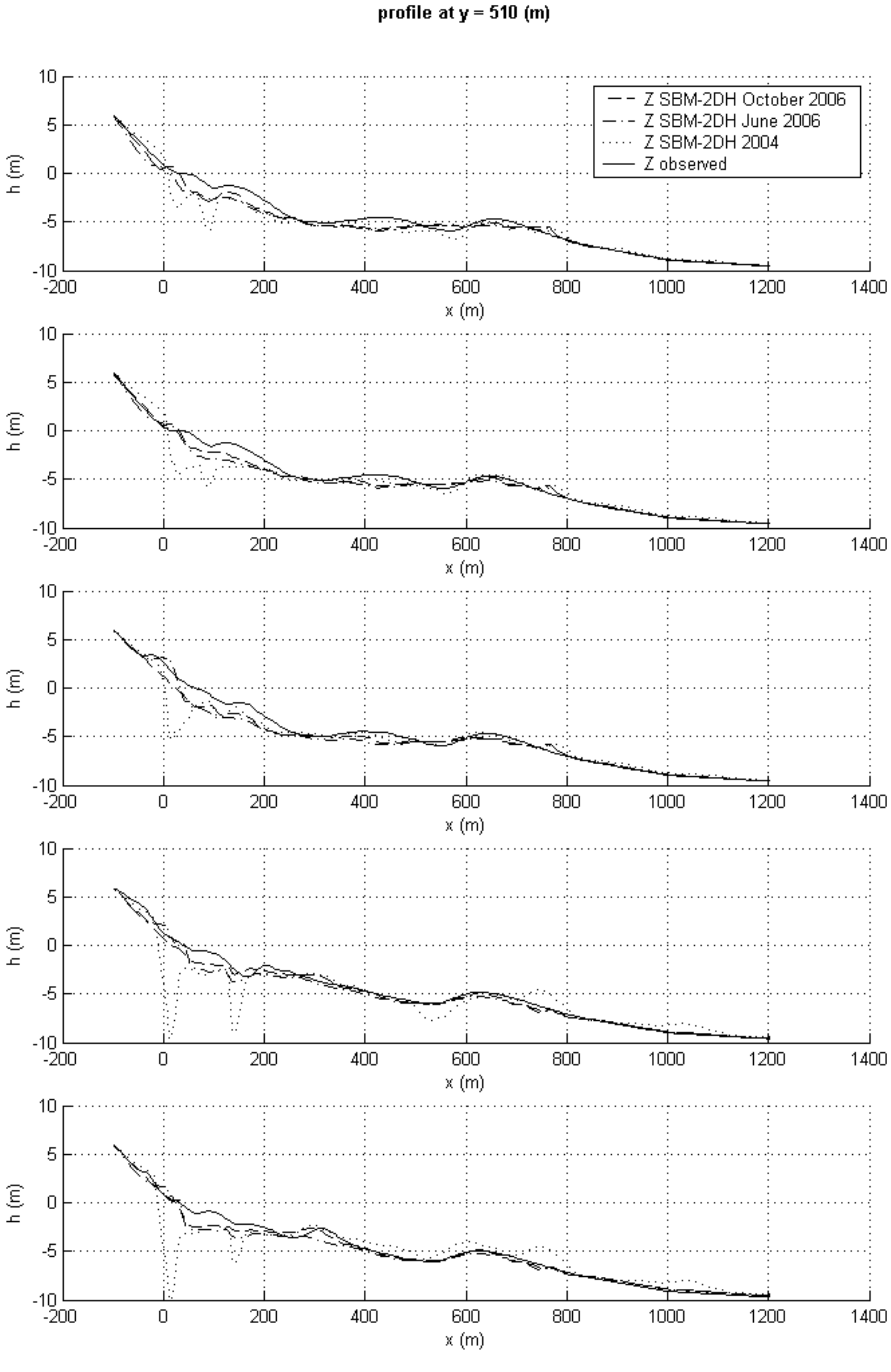

Figure 39: Results of the Egmond application at a cross-shore array (y = 510 m) at the five points in time during the model period when the bathymetry was measured (from top to bottom: 05/04/2000, 17/05/2000, 17/09/2000, 18/04/2001 and 18/06/2001). The thick black line indicates the measured bathymetry, the thin black line indicates the computed bathymetry. The dash-dotted lines indicate the initial situation of both.

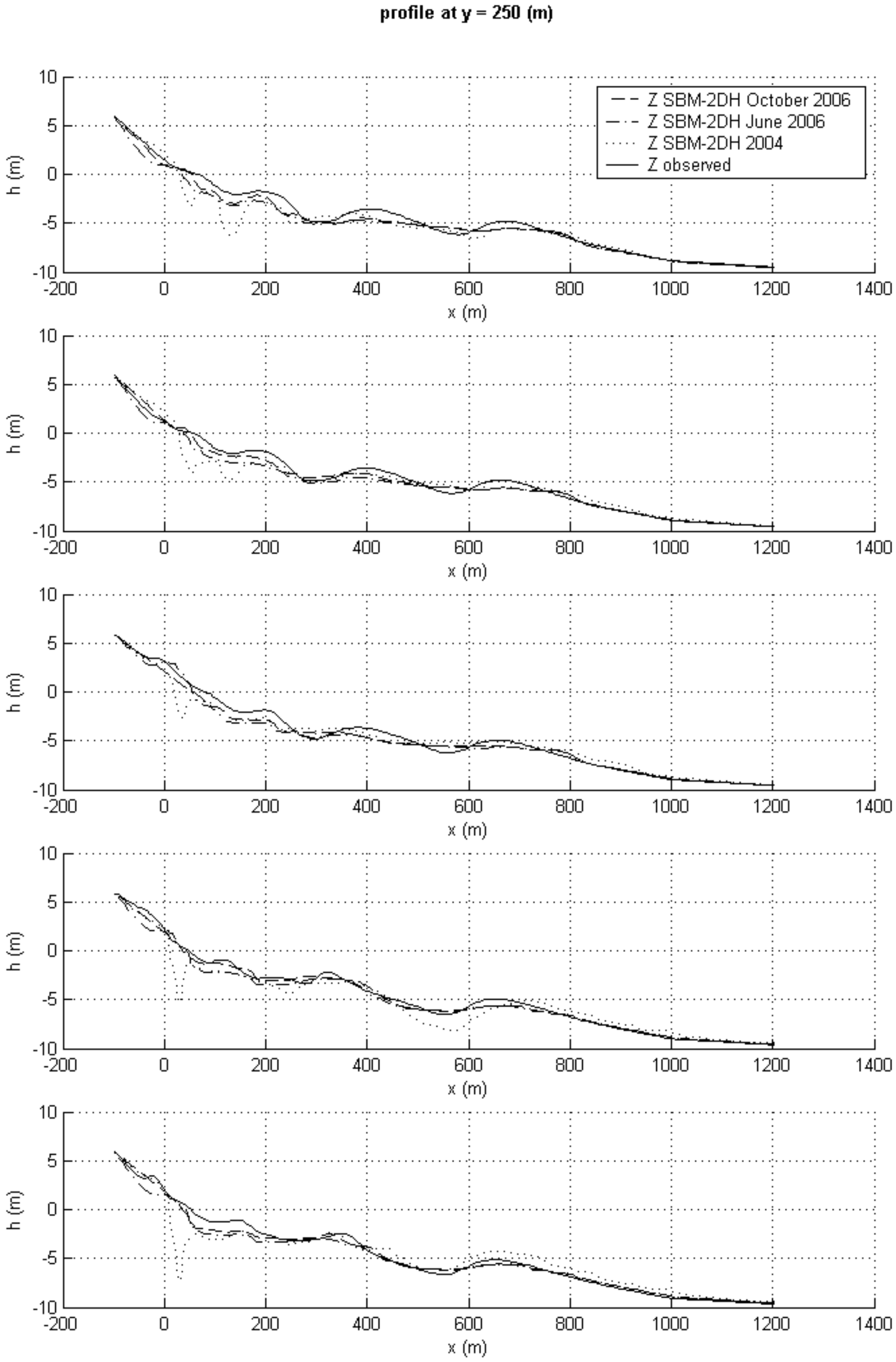

Figure 40: Results of the Egmond application at a cross-shore array (y = 250 m) at the five points in time during the model period when the bathymetry was measured (from top to bottom: 05/04/2000, 17/05/2000, 17/09/2000, 18/04/2001 and 18/06/2001). The thick black line indicates the measured bathymetry, the thin black line indicates the computed bathymetry. The dash-dotted lines indicate the initial situation of both.

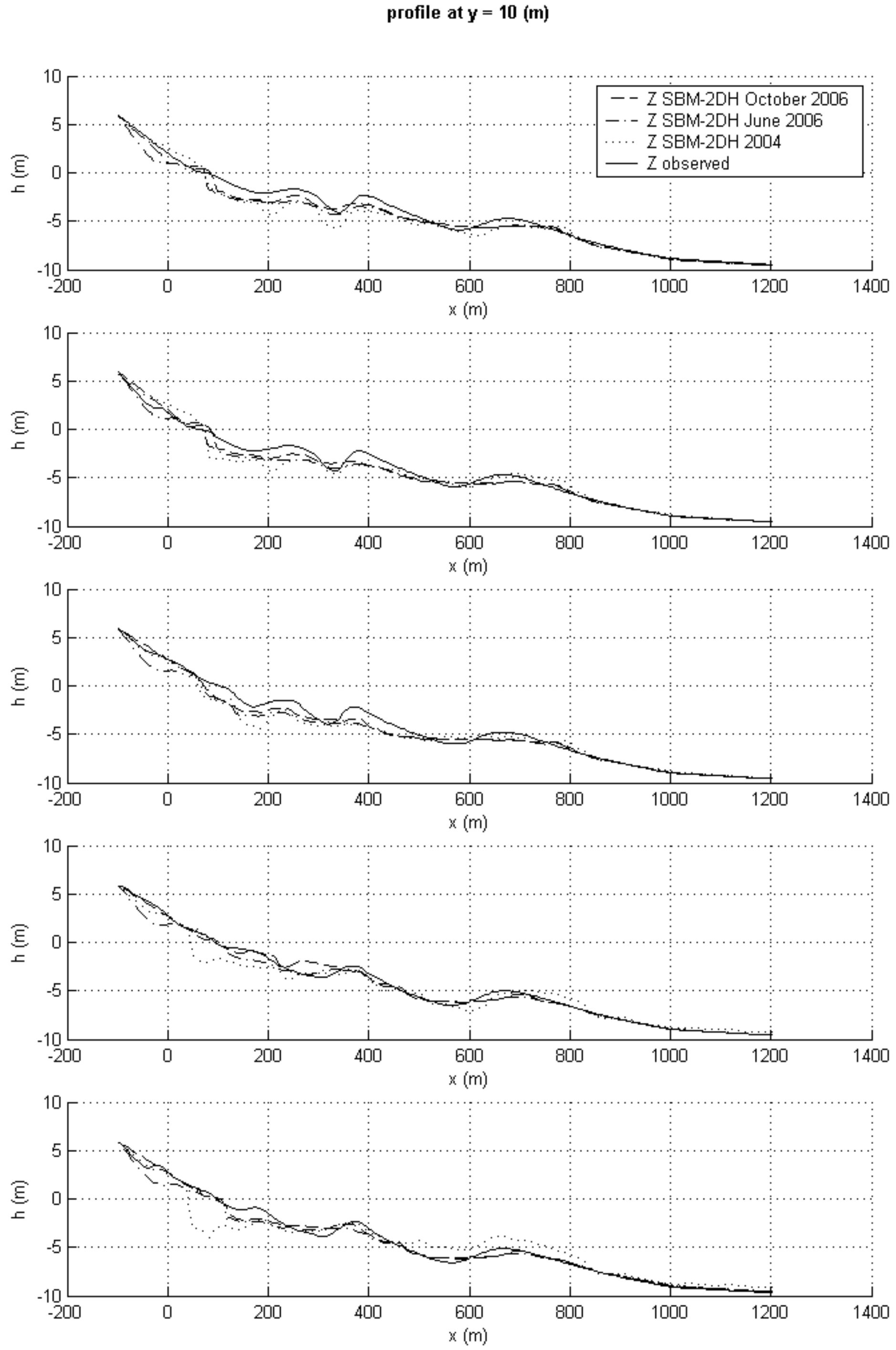

Figure 41: Results of the Egmond application at a cross-shore array (y = 10 m) at the five points in time during the model period when the bathymetry was measured (from top to bottom: 05/04/2000, 17/05/2000, 17/09/2000, 18/04/2001 and 18/06/2001). The thick black line indicates the measured bathymetry, the thin black line indicates the computed bathymetry. The dash-dotted lines indicate the initial situation of both.

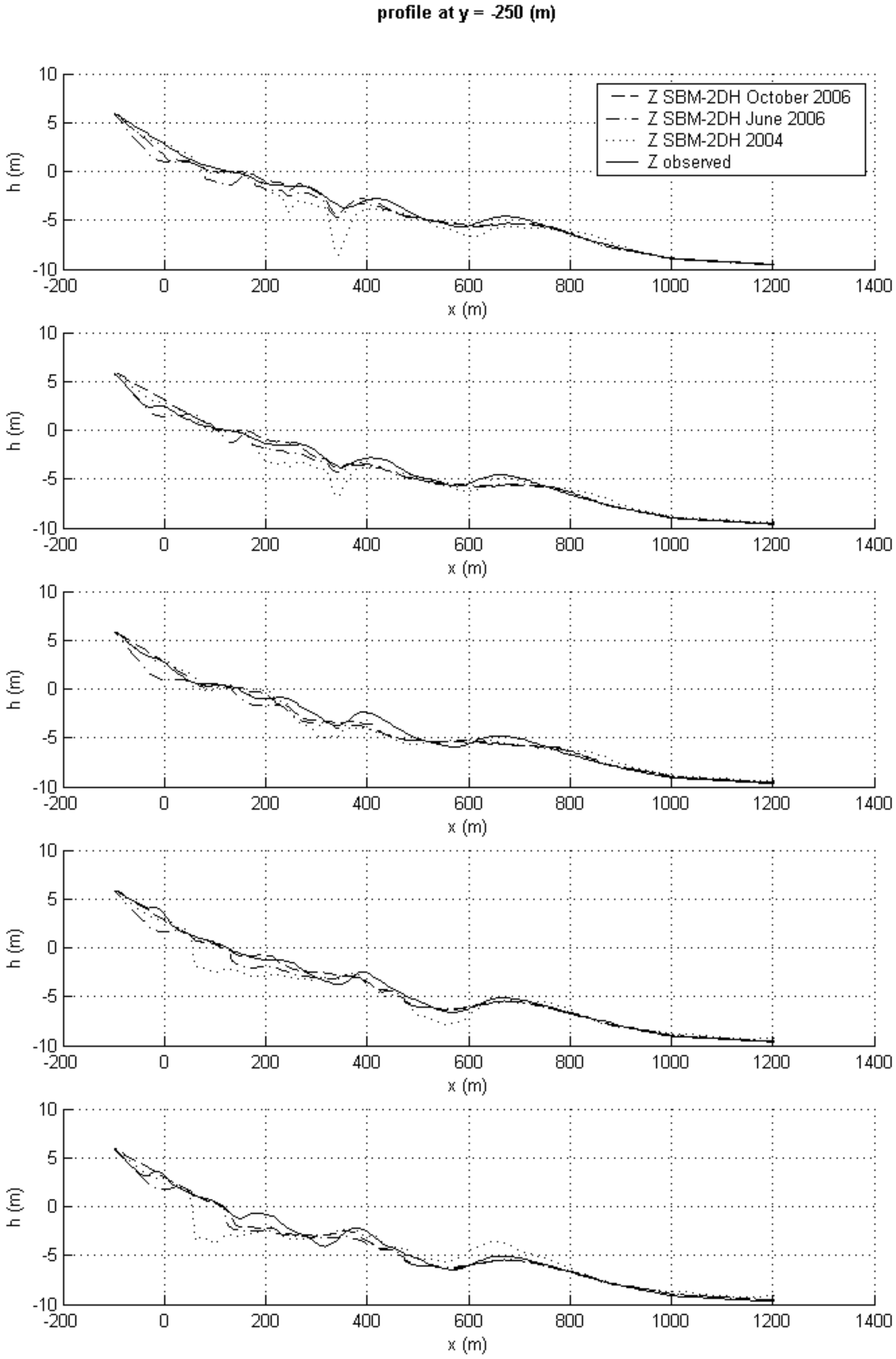

Figure 42: Results of the Egmond application at a cross-shore array (y = -250 m) at the five points in time during the model period when the bathymetry was measured (from top to bottom: 05/04/2000, 17/05/2000, 17/09/2000, 18/04/2001 and 18/06/2001). The thick black line indicates the measured bathymetry, the thin black line indicates the computed bathymetry. The dash-dotted lines indicate the initial situation of both.

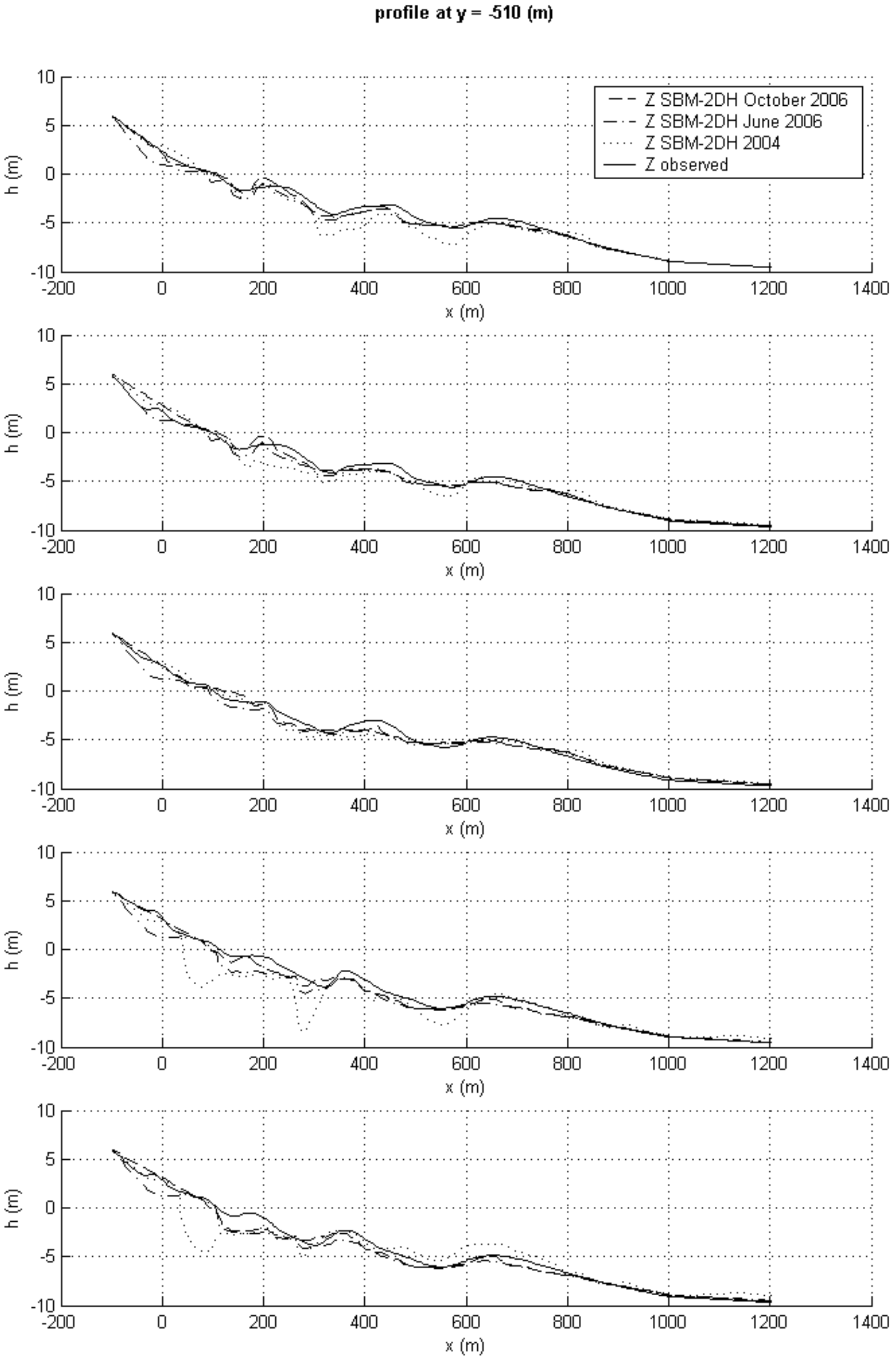

Figure 43: Results of the Egmond application at a cross-shore array (y = -510 m) at the five points in time during the model period when the bathymetry was measured (from top to bottom: 05/04/2000, 17/05/2000, 17/09/2000, 18/04/2001 and 18/06/2001). The thick black line indicates the measured bathymetry, the thin black line indicates the computed bathymetry. The dash-dotted lines indicate the initial situation of both.

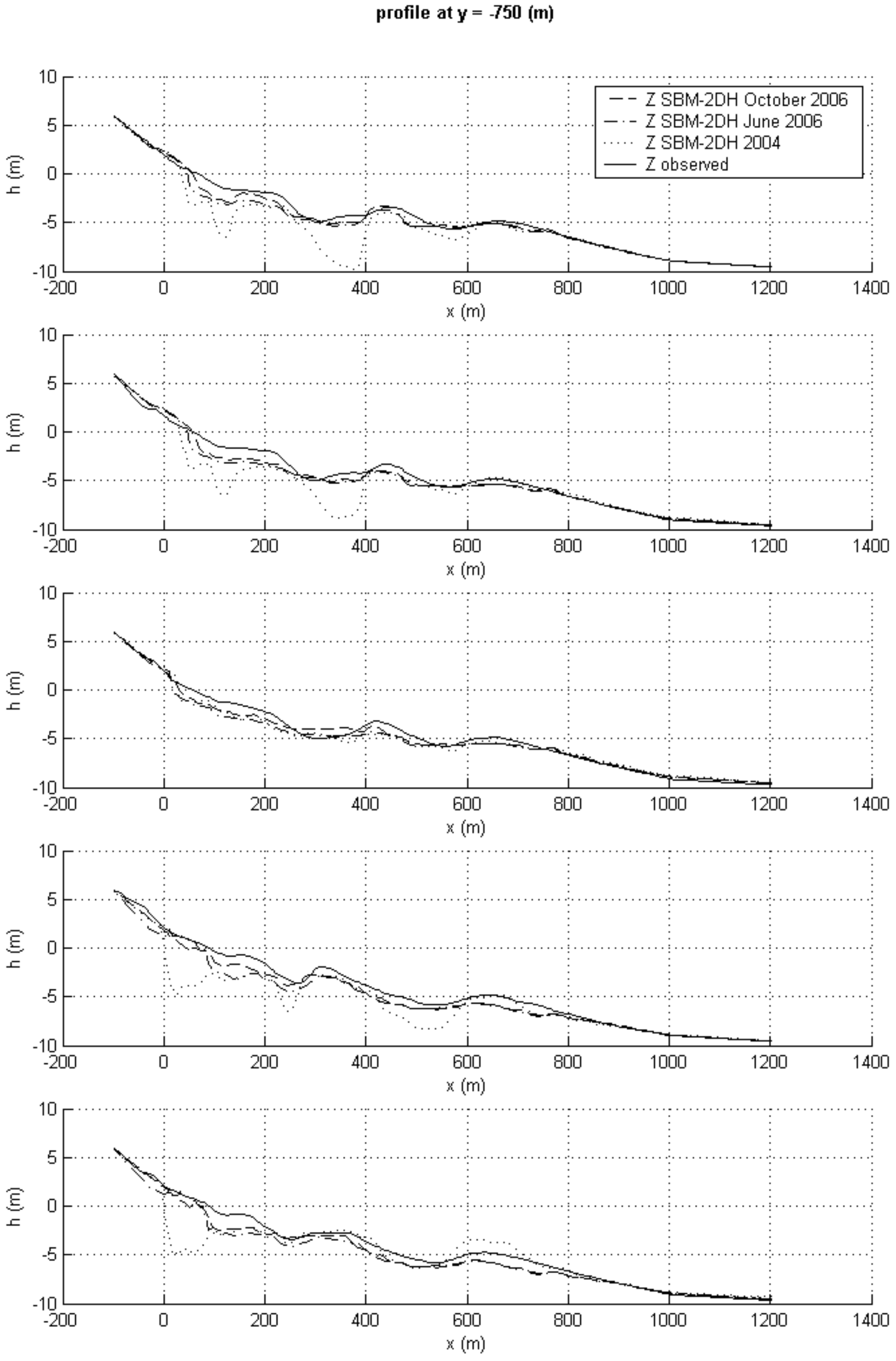

Figure 44: Results of the Egmond application at a cross-shore array (y = -750 m) at the five points in time during the model period when the bathymetry was measured (from top to bottom: 05/04/2000, 17/05/2000, 17/09/2000, 18/04/2001 and 18/06/2001). The thick black line indicates the measured bathymetry, the thin black line indicates the computed bathymetry. The dash-dotted lines indicate the initial situation of both.

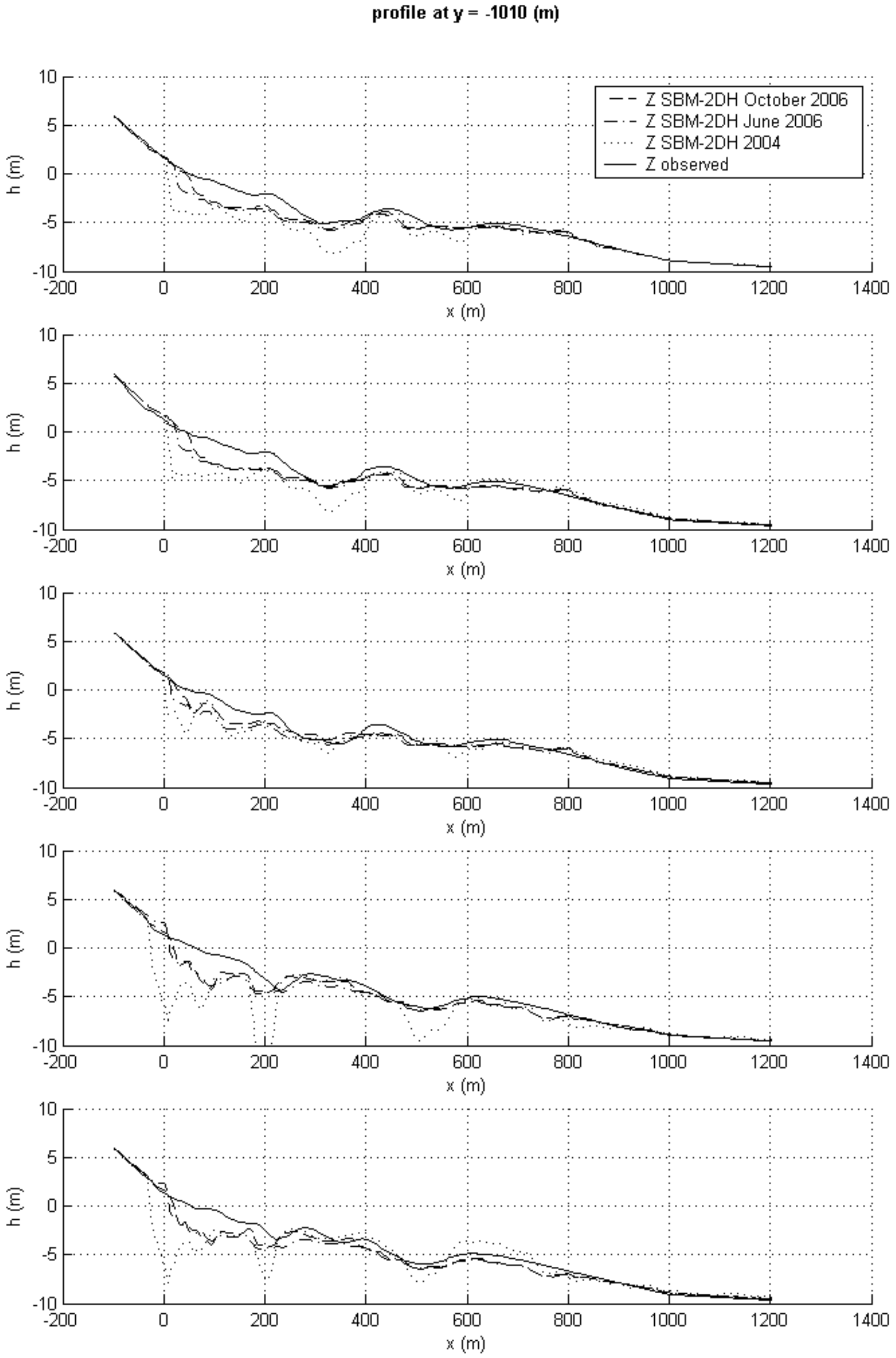

Figure 45: Results of the Egmond application at a cross-shore array (y = -1010 m) at the five points in time during the model period when the bathymetry was measured (from top to bottom: 05/04/2000, 17/05/2000, 17/09/2000, 18/04/2001 and 18/06/2001). The thick black line indicates the measured bathymetry, the thin black line indicates the computed bathymetry. The dash-dotted lines indicate the initial situation of both.

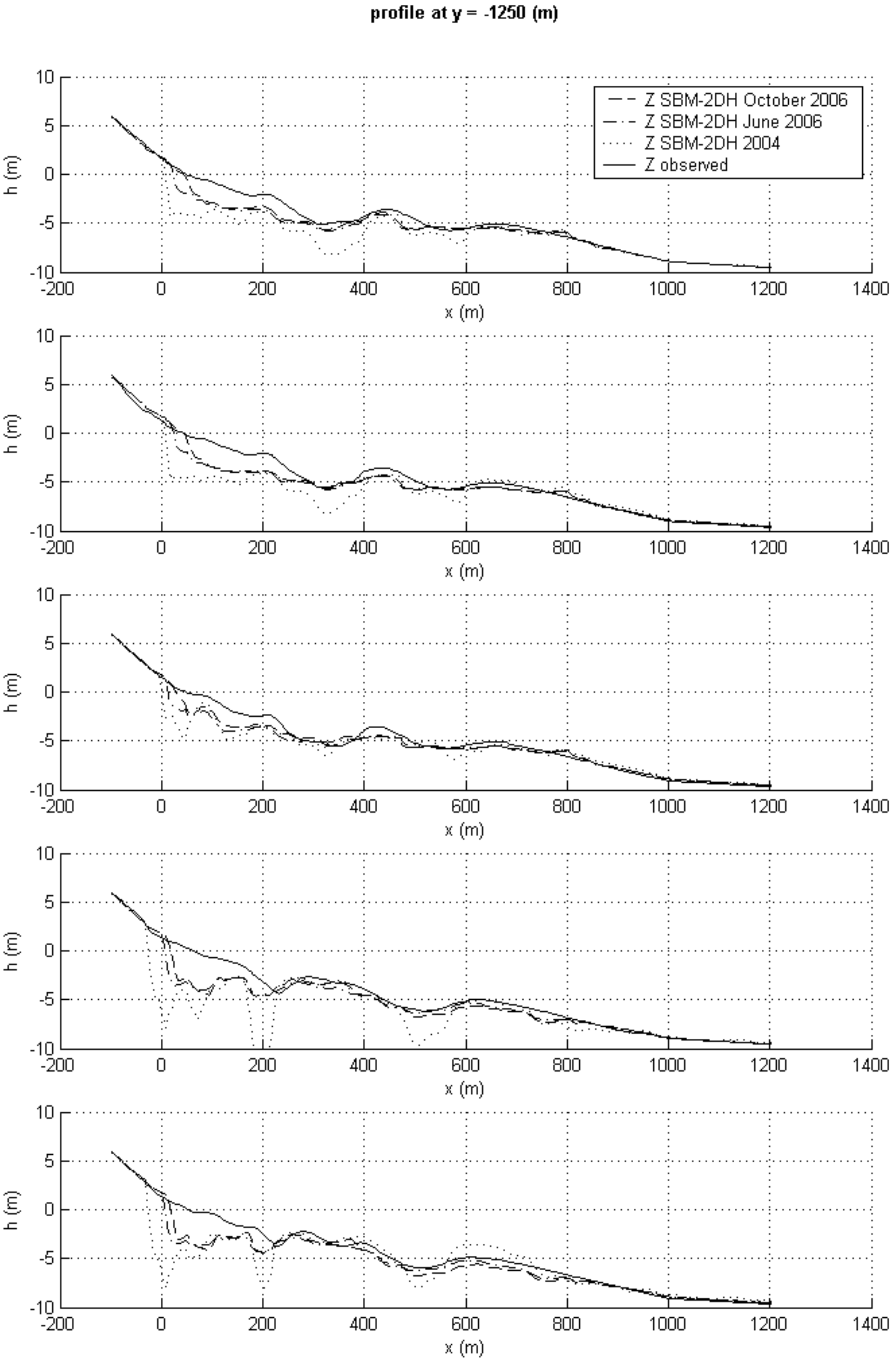

Figure 46: Results of the Egmond application at a cross-shore array (y = -1250 m) at the five points in time during the model period when the bathymetry was measured (from top to bottom: 05/04/2000, 17/05/2000, 17/09/2000, 18/04/2001 and 18/06/2001). The thick black line indicates the measured bathymetry, the thin black line indicates the computed bathymetry. The dash-dotted lines indicate the initial situation of both.

D Momentary Coast Line

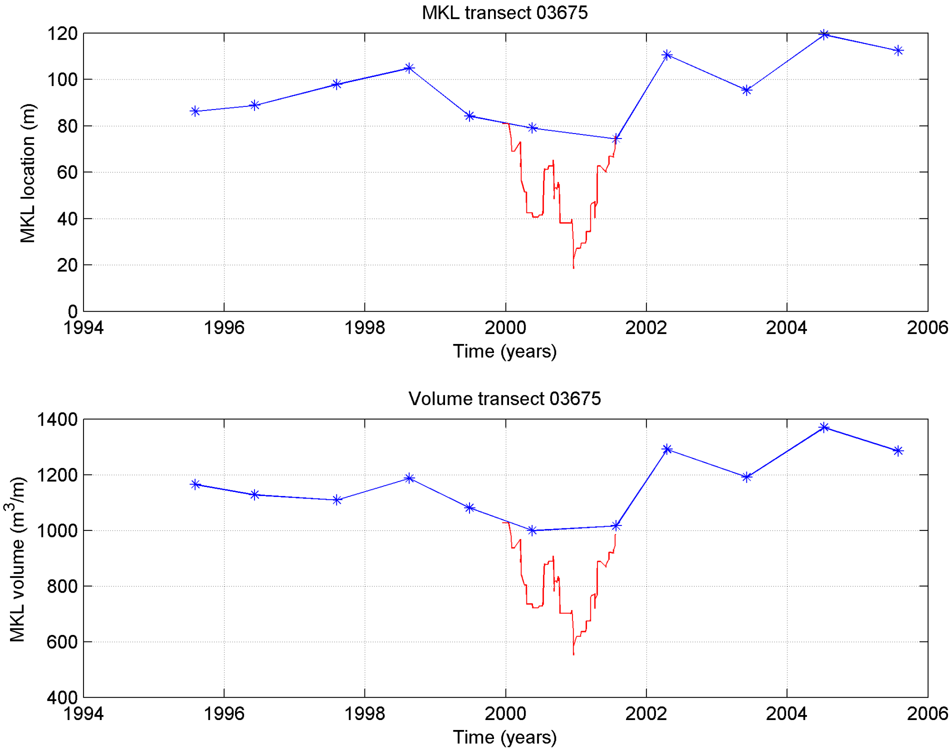

Figure 47: MCL position and volume at JARKUS transect 3675 from JARKUS data (blue) and model (red). This corresponds to y=-1250 m in the ARGUS coordinates.

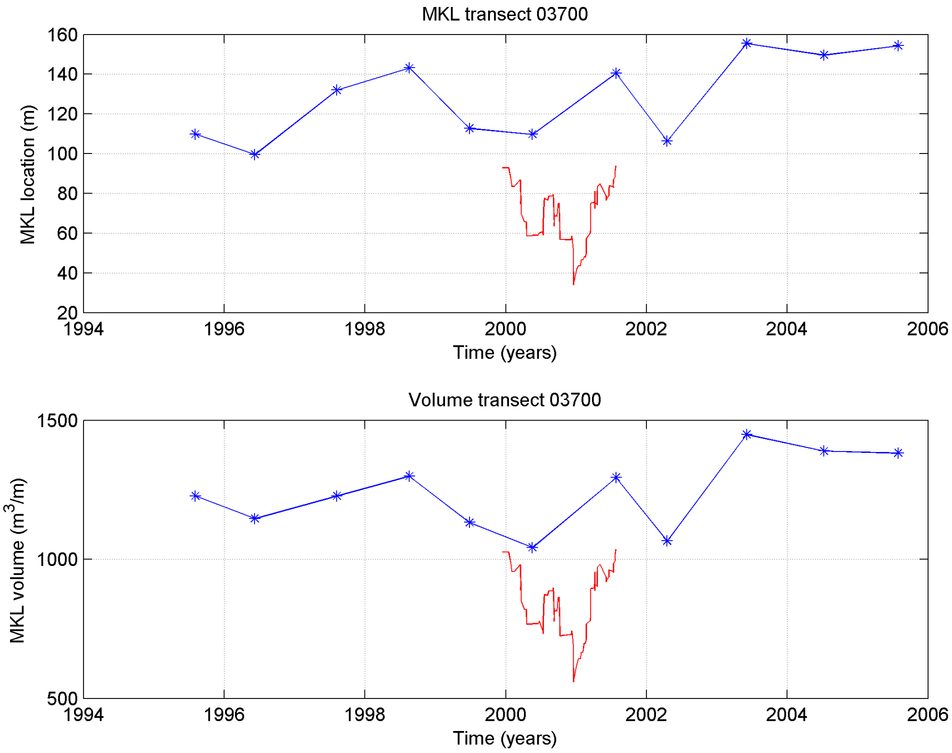

Figure 48: MCL position and volume at JARKUS transect 3700 from JARKUS data (blue) and model (red). This corresponds to y=-1000 m in the ARGUS coordinates.

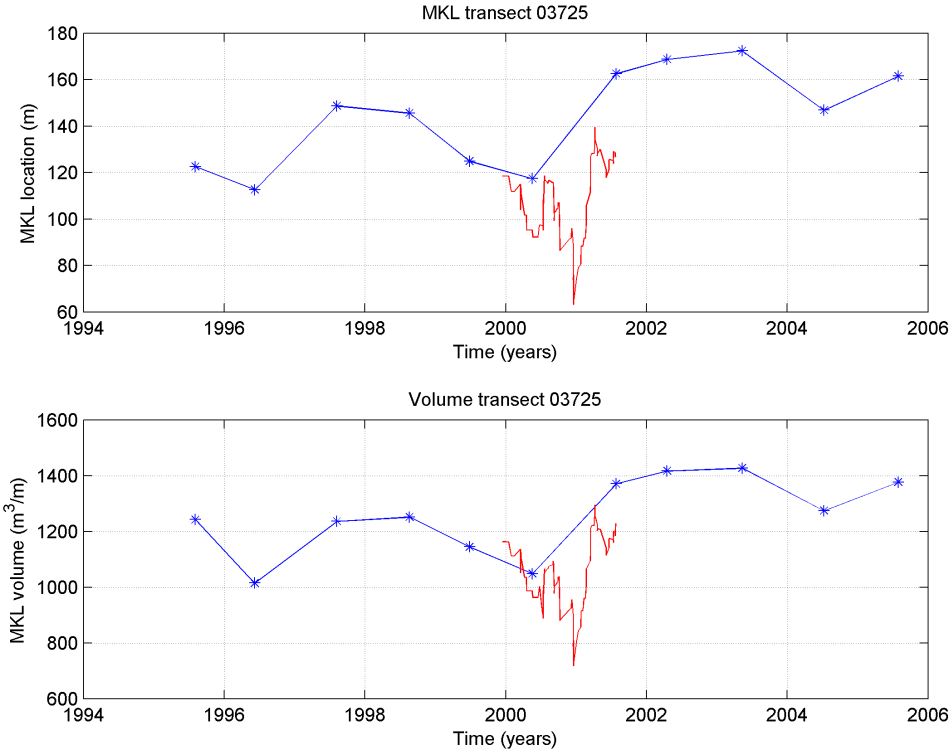

Figure 49: MCL position and volume at JARKUS transect 3725 from JARKUS data (blue) and model (red). This corresponds to y=-750 m in the ARGUS coordinates.

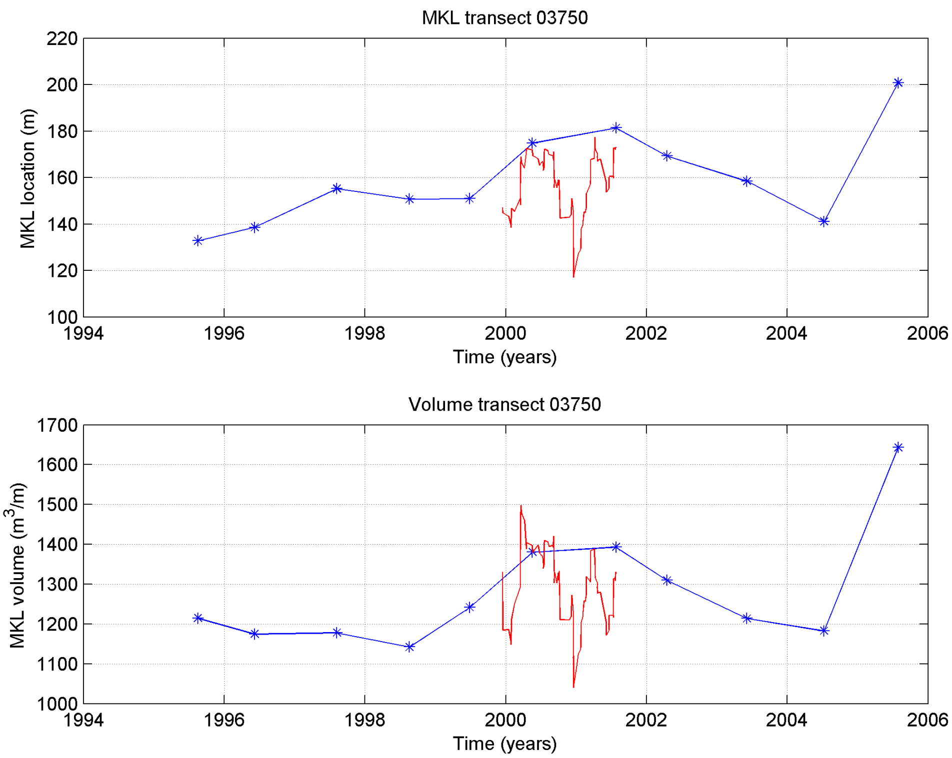

Figure 50: MCL position and volume at JARKUS transect 3750 from JARKUS data (blue) and model (red). This corresponds to y=-500 m in the ARGUS coordinates.

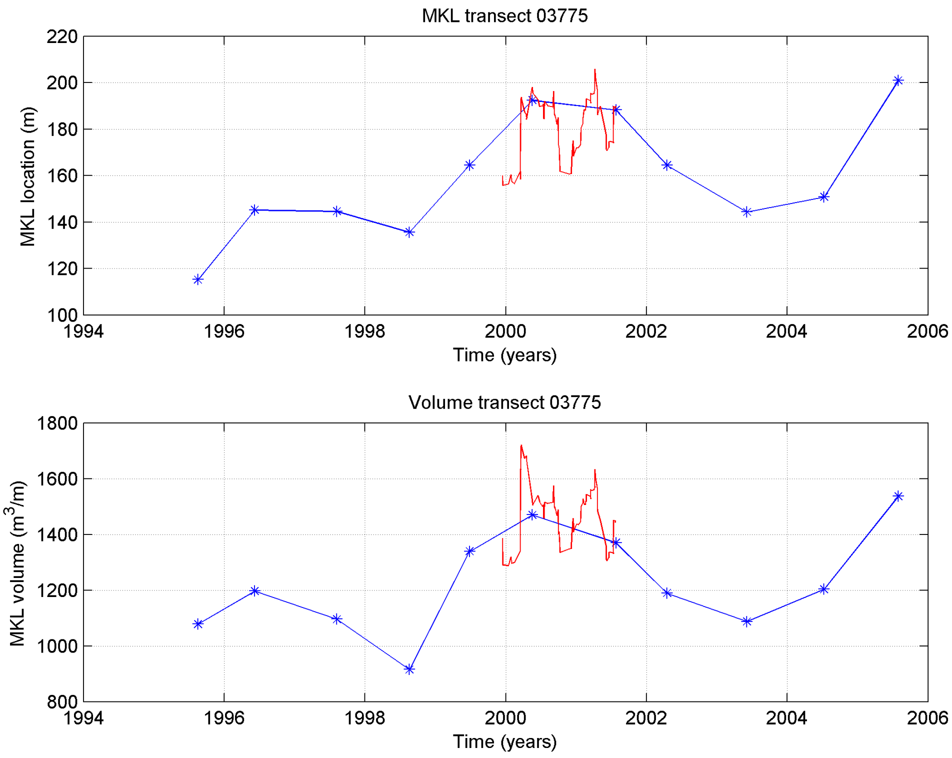

Figure 51: MCL position and volume at JARKUS transect 3775 from JARKUS data (blue) and model (red). This corresponds to y=-250 m in the ARGUS coordinates.

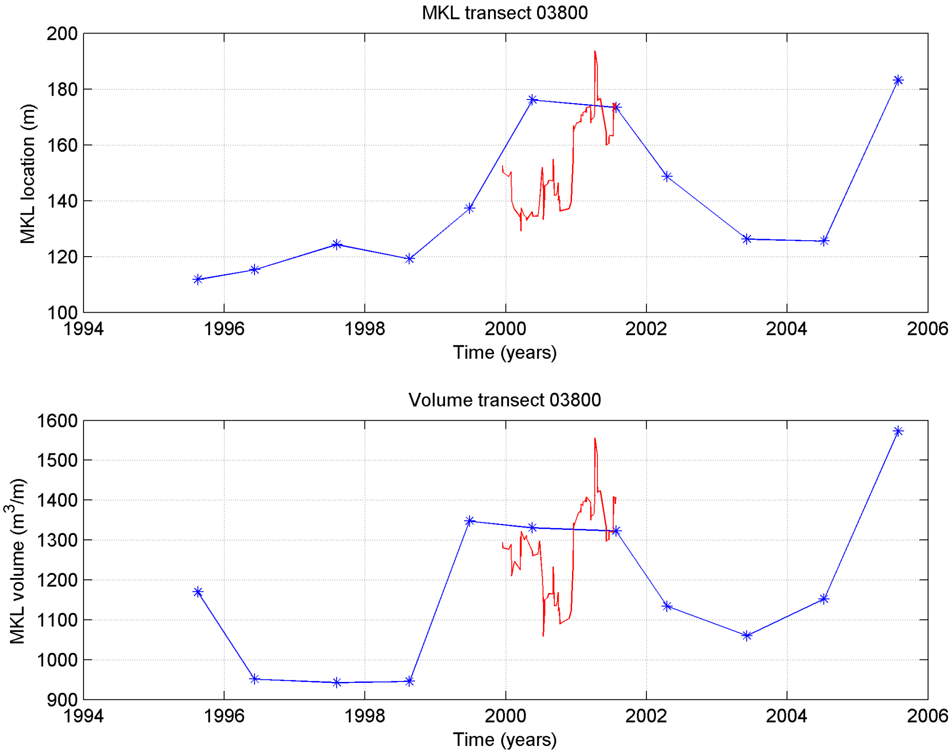

Figure 52: MCL position and volume at JARKUS transect 3800 from JARKUS data (blue) and model (red). This corresponds to y= 10 m in the ARGUS coordinates.

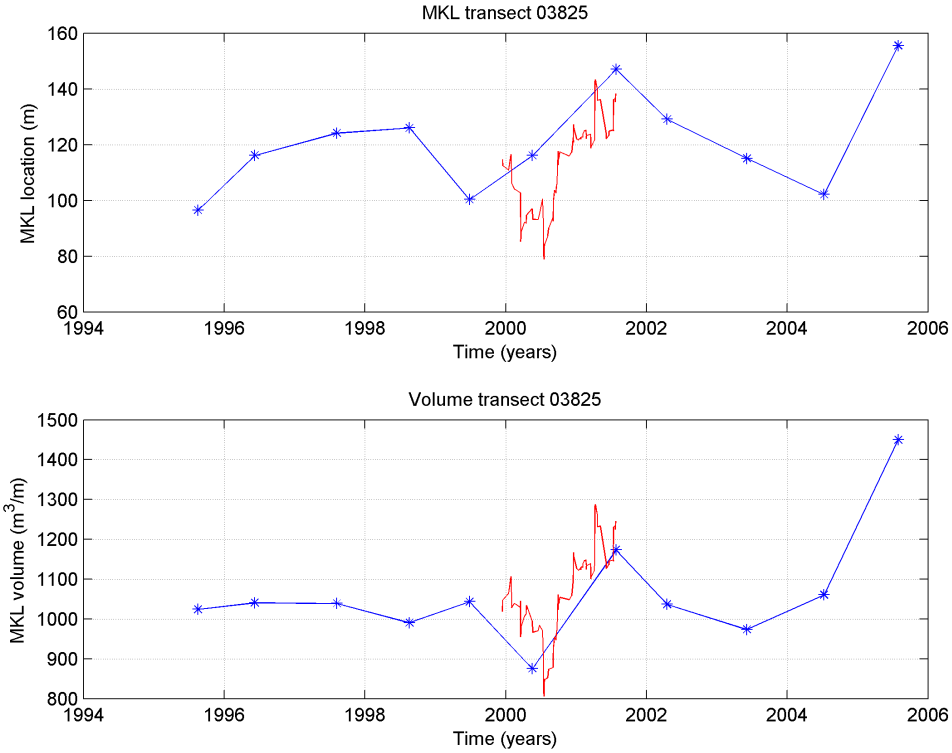

Figure 53: MCL position and volume at JARKUS transect 3825 from JARKUS data (blue) and model (red). This corresponds to y= 250 m in the ARGUS coordinates.

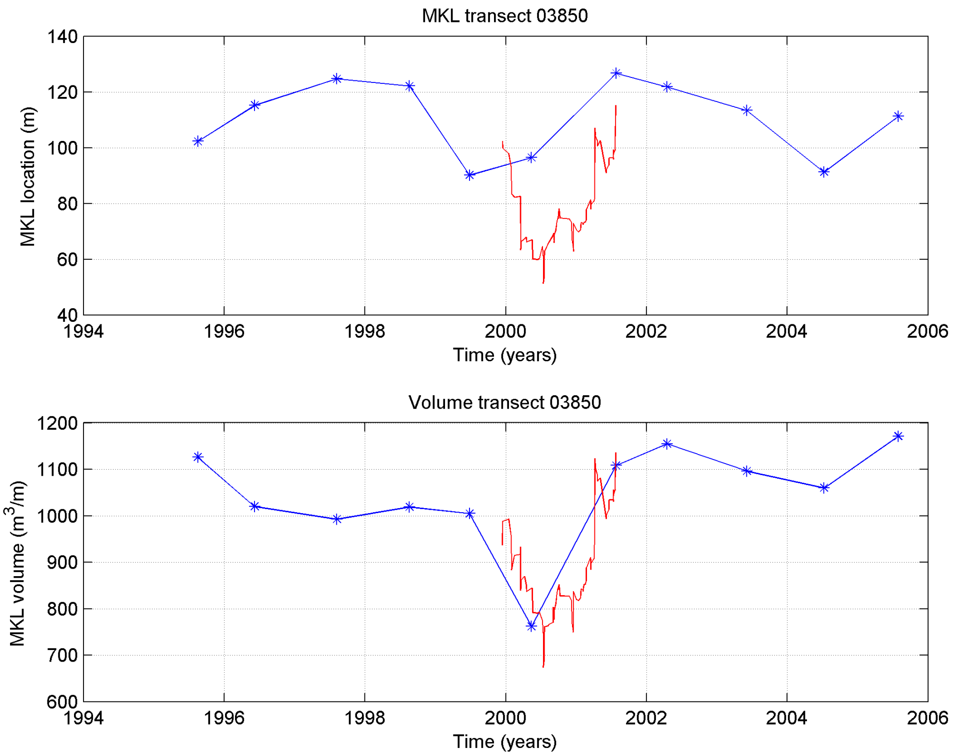

Figure 54: MCL position and volume at JARKUS transect 3850 from JARKUS data (blue) and model (red). This corresponds to y= 500 m in the ARGUS coordinates.

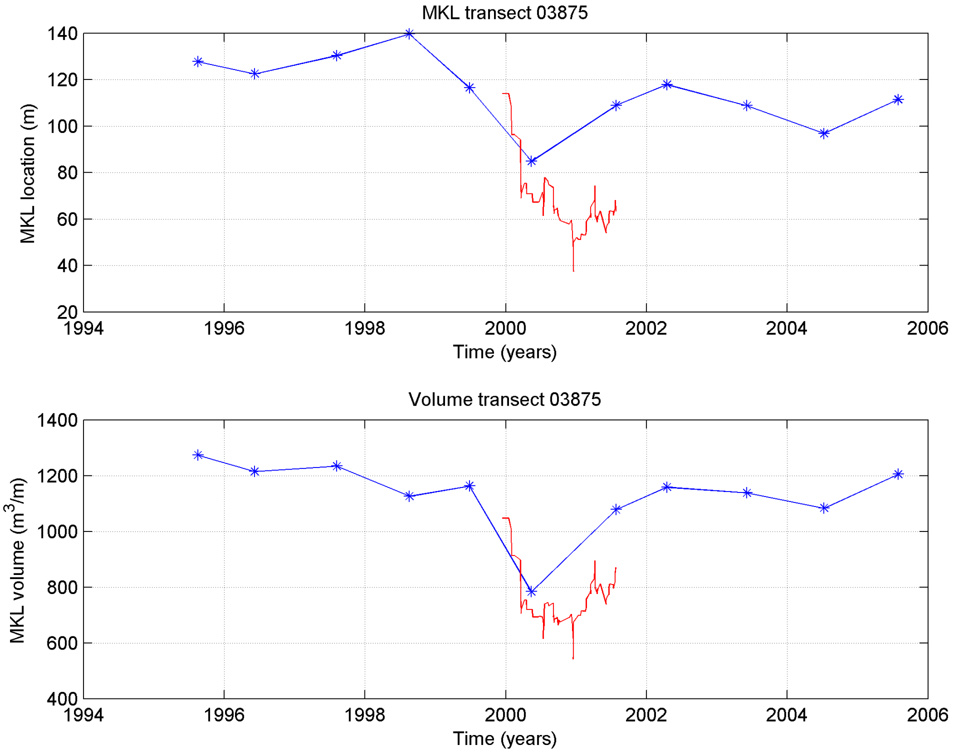

Figure 55: MCL position and volume at JARKUS transect 3875 from JARKUS data (blue) and model (red). This corresponds to y= 750 m in the ARGUS coordinates.

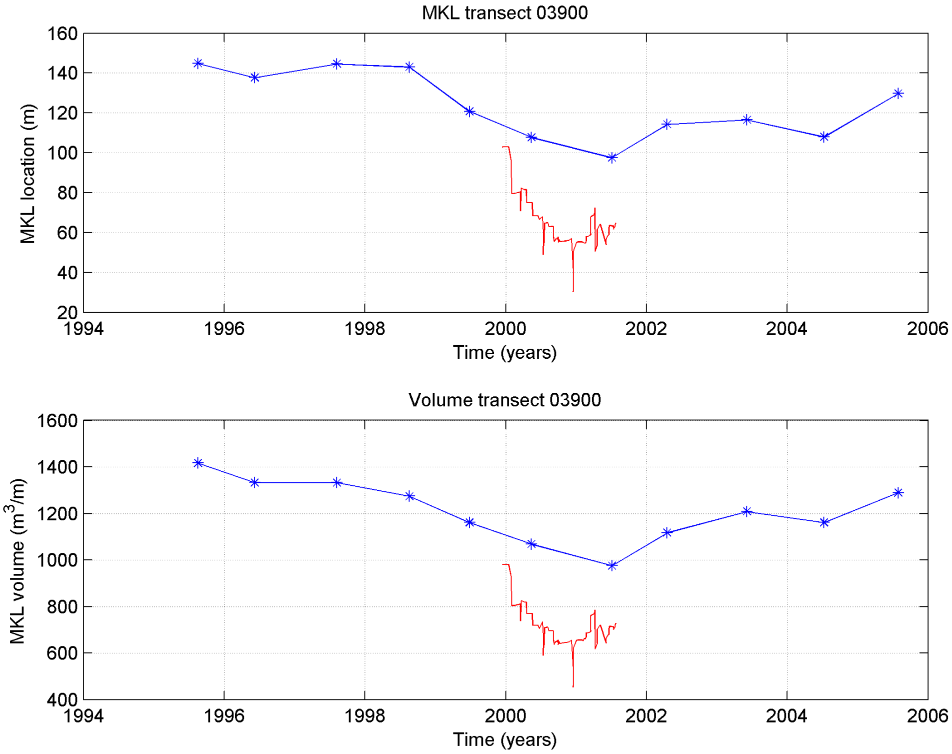

Figure 56: MCL position and volume at JARKUS transect 3900 from JARKUS data (blue) and model (red). This corresponds to y= 1000 m in the ARGUS coordinates.

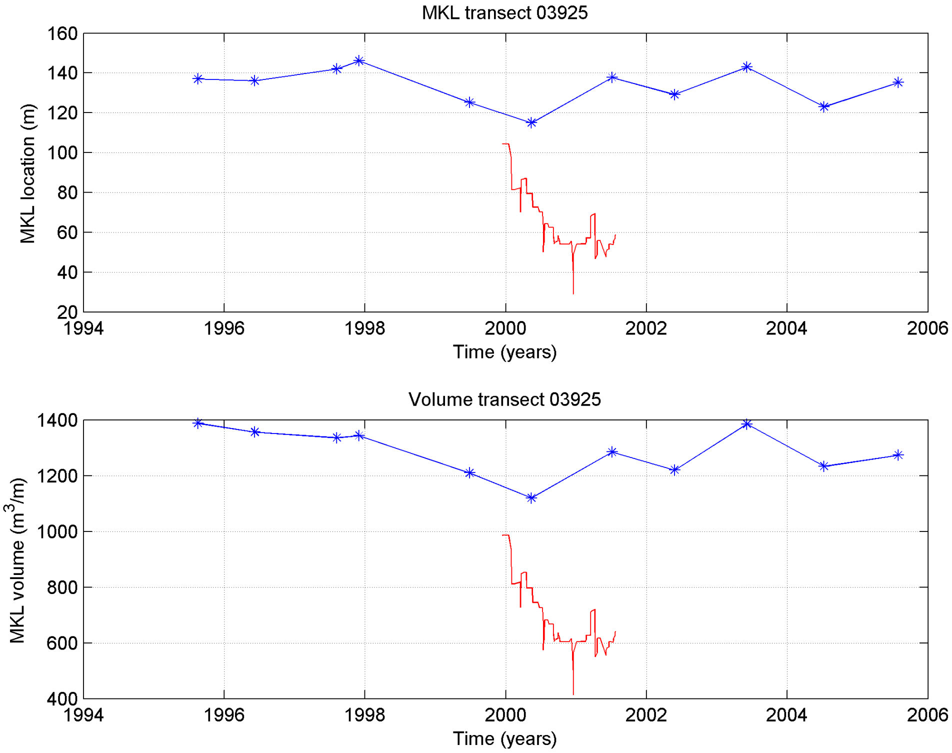

Figure 57: MCL position and volume at JARKUS transect 3925 from JARKUS data (blue) and model (red). This corresponds to y= 1250 m in the ARGUS coordinates.

E Bar position and height

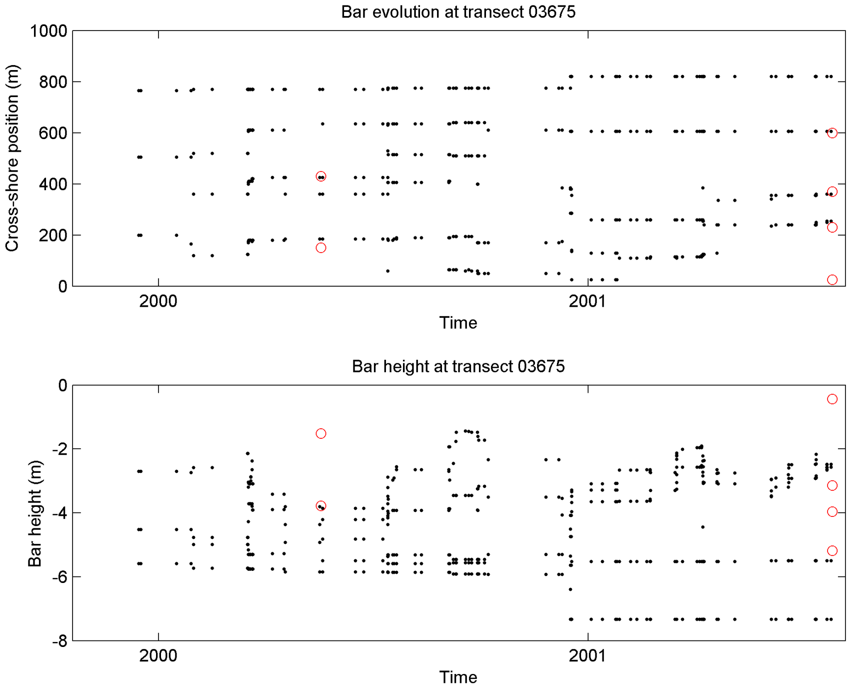

Figure 58: Caption as in Figure 22

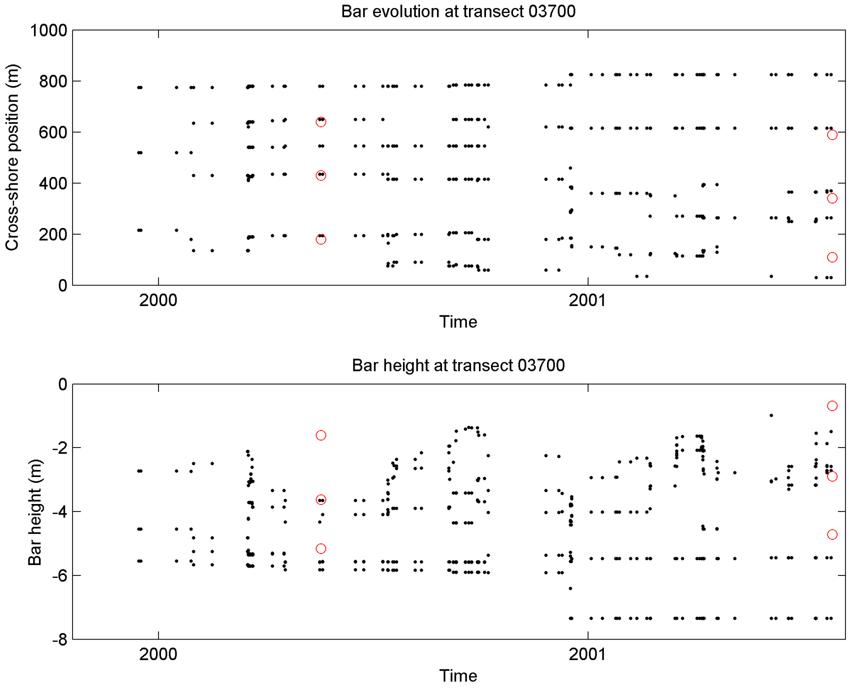

Figure 59: Caption as in Figure 22

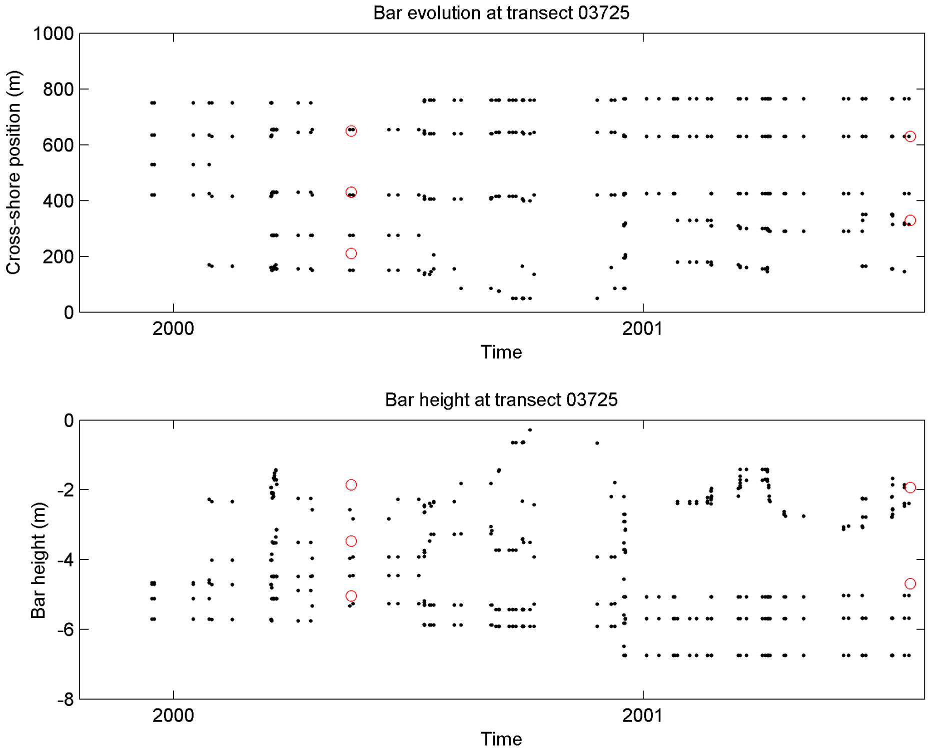

Figure 60: Caption as in Figure 22

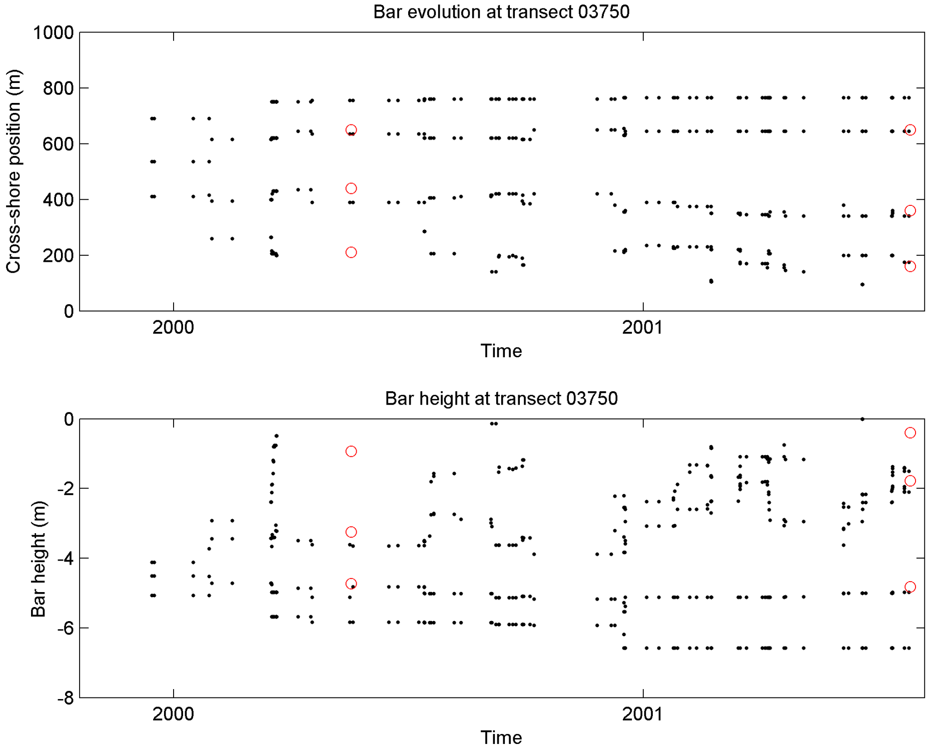

Figure 61: Caption as in Figure 22

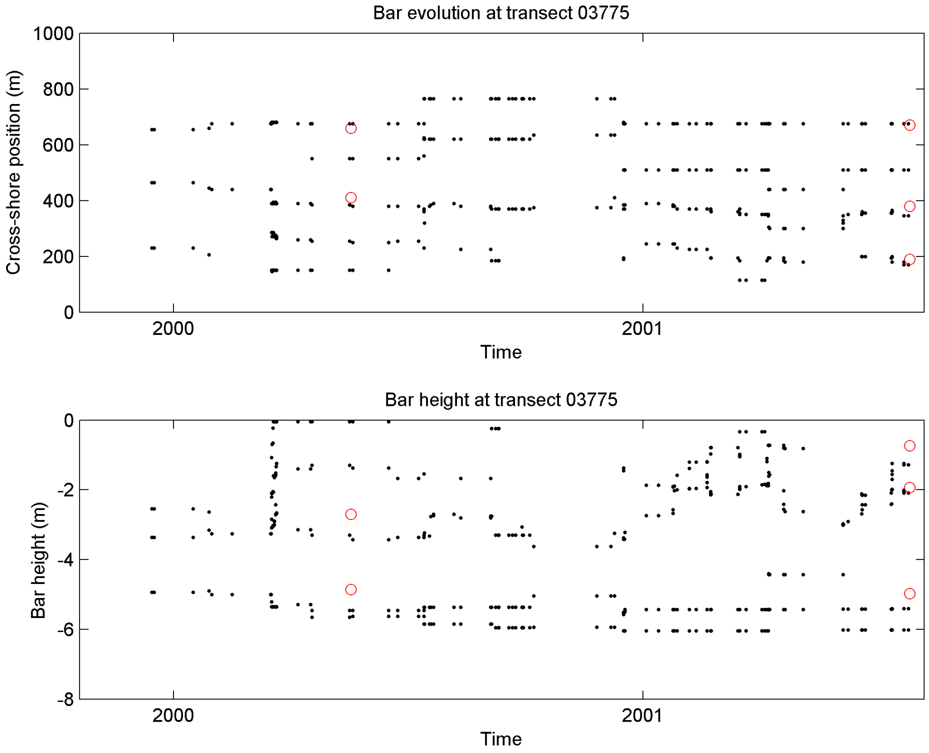

Figure 62: Caption as in Figure 22

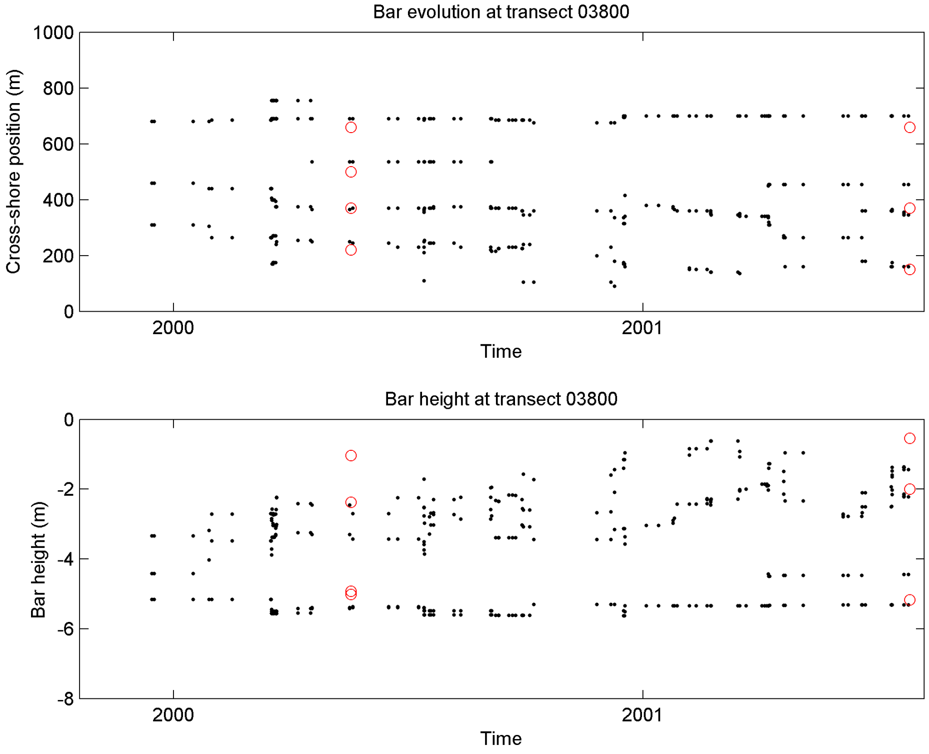

Figure 63: Caption as in Figure 22

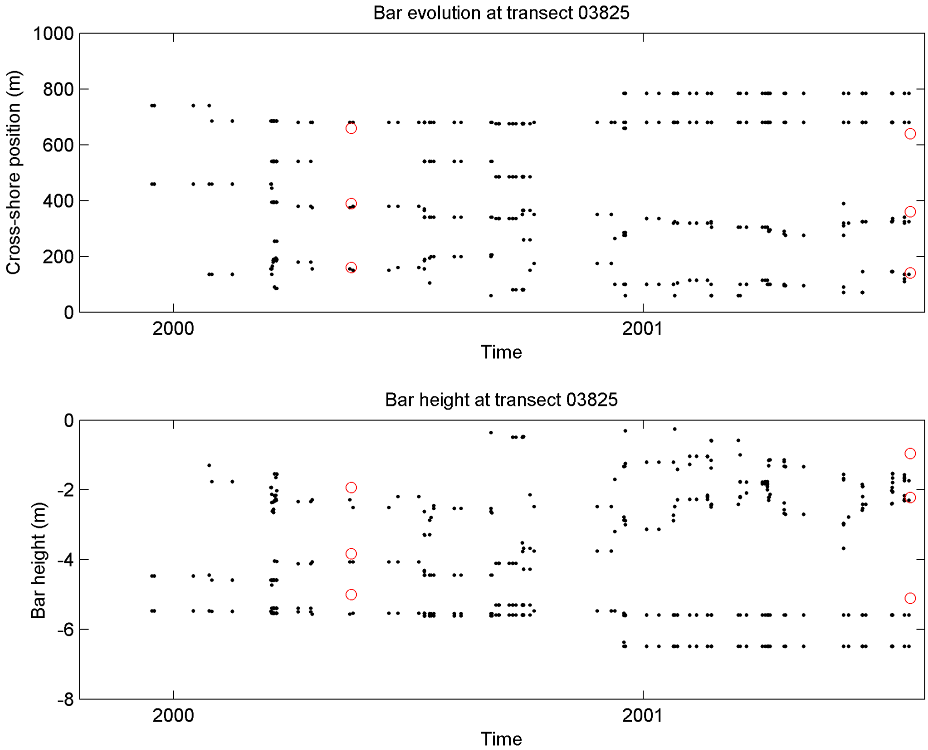

Figure 64: Caption as in Figure 22

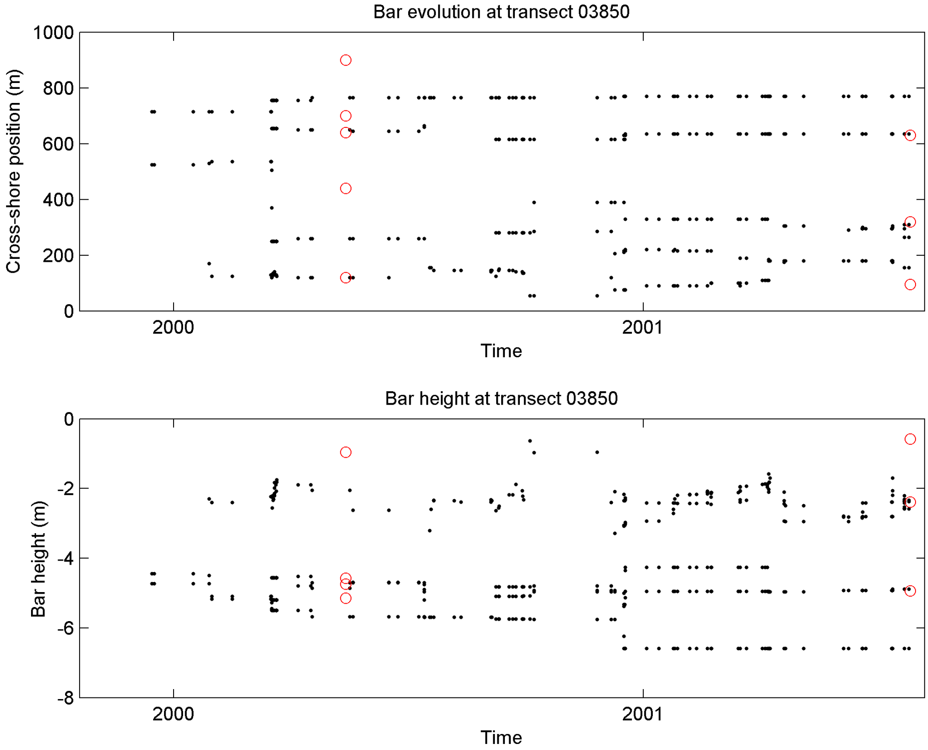

Figure 65: Caption as in Figure 22

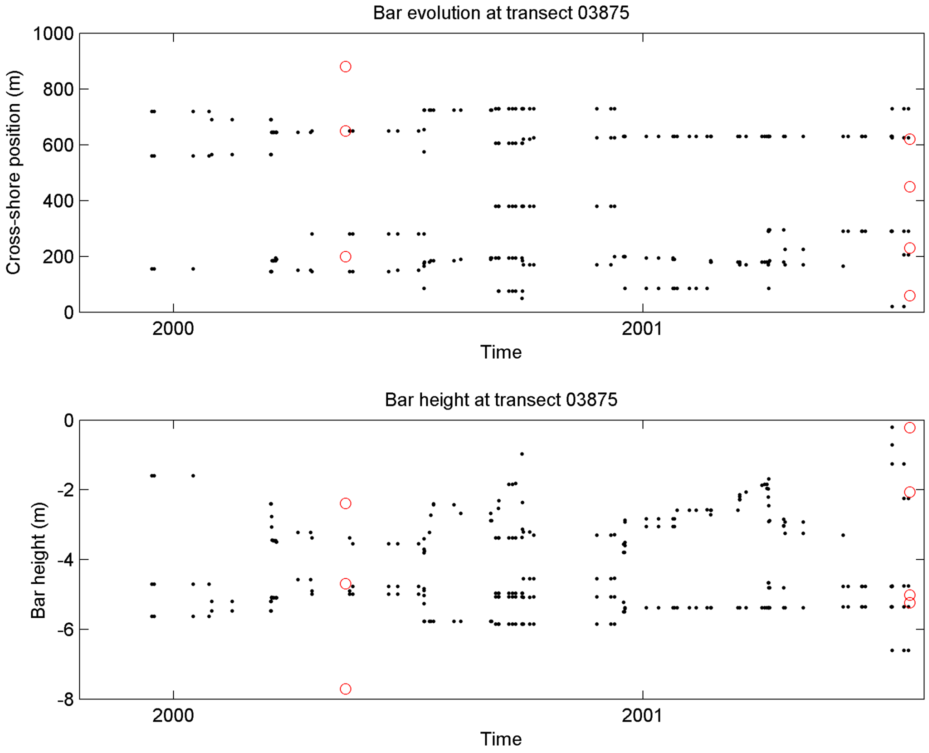

Figure 66: Caption as in Figure 22

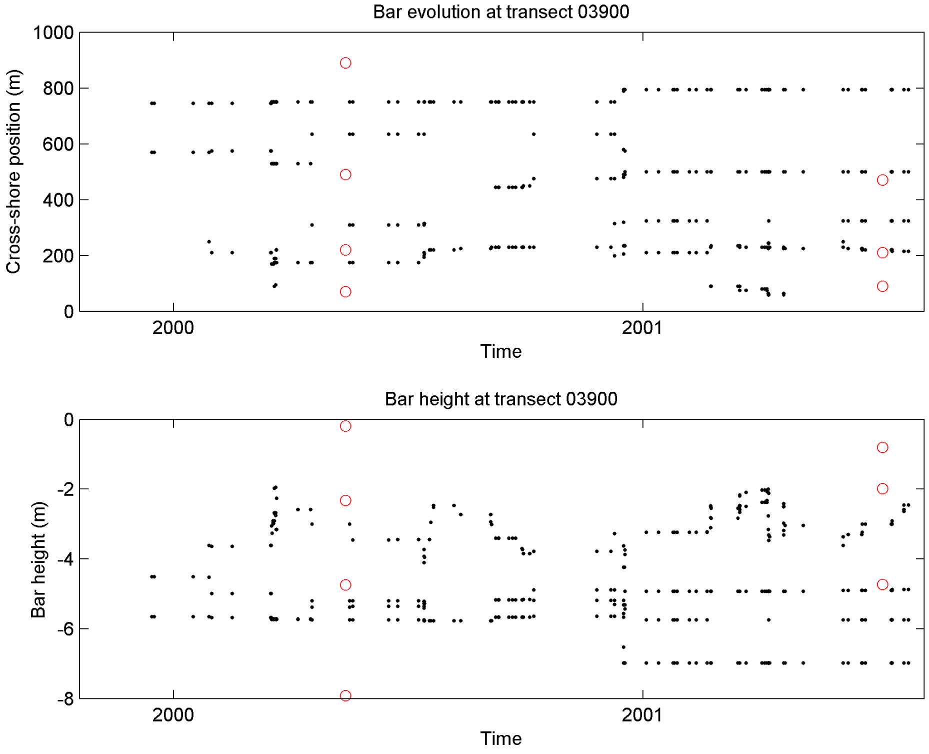

Figure 67: Caption as in Figure 22

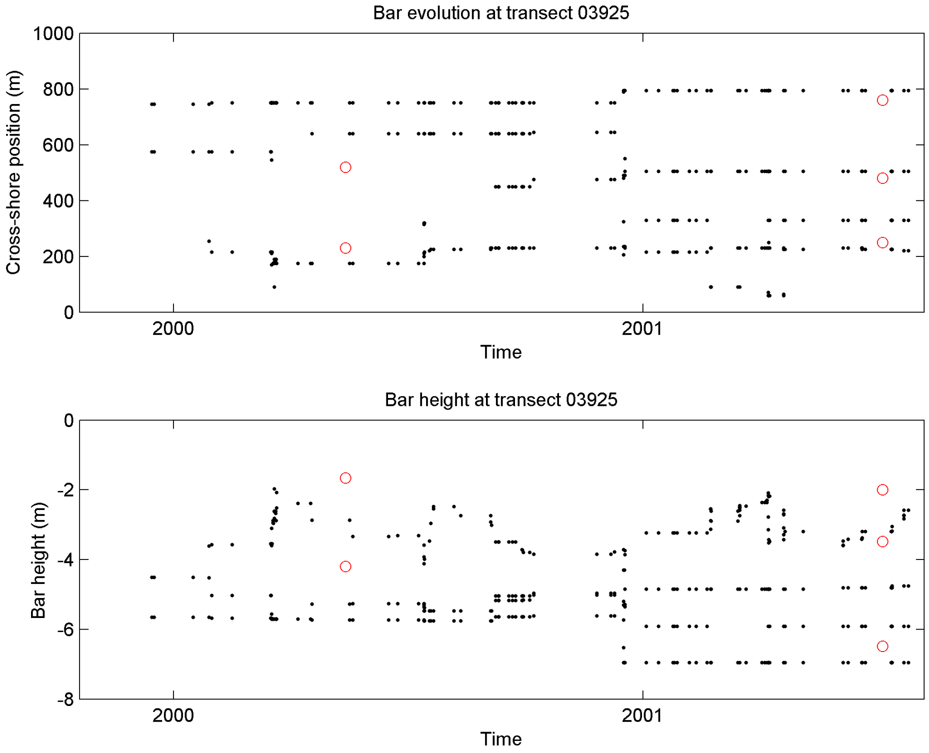

Figure 68: Caption as in Figure 22

References

Aarninkhof, S.G.J. and Holman, R.A. (1999). Monitoring the nearshore with video. Backscatter, 10(2), pp. 8-11

Aarninkhof, S.G.J., Turner, I.L., Dronkers, T.D.T., Caljouw, M. and Nipius, L. (2003).A video-technique for mapping intertidal beach bathymetry. Coastal Engineering49, pp. 275-289.

Aarninkhof, S.G.J., Ruessink, B.G. and Roelvink, J.A. (2005a). Nearshore subtidal bathymetry from time-exposure video images. Jnl. of Geophysical Research, Vol. 110, C06011, doi: 10.1029/2004JC002791.

Aarninkhof, S.G.A., K.M. Wijnberg, J.A. Roelvink and A.J.H.M. Reniers (2005b), 2DH-Quantication of surf zone bathymetry from video, Proc. Coastal Dynamics ’05.

Alport, M., J. Basson, G. P. Mocke, J. Naicker & C. Saltau (2001), Discrimination and analysis of video imaged shorelines and nearshore processes. In: Proc. of Coastal Dynamics Conf., Lund, Sweden, ASCE, pp. 989–997.

Arcilla, A.S., Roelvink, J.A., O’Connor, B.A., Reniers, A.J.H.M. and Jimenez, J.A. (1994). The Delta flume ’93 experiment. ASCE, Proc. Coastal Dynamics 1994, Barcelona, Spain, 488 – 502.

Baldock, T.E., P. Holmes, S. Bunker, and P.V. Weert (1998). Cross-shore hydrodynamics within an unsaturated surf zone, Coastal Engineering, 34, 173-196.

Bell, P. S. (1999), Shallow water bathymetry derived from an analysis of X-band marine radar images of waves. Coastal Engineering 37, pp. 513–527.

Boers, M. (1996). Simulation of a surf zone with a barred beach. Report 1: wave heights and wave breaking. Communications on hydraulic and geotechnical engineering. ISSN 0169-6548.

Booij, N., Ris, R.C., and Holthuijsen, L.H. (1999). “A third-generation wave model for coastal regions. 1. Model description and validation.” J. Geophys. Res., 104(C4), 7649-7666.

Bos. C. (2006). Wave characteristics derived from video. WL|Delft Hydraulics report Z3757.00

Caljouw, M., 2000. Video-based monitoring of the Egmond beach and shoreface nourishment. Rijkswaterstaat, RIKZ, Z2773.

Chickadel, C.C., Holman, R.A. and Freilich, M.H. (2003). An optical technique for the measurement of alongshore currents. Journal of Geophysical Research, 108(C11), 3364.

Cohen, A. B., A.R. Van Dongeren, J.A. Roelvink, N.G. Plant, S.G.A. Aarninkhof, M.C. Haller and P. Catalan, 2006, Nowcasting of coastal processes through assimilation of model computations and remote observations. Proc. ICCE 2006, in press.

Dugan, J. P., C. C. Piotrowski & J. Z. Williams (2001), Water depth and surface current retrievals from airborne optical measurements of surface gravity wave dispersion. Journal of Geophysical Research 106(C8), pp. 16903–16915.

Hamm, L., Capobianco, M., Dette, H. H., Lechuga, A., Spanhoff, R. & Stive, M. J. F. (2002). A summary of European experience with shore nourishment. Coastal engineering, 47(2), 237-264, issn. 0378-3839.

Lentine, J.D., Nearshore applications of marine radar, M.Sc. Project Report, Oregon State University, 2006.

Lesser, G.R., Roelvink, J.A, Van Kester, J.A.T.M and Stelling, G.S. (2004). Development and Validation of a Three-dimensional Morphological Model. Jnl. of Coastal Research 51 (2004), pp. 883-915.

Nipius, L., 2002. Evaluation of nourishments at Egmond. Rijkswaterstaat, RIKZ, Z2822.51.

Plant, N. G., K. T. Holland & J. A. Puleo (2002), Analysis of the scale of errors in nearshore bathymetric data. Marine Geology 191, pp. 71–86.

Reniers, A.J.H.M., Symonds, G and E.B. Thornton (2001). Modelling of rip currents during RDEX. In: Proceedings Coastal Dynamics'01, Lund.

Reniers, A.J.H.M., J.A. Roelvink and E.B. Thornton. (2004). Morphodynamic modelling of an embayed beach under wave group forcing. Jnl. of Geophysical Research, VOL. 109, C01030, doi:10.1029/2002JC001586, 2004

Roelvink, J.A. 1993. Dissipation in random wave groups incident on a beach.
Coastal Engineering, 19, 127-150.

Ruessink, B.G., D.J.R. Walstra, H.N. Southgate (2003). Calibration and verification of a parametric wave model on barred beaches - Coastal engineering 48, 139-149.

Smit, M.W., A.J.H.M. Reniers, G. Symonds, and B.G. Ruessink, 2006, Modelling non-linear nearshore dynamics on a barred coast: Palm Beach, Australia. Proc. ICCE 2006, in press.

Stockdon, H.F. and Holman, R.A. (2000). Estimation of wave phase speed and nearshore bathymetry from video imagery. Journal of Geophysical Research 105, pp. 22015-22033

Turner, I.L., Aarninkhof, S.G.J., Dronkers, T.D. and McGrath, J. (2004). CZM Applications of Argus Coastal imaging at the Gold Coast, Australia. Jnl. of Coastal Research, 20(3), pp. 739-752.

Van Enckevort, I. M. J. & B. G. Ruessink (2003a), Video observations of nearshore bar behavior. part 1: alongshore uniform variability. Continental Shelf Research 23, pp. 501–512.

Van Enckevort, I. M. J. & B. G. Ruessink (2003b), Video observations of nearshore bar behavior. part 2: alongshore non-uniform variability. Continental Shelf Research 23, pp. 513–532.

Van Koningsveld, M.; J.P.M. Mulder, 2004. "Sustainable Coastal Policy Developments in the Netherlands. A Systematic Approach Revealed." *Journal of Coastal Research* **20(2):** pp. 375-385

Van Koningsveld, M.; M.J.F. Stive and J.P.M. Mulder, 2004. "Balancing research efforts and management needs. A challenge to coastal engineering." Proceedings of the 29th Int Conf. of Coast. Eng. Lisbon, Portugal, 2004. pp. 2985 - 2997

Van Rijn, L.C., B.G. Ruessink and J.P.M. Mulder, 2002. Coast3D-Egmond. The behavior of a straight sandy coast on the time scale of storms and seasons. Aqua Publication, Amsterdam, The Netherlands.

Wallace, J.M. & Dickinson, R.E. (1972) Empirical Orthogonal representation of time series in the frequency domain. Part I: Theoretical considerations, Journal of Applied Meteorology, 11 (6), pp. 887-892.

Wijnberg, K.M., 2002. Environmental controls on decadal morphologic behavior of the Holland coast. Marine Geology 189, pp. 227-247.

Wijnberg, K.M., J.A. Roelvink and S.G.J. Aarninkhof, 2004. Bed variability in the surf zone at the storm- and seasonal time scale, mapped by Argus-video techniques. Rijkswaterstaat, RIKZ, Z3781.

WL | Delft Hydraulics

Rotterdamseweg 185
postbus 177
2600 MH Delft
telefoon 015 285 85 85
telefax 015 285 85 82
e-mail info@wldelft.nl
internet www.wldelft.nl

Rotterdamseweg 185
p.o. box 177
2600 MH Delft
The Netherlands
telephone +31 15 285 85 85
telefax +31 15 285 85 82
e-mail info@wldelft.nl
internet www.wldelft.nl